UNIVERSIDAD DE CHILE
FACULTAD DE CIENCIAS FÍSICAS Y MATEMÁTICAS
DEPARTAMENTO DE GEOLOGÍA

PETROGENESIS AND GEOCHRONOLOGY OF LARGE QUATERNARY PYROCLASTIC ERUPTIONS IN CENTRAL CHILE: PUDAHUEL IGNIMBRITE CASE

TESIS PARA OPTAR AL GRADO DE DOCTORA
EN CIENCIAS MENCIÓN GEOLOGÍA

CAMILA ANDREA PINEDA RAMÍREZ

PROFESOR GUÍA:
DIEGO MORATA CÉSPEDES

MIEMBROS DE LA COMISIÓN:
ÁLVARO AMIGO RAMOS
ÁNGELO CASTRUCCIO ÁLVAREZ
JULIA EVE HAMMER
PATRICIA LARREA MARQUEZ

SANTIAGO DE CHILE
2022

RESUMEN DE LA TESIS PARA OPTAR
AL GRADO DE: Doctora en Ciencias, mención Geología
POR: Camila Andrea Pineda Ramírez
FECHA: 2022
PROFESOR GUÍA: Diego Morata Céspedes

PETROGÉNESIS Y GEOCRONOLOGÍA DE GRANDES ERUPCIONES PIROCLÁSTICOS CUATERNARIAS DE CHILE CENTRAL: CASO DE LA IGNIMBRITA PUDAHUEL

La Ignimbrita Pudahuel es un depósito cuaternario que se ha asociado a la formación de la caldera Diamante, la cual se encuentra ubicada en la Zona Volcánica Sur de Los Andes. La caldera forma parte del complejo volcánico Maipo, el cual también incluye el estratovolcán activo Maipo. Esta ignimbrita es el resultado de una erupción de gran volumen (135 km^3 DRE), cuyos afloramientos se encuentran tanto en Chile como en Argentina en zonas densamente pobladas. El presente estudio busca comprender la génesis de esta erupción formadora de caldera a partir de una caracterización de factores como la edad, sus condiciones pre-eruptivas y los posibles procesos magmáticos que pudieron dar origen a este evento, para así poder evaluar el potencial riesgo del complejo volcánico Maipo.

La edad de este depósito es un tópico de debate, debido a que se han realizado diversas dataciones con resultados discordantes; acá se presentan nuevas edades obtenidas a partir del método U–Th en circones, resultantes en 167 ± 8 ka. Además, se ha encontrado que las razones de las actividades U–Th en circones pueden verse afectadas por la presencia de monacita. Este mineral incorpora en su estructura REE, U, Th en razones diferentes al circón y por lo tanto su cristalización conjunta afecta las edades U/Th obtenidas a partir de circones. Se sugiere tener en consideración este comportamiento para el cálculo de edades, sobre todo en el caso de erupciones jóvenes, en donde variaciones de miles de años pudieran afectar la interpretación de procesos y la percepción del riesgo asociado.

Las condiciones pre-eruptivas son determinadas a partir de aproximaciones analíticas y experimentales. Se utilizó el geotermómetro de óxidos de Fe-Ti en conjunto con el higrómetro de plagioclasa para determinar condiciones de T-X_{H2O}^{fl}, lo que fue combinado con un modelo de solubilidad de agua, para establecer la presión de almacenamiento del magma. A partir de este método, el cual fue aplicado a temperaturas hasta los 850 ºC, se estableció un rango de condiciones P-T-H_2O que satisfacen el equilibrio entre plagioclasa y vidrio de la muestra natural. Para estas condiciones, se realizaron experimentos de equilibrio de fases en pómez, en condiciones saturadas y subsaturadas en vapor de H_2O. La aproximación mineralógica sugiere temperaturas pre-eruptivas de 717±7 ºC, P_{H2O} de 200-360 MPa y H_2O wt.% de 6.9-7.6 wt. %. Los experimentos que mejor reprodujeron las fases y la composición del vidrio de la muestra natural son los realizados a bajas temperaturas (700-750 ºC) y alta P_{Total} (>200 MPa, más probablemente 300-350 MPa), con al menos un 6 wt. % de agua.

Los posibles gatillantes de esta erupción deben poder perturbar un reservorio alojado a profundidades relativamente altas. Resultados preliminares de inclusiones vítreas, indican que flujos de CO_2 pudieran haberse infiltrado en el magma lo que podría llegar a gatillar una erupción. Sin embargo, es factible que mecanismos externos al reservorio, como una denudación a gran escala en la zona, hayan sido los responsables de gatillar el evento.

La aparente similitud de la profundidad de almacenamiento del magma que generó a la Ignimbrita Pudahuel con la del actual volcán Maipo, y la generación de magmas dacíticos en el macizo, evidencian la necesidad de realizar más análisis mineralógicos y de monitorear el área para así evaluar con precisión el real riesgo del complejo volcánico Maipo.

THESIS ABSTRACT TO OBTAIN THE DEGREE
OF: Doctora en Ciencias, mención Geología
BY: Camila Andrea Pineda Ramírez
DATE: 2022
ADVISOR: Diego Morata Céspedes

PETROGENESIS AND GEOCHRONOLOGY OF LARGE QUATERNARY PYROCLASTIC ERUPTIONS IN CENTRAL CHILE: PUDAHUEL IGNIMBRITE CASE

The Pudahuel Ignimbrite is a Quaternary deposit associated to the formation of the Diamante caldera, which is in the South Volcanic Zone in the Andes. The caldera is part of the Maipo volcanic complex, which also includes the active Maipo stratovolcano. This ignimbrite is the result of a great volume eruption (135 km^3 DRE), which outcrops are in densely populated areas in Chile and Argentina. This study aims to understand the genesis of this caldera-forming eruption through the characterization of factors such as age, pre-eruptive conditions and possible magmatic processes that could originated this event, and hence evaluate the potential risk of the Maipo volcanic complex.

The age of the deposit is a controversial topic as there are different results obtained with different methods; we present new ages of 167 ± 8 ka, obtained with U–Th in zircons. We found that U–Th activity ratios in zircons can be affected by the presence of monazite, which is a mineral that incorporates REE, U and Th into its structure in a different way than zircon and therefore their simultaneous crystallization affect the U/Th ages in zircons. We suggest considering this behavior in age calculations, especially in young eruptions, where variations of thousands of years can affect the interpretation of processes and the associated risk perception.

The pre-eruptive conditions were determined by analytical and experimental approaches. We used the Fe–Ti oxide geothermometer along with plagioclase hygrometer to determine T-X_{H2O}^{fl} conditions, which was in part combined with a water solubility model to stablish the magma storage pressure. We applied this method to temperatures of up to 850 ºC to determine the range of P-T-H_2O conditions that satisfy the plagioclase-glass equilibrium in the natural sample. For these conditions, we ran phase equilibrium experiments with pumice at saturated and undersaturated water conditions. The mineralogical approach indicates pre-eruptive temperatures of 717±7 ºC, P_{H2O} of 200 - 360 MPa and H_2O wt.% of 6.9 - 7.6 wt.%. The experiments that better reproduce the phases and glass composition of the natural sample are the ones run at low temperatures (700– 750 ºC) and high P_{Total} (> 200 MPa, more likely 300– 350 MPa), with at least 6 wt.% of H_2O.

The possible triggers of the eruption must disturb a reservoir at a relatively high depth. Preliminary results in melt inclusions indicate that CO_2 fluxes could have infiltrated into the reservoir leading to an eruption. However, external mechanisms such as a regional scale denudation, could also pose as a potential trigger.

The depth similarity between the reservoir that generated the Pudahuel Ignimbrite and the current Maipo volcano, as well as the generation of dacitic magmas in it, evidence the necessity of further mineralogic analysis and area monitoring, this in order to precisely assess the real risk posed by the Maipo volcanic complex.

Para Christian B.

Agradecimientos

Quisiera partir agradeciendo al Centro de Excelencia en Geotermia de los Andes (CEGA; Proyecto Fondap-Conicyt Nº15090013 y 15200001) por financiamiento y apoyo en la presente investigación y seguir con su misión de contribuir con la generación de conocimiento científico. Debo agradecer también a la Agencia Nacional para la Investigación y el Desarrollo (ANID) por el financiamiento otorgado mediante la beca de doctorado nacional 2016-21160376.

Le agradezco a mi profesor Diego Morata por su enorme apoyo durante todos estos años, ha sido realmente un placer trabajar juntos en este proyecto, y le estaré siempre agradecida por la motivación y entusiasmo con el que siempre recibió mis propuestas, que para muchos parecían inviables. I would like to thank Julia Hammer, who not only collaborated with me on this great research but was also an important support in this difficult pandemic times. Me gustaría agradecer a Álvaro Amigo, quien sin saberlo y gracias a su búsqueda constante de la integración de equipos para contribuir con avances investigativos en el país, inició una cadena de acciones que llevó a que mi investigación tuviera múltiples colaboraciones internacionales, lo que la diversificó y enriqueció enormemente. Agradezco al resto de los miembros de la comisión Angelo Castruccio y Patricia Larrea por sus comentarios que enriquecieron nuestras discusiones y nos permitieron ver nuestros resultados desde otros puntos de vista. Quisiera agradecerle a Claudia Canatelli por su gran colaboración, su apoyo y por su enorme voluntad de enseñar y guiar. To Philip Ruprech for his important collaboration, his interest and dedication in our work and his thoughtful comments in our manuscript. To Axel Schmitt for his enthusiasm for science and his significant collaboration that led to an interesting and beautiful investigation.

Quisiera agradecer a todas las personas que de alguna u otra manera estuvieron involucradas y permitieron que esta investigación pudiera ser llevada a cabo: Emily First, not only for her collaboration, but for her great disposition and lovely attitude. To Ellyn Huggins for receiving me in her home during my stay in Reno and making my visit a wonderful time. A Paul y Holly quienes me recibieron en su hogar e hicieron de mis viajes a la microsonda unas verdaderas vacaciones. A Hermann y Marlene, quienes también me recibieron en su hogar

con los brazos abiertos, me apoyaron en momentos difíciles e hicieron que mi estadía en Heidelberg fuera una experiencia maravillosa.

A mis amigos geólogos que siempre me apoyaron y estuvieron para mi: Pau, Olmedo, Edwin, Charly y Mila, gracias por su amistad. A Chiri P., Pelao M. y Mumo B. por su constante ayuda, sobre todo en el principio cuando nada estaba claro. A mis amigos no geólogos que me apoyaron enormemente, sobre todo durante los momentos en que las cosas se veían más complicadas: Javi, Dani y Javier.

A mi nueva familia que me ha dado todo su cariño y apoyo desde el primer día que quise seguir este camino, les agradezco de todo corazón: Juana, Rony, Nico, Mariana, Bernardita y Héctor.

Por supuesto, nada sería posible sin mi hermosa familia, mis padres María Angélica y Samuel, gracias por su apoyo incondicional, su inmenso amor y no tener jamás la duda de que puedo lograr todo lo que me proponga. A Sergio, quien es a esta altura es como un padre para mi. A mis hermanos por su alegría, su cariño y su enorme apoyo Vicky, Felipe, Paula y Valeria. A mis hermosos abuelos Inés y Ramón, sin su cariños y apoyo la vida no sería la misma. A todos en mi querida familia Coca, Marce, Caro P., Caro B, Cata y Edgar que siempre han creído en mi.

Por último agradecerle a mi compañero de vida Christian Betancourt, sin tu apoyo nada de esto habría sido posible, gracias e infinitas gracias.

Tabla de contenido

Capítulo 1. Introducción

1. Motivación

Las erupciones formadoras de calderas son aquellas que producen grandes volúmenes (> 100 km^3) de magma y, generalmente, se encuentran asociadas a magmas silíceos y con un bajo contenido de cristales (Deering et al., 2011; Hildreth, 1981; Lindsay et al., 2001; Lipman, 2007). La formación de una caldera puede corresponder a un evento catastrófico debido al carácter explosivo que pueden llegar a tener este tipo de eventos que, dependiendo de su magnitud, pueden llegar a afectar el clima a escala regional o incluso mundial (Gottsmann and Martí, 2008; Lipman, 2000). Es debido a esto que la presencia de un centro volcánico en el cual han ocurrido eventos formadores de caldera, en las cercanías de áreas pobladas representa un riesgo para la vida y forma de vida de las personas que ahí residen (Self, 2015). Para anticipar este tipo de eventos y desarrollar planes de prevención adecuados, es necesaria una completa caracterización del sistema volcánico y combinarla con un monitoreo volcánico activo (National Academies of Sciences and Medicine, 2017). Comprender las condiciones pre-eruptivas y los procesos asociados a la generación de este tipo de erupciones, es por lo tanto, crucial para mejorar la comprensión de estos eventos y de esta manera mitigar los riesgos asociados a su ocurrencia.

En Chile existen más de 100 volcanes, campos volcánicos y complejos de calderas (González-Ferrán, 1995; Simkin and Siebert, 1994), que lo convierte en un laboratorio natural para estudiar procesos volcánicos. El complejo volcánico Maipo, localizado en la zona central del país, es de particular interés debido a que generó una gran erupción formadora de caldera. Durante este evento se produjo una Corriente de Densidad Piroclástica (CDP), denominada Ignimbrita Pudahuel (Wall et al., 1996), cuyos productos pueden ser encontrados en áreas densamente pobladas como por ejemplo en la ciudad de Santiago. Se ha estimado que el volumen de esta CDP es de 250 km^3 y que fue expulsado en un período de tan solo un par de días (Guerstein, 1993). Esta tesis presenta un estudio petrogenético y geocronológico de esta gran erupción que busca ser un aporte en la comprensión de sistemas riolíticos.

2. Objetivos y estructura de la tesis

Si bien existen variados estudios en la Ignimbrita Pudahuel, muchos de ellos se centran en su estratigrafía (*e.g.*, Guerstein, 1993; Troncoso, 2012) o en su edad (*e.g.*, Lara et al., 2008; Stern et al., 1984; Wall et al., 2001); siendo estos últimos, un tanto controversiales ya que los resultados obtenidos varían en el orden del millón de años. Esta investigación pretende expandir el conocimiento que se tiene sobre esta erupción formadora de caldera, teniendo como objetivo principal determinar los tiempos y los procesos asociados a la generación de este magma riolítico. Dentro de los objetivos específicos se encuentran:

- Determinar condiciones de almacenamiento del magma, tales como temperatura, presión, concentración de volátiles y fugacidad de oxígeno.
- Identificar los procesos que pudieron dar origen a esta gran erupción.
- Acotar la posible edad de la erupción y constreñir las escalas de tiempo en la que se habría originado el magma riolítico.

Cada uno de estos objetivos es abordado en los siguientes capítulos, en donde mediante el desarrollo de estudios petrológicos, geoquímicos y geocronológicos, se busca comprender la génesis del cuerpo magmático que dio origen a la Ignimbrita Pudahuel. El capítulo 1 presenta las principales motivaciones y objetivos de la investigación. El capítulo 2 entrega el contexto geológico en el que encuentra el complejo volcánico Maipo, considerando el regional y local, y entrega los principales antecedentes de la Ignimbrita Pudahuel. El capítulo 3 presentan estudios geocronológicos y cristaloquímicos en circones y se titula “Monazite as control on Th/U in magmatic zircon” y fue sometido para su publicación en la revista *Chemical Geology*. En el capítulo 4 se aborda la determinación de las condiciones pre-eruptivas y corresponde a un trabajo publicado en la revista *Lithos* titulado “Storage conditions of a caldera-forming volcanic eruption: insights from the Pudahuel rhyolitic ignimbrite in central Chile (32º 10’ S)”. El capítulo 5 presenta resultados de análisis de inclusiones vítreas. El capítulo 6 resume los principales resultados de esta investigación, presenta una discusión y conclusión general sobre sus implicancias.

3. Publicaciones y resultados presentados en congresos

El trabajo desarrollado durante esta tesis ha sido presentado en diversos congresos científicos y cuenta con una publicación en la revista *Lithos* y un manuscrito sometido en la revista *Chemical Geology*:

Pineda, C., Hammer, J., First, E., Morata, D. 2021. Storage conditions of a caldera-forming volcanic eruption: insights from the Pudahuel rhyolitic ignimbrite in central Chile (32º10'S). Lithos 400–401, 106382. https://doi.org/10.1016/J.LITHOS.2021.106382

Pineda, C., Schmitt, A., Morata, D. Monazite as control on Th/U in magmatic zircon. *Submitted to Chemical Geology.*

Pineda, C. Cannatelli, C., Ruprecht, P., Morata, D. 2019. Melt Inclusion Study from the Quaternary Pudahuel Ignimbrite: A Window to Magma Chamber Processes. Presentación oral, Goldschmidt, Barcelona, España

Pineda, C. Cannatelli, C., Morata, D. 2018. Evolución magmática de una erupción formadora de caldera a partir del estudio de inclusiones vítreas. Presentación poster, XV Congreso Geológico Chileno, Concepción, Chile.

Pineda, C., Hammer, J., Morata, D. 2018. Storage Conditions of Pudahuel Rhyolitic Ignimbrite in Central Chile. Presentación poster, AGU Chapman conference, Colbún, Chile

Pineda, C., Hammer, J., Morata, D. 2017. Storage Conditions of Pudahuel Rhyolitic Ignimbrite in Central Chile. Presentación poster, IAVCEI, Portland, USA

4. Referencias

Deering, C.D., Bachmann, O., Vogel, T.A., 2011. The Ammonia Tanks Tuff: Erupting a melt-rich rhyolite cap and its remobilized crystal cumulate. Earth Planet. Sci. Lett. 310, 518–525. https://doi.org/10.1016/j.epsl.2011.08.032

González-Ferrán, O., 1995. Volcanes de Chile. Instituto Geográfico Militar. Santiago 635.

Gottsmann, J., Martí, J. (Eds.), 2008. Caldera Volcanism Analysis, Modeling and Response, Developments in Volcanology.

Guerstein, P.G., 1993. Origen y significado geológico de la asociación piroclástica pumícea.

Preistoceno de la Provincia de Mendoza entre los 33°30’ y 34°40’ L.S. Universidad Nacional de La Plata, La Plata.

Hildreth, W., 1981. Gradients in silicic magma chambers: Implications for lithospheric magmatism. J. Geophys. Res. Solid Earth 86, 10153–10192. https://doi.org/https://doi.org/10.1029/JB086iB11p10153

Lara, L., Wall, R., Stockli, D., 2008. La ignimbrita Pudahuel (Asociación Piroclástica Pumícea) y la caldera Diamante (33° S): nuevas edades U–Th–He, in: XVII Congreso Geológico Argentino. p. 1365.

Lindsay, J.M., De Silva, S., Trumbull, R., Emmermann, R., Wemmer, K., 2001. La Pacana caldera, N. Chile: A re-evaluation of the stratigraphy and volcanology of one of the world’s largest resurgent calderas. J. Volcanol. Geotherm. Res. 106, 145–173. https://doi.org/10.1016/S0377-0273(00)00270-5

Lipman, P.W., 2007. Incremental assembly and prolonged consolidation of Cordilleran magma chambers: Evidence from the Southern Rocky Mountain volcanic field. Geosphere 3, 42–70. https://doi.org/10.1130/GES00061.1

Lipman, P.W., 2000. Calderas. Encycl. Volcanoes 643–662.

National Academies of Sciences and Medicine, E., 2017. Volcanic Eruptions and Their Repose, Unrest, Precursors, and Timing. The National Academies Press, Washington, DC. https://doi.org/10.17226/24650

Self, S., 2015. Explosive Super-Eruptions and Potential Global Impacts, Volcanic Hazards, Risks and Disasters. Elsevier Inc. https://doi.org/10.1016/B978-0-12-396453-3.00016-2

Simkin, T., Siebert, L., 1994. Volcanoes of the World. Geoscience Presss. Inc. Tusson. Arizona.

Stern, C.R., Amini, H., Charrier, R., Godoy, E., Herve, F., Varela, J., 1984. Petrochemistry and age of rhyolitic pyroclastic flows which occur along the drainage valleys of the río Maipo and río Cachapoal (Chile) and the río Yaucha and río Papagayos (Argentina). Rev. Geológica Chile 23, 39–52.

Troncoso, C., 2012. Estudio Estratigráfico y de volcanología física de la Ignimbrita Pudahuel. Universidad de Chile.

Wall, R., Gana, P., Gutiérrez, Á., 1996. Mapa Geológico Del Área De San Antonio-

Melipilla, Regiones de Valparaíso, Metropolitana y del Libertador General Bernardo O'Higgins, in: Servicio Nacional de Geología y Minería, Mapa Geológico Nº 2, 1 Mapa Escala 1:100.000. Santiago.

Wall, R.M., Lara, L.E., Perez de Arce, C., 2001. Upper pliocene-lower pleistocene 40Ar/39Ar ages of Pudahuel ignimbrite (Diamante-Maipo volcanic complex), Central Chile (33.5º).

Capítulo 2. Contexto Geológico

1. Contexto regional

La zona de estudio se ubica en el margen oeste de la Placa Sudamericana, bajo la cual ha estado subductando la placa de Nazca desde el Jurásico temprano de manera casi ininterrumpida. Esto ha permitido la formación de un arco magmático, que se ha desplazado desde donde actualmente se ubica la Cordillera de la Costa hacia el este, ubicándose actualmente en la Cordillera de los Andes (Scheuber et al., 1994). El margen sudamericano se divide en cuatro zonas con volcanismo activo: Zona Volcánica Norte (ZVN), Zona Volcánica Central (ZVC), Zona Volcánica Sur (ZVS) y Zona Volcánica Austral (ZVA) (Fig. 1a). La actividad andina resulta de la subducción de las placas oceánicas de Nazca y Antártica bajo la litósfera continental del oeste de Sudamérica. Esto es confirmado, no solo por los gap volcánicos en zonas donde el proceso de subducción no ocurre (dorsales de Juan Fernández y de Chile, Fig. 1a); sino que también, por estudios geoquímicos que atribuyen la generación de magmas a la deshidratación y/o fusión de la litósfera de la placa oceánica subductada, y a evidencia de interacción entre fluidos provenientes de esta placa con la cuña mantélica (Stern et al., 2007).

El complejo volcánico Maipo se localiza en el área septentrional de la ZVS, la que se encuentra limitada al norte por la subducción de la dorsal de Juan Fernández, y al sur por la intersección de la dorsal de Chile con la fosa (Stern et al., 2007) (Fig. 1b). La dirección de convergencia entre las placas de Nazca y Sudamericana es oblicua (*ca*. 20-30º) con respecto a la fosa (Dewey and Lamb, 1992; Jarrard, 1986) y la velocidad a la que ocurre este proceso es de 7-9 cm/año (DeMets et al., 1990). En esta zona, el ángulo de subducción de la placa aumenta desde ~ 20º en el norte hasta más de 25º en el sur, lo que implica una variación en la distancia de la fosa al frente volcánico desde más de 290 km en el norte hasta menos de 270 km en el sur (Stern et al., 2007). La ZVS se encuentra formada por ocho estratovolcanes y la Caldera Diamante. De norte a sur, los centros eruptivos más antiguos incluyen a los Nevado de Piuquenes (6019 m), Marmolejo (6108 m), Castillo (5485 m), Caldera Diamante, Listado (4250 m) y Picos del Barroso (5000 m) (Fig. 2). Todos se encuentran muy erosionados y los que se encuentran más al norte colapsaron lateralmente formando avalanchas debido a la inestabilidad causada por alteración hidrotermal y erosión intensa.

Los centros más jóvenes consisten en estratovolcanes como el Tupungato, Tupungatito (5682 m), complejo volcánico San José (5856 m) ubicado sobre el Marmolejo y el volcán Maipo que se encuentra dentro de la Caldera Diamante. Los volcanes Tupungatito, San José y Maipo han tenido erupciones históricas, las más recientes en 1987, 1960 y 1912, respectivamente. Estos tres centros volcánicos poseen altas elevaciones (> 5920 m), se encuentran cubiertos de glaciares y forman parte del sistema de drenaje que alimenta al río Maipo, que fluye al sur de Santiago, la ciudad más poblada de Chile (Stern et al., 2007).

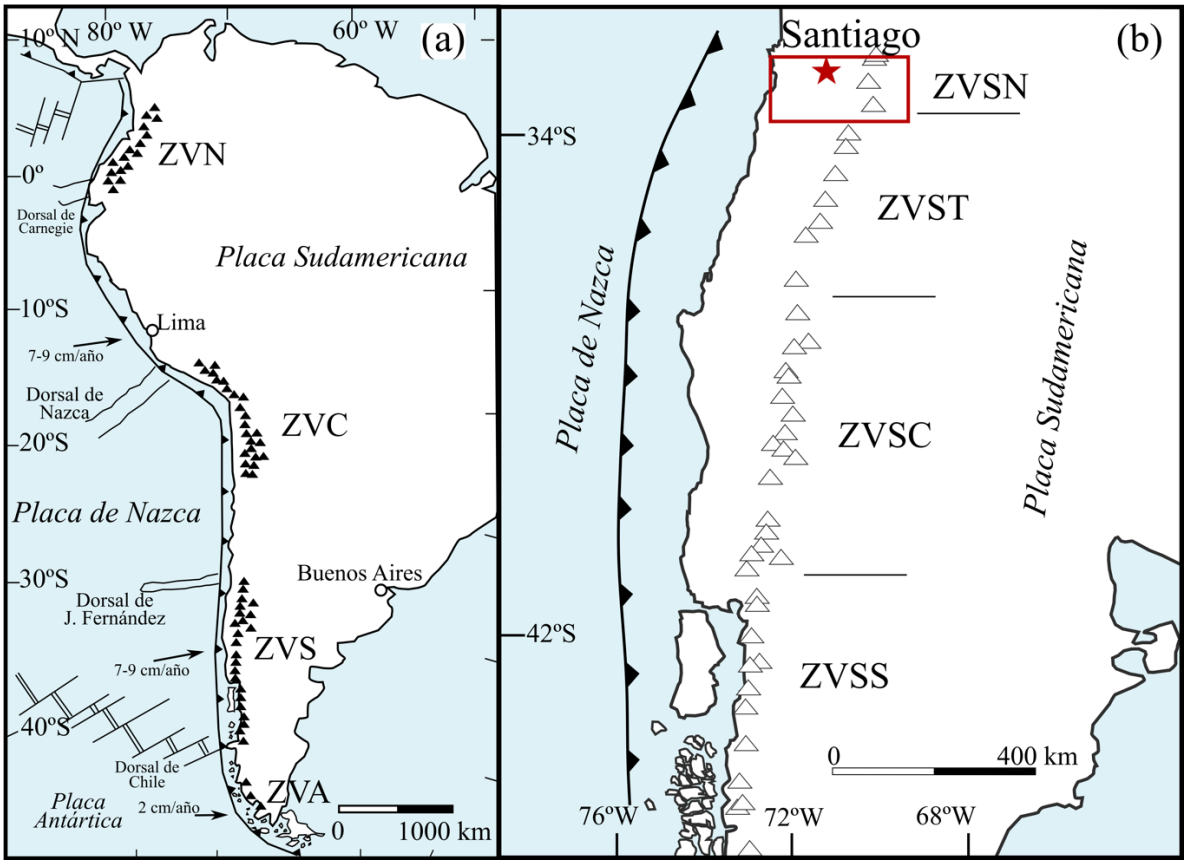

Figura 1: Contexto geológico regional. a) Margen sudamericano indicando zonas volcánicas de los Andes. ZVN: Zona Volcánica Norte, ZVC: Zona Volcánica Central, ZVS: Zona Volcánica Sur, ZVA: Zona Volcánica Austral; b) Aproximación de la ZVS, indicando ubicación del área de estudio. ZVSN: ZVS Norte, ZVST: ZVS Transicional, ZVSC: ZVS Central, ZVSS: ZVS Sur. Ambas imágenes modificadas de Stern et al., (2007).

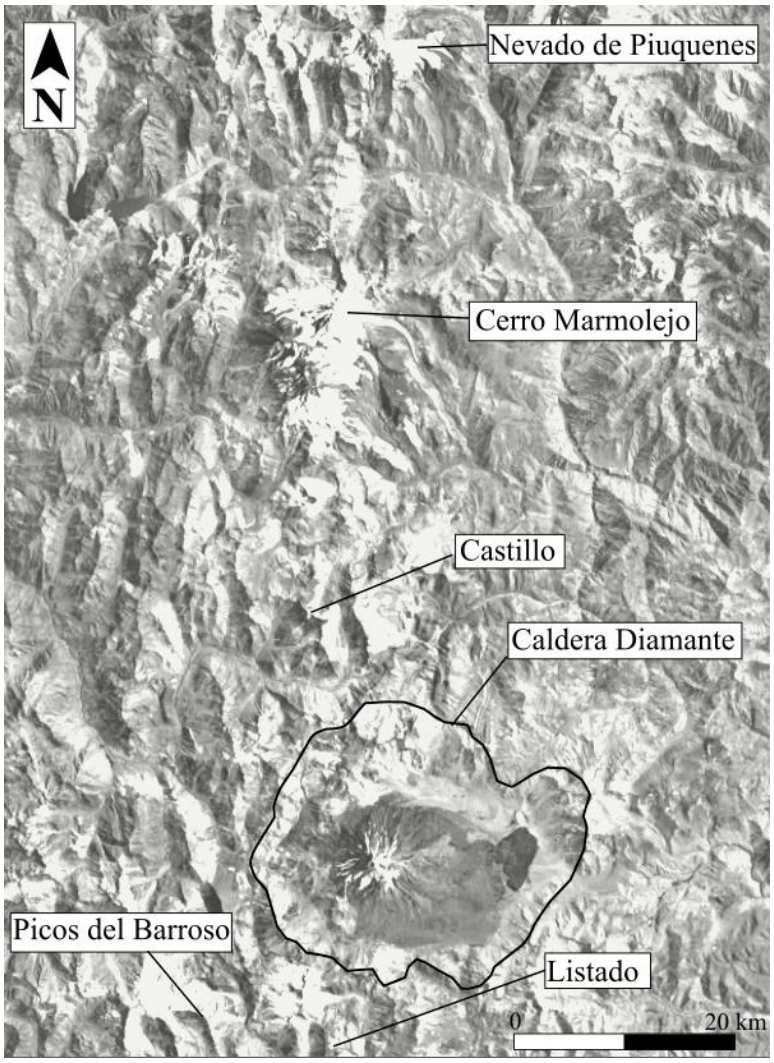

Figura 2: Detalle de los centros eruptivos más antiguos de la ZVSN.

5. Contexto local

El complejo volcánico Maipo se ubica, como se mencionó anteriormente, en la zona central de Chile en la Cordillera de los Andes, en el límite entre Chile y Argentina (34º09'S, 69º59'W), en el norte de la ZVS (Fig. 1b–2). El complejo incluye la caldera Diamante y el volcán Maipo. La caldera se formó durante una erupción VEI 7 (Guerstein, 1993) que produjo una voluminosa ignimbrita, primeramente descrita por Polanski, (1963) y llamada Asociación Piroclástica Pumícea. El depósito es identificado como Ignimbrita Pudahuel en Chile y Toba Diamante en Argentina (*e.g.,* Wall et al., 1996 and Harrington, 1989 respectivamente).

En las paredes de la caldera Diamante se observa una secuencia pre-cuaternaria correspondiente a rocas sedimentarias mesozoicas que conforman una faja plegada y corrida

con orientación N-S, que se encuentra intruída por cuerpos sub-volcánicos y cubierta por lavas, probablemente mio-pliocenas (Sruoga et al., 2005a). Al norte de la caldera se encuentra la faja plegada y corrida del Aconcagua, que se divide en dos zonas de este a oeste: zona de imbricación y la zona de inversión tectónica (Ramos et al., 1997). Se desarrolló y fue activa principalmente entre el Mioceno inferior y el superior, siendo progresivamente desactivada y atrapada en el interior del orógeno andino, debido a la deformación hacia el este a partir del Mioceno superior (Ramos, 1988). Al este de la caldera se encuentra el bloque de la Cordillera Frontal, cuya estructuración se produjo durante los estadíos finales de la orogenia Andina, pero con posterioridad a la Cordillera Principal. Al Sur de la caldera, se encuentra la faja plegada y corrida de Malargüe, que se puede dividir en dos zonas de este a oeste: la del sector externo y la del interno (Kozlowski et al., 1993). La primera se caracteriza por una estructura con orientación general NNO-SSE y por originarse exclusivamente durante la orogenia antigua, sin intervención de estructuras previas posteriormente reactivadas; y la segunda, se caracteriza por poseer una orientación de estructuras de NNE-SSO que corresponde a la expresión del período de extensión jurásico y no es coincidente con deformación originada durante la última orogenia (NNO-SSE) (Sruoga et al., 2005a).

6. La Ignimbrita Pudahuel

Esta corriente de densidad piroclástica (CDP) posee una extensa distribución, encontrándose afloramientos tanto en Chile como en Argentina. Su volumen fue primeramente estimado en 450 km^3 a partir de promedios de espesor de los depósitos expuestos (Stern et al., 1984). Luego, a partir de trabajos de mapeo y de detallada descripción estratigráfica en el lado Argentino, se estimó un volumen total de 20 km^3 (5 km^3 densidad de roca equivalente DRE por sus siglas en inglés: *Dense-Rock Equivalent*) para dos unidades de caída que iniciaron la erupción y un volumen total de 250 km^3 (130 km^3 DRE) para los depósitos de la CDP (Guerstein, 1993). Tomando en consideración estos resultados y combinándolos con descripciones estratigráficas detalladas del lado chileno, Troncoso, (2012) estimó un valor muy similar del volumen (135 km^3 DRE).

La Ignimbrita Pudahuel se compone por depósitos de CDP matriz-soportados que se encuentran en los valles de los ríos Maipo y Cachapoal en Chile y en los valles de los ríos Yaucha, Rosario y Papagayos en Argentina (Fig. 3). Si bien se trata de un depósito bastante homogéneo, existen algunas diferencias entre los afloramientos encontrados en cada uno de

los valles, siendo las más destacas: la presencia de pipas de degasificación en el valle del Maipo y en zonas distales de los valles del Yaucha y Papagayos; variaciones en el tamaño de las pómez y en el tamaño y tipo de líticos; y el grado de soldamiento, que va desde no soldado hasta moderadamente soldado en algunas áreas de los valles del Maipo y del Rosario (Guerstein, 1993; Troncoso, 2012). Con respecto al tipo de líticos, Troncoso (2012) identificó líticos plutónicos y volcánicos en ambos valles chilenos, además, en facies distales del valle del Maipo identificó líticos volcanoclásticos, caliza y obsidiana. En los valles del Papagayos y el Yaucha se identificaron líticos sedimentarios y obsidiana, además de los volcánicos e intrusivos. En la facies proximales solo se identifican líticos de origen volcánico (Guerstein, 1993). En general, los clastos presentes en los depósitos de la CDP corresponden, en orden de abundancia volumétrica, a pómez altamente vesiculadas (60-90 %) de hasta 18 cm y líticos del basamento (Guerstein, 1993; Hynek et al., 2010; Troncoso, 2012). Pómez con diferentes tonalidades, que varían entre rosado, gris claro y blanco con bandas grisáceas, han sido descritas por Burkert et al., (2010).

La cantidad de flujos generados por la erupción no es del todo clara, mientras Guerstein (1993) sugiere que la CDP se generó de manera simultánea en todos los valles, Troncoso (2012), interpreta una fuerte variación en la abundancia de líticos de obsidiana en la parte superior del depósito del valle del Maipo, como evidencia de la ocurrencia de dos flujos. En la zona Argentina se han descrito depósitos de caída de ceniza bajo la CDP, lo que se ha interpretado como una fase pliniana inicial de la erupción. La presencia de un contacto oxidado entre bandas de estos depósitos, sugiere una exposición sub-aérea por lo que se interpretan como dos unidades de caída (Guerstein, 1993).

La composición de roca total de la Ignimbrita Pudahuel, tanto de la pómez como de la matriz, es riolítica (~74 wt.% SiO_2) (Guerstein, 1993; Hynek et al., 2010; Sruoga et al., 2005b; Stern et al., 1984). Los análisis de elementos traza indican altos valores de Rb y Ba (103-156 ppm y 715-769 ppm, respectivamente) y bajos valores de Sr y Zr (62-86 ppm y 57-89 ppm, respectivamente), lo que sugiere un fuerte componente cortical combinado con extensa cristalización fraccionada (Futa and Stern, 1988; Stern et al., 1984). En clastos de pómez y esquirlas de vidrio de la CDP, pertenecientes a una sección estratigráfica expuesta entre los valles Papagayos y Yaucha, se han observado pequeñas variaciones en las concentraciones

de elementos como Fe_2O_3 (0.41-0.67%), Cl (0.068-0.117%) y CaO (0.44-0.53%) (Hynek et al., 2010).

Tanto las pómez como la matriz de ceniza que conforman la Ignimbrita Pudahuel, se encuentran compuestas principalmente por vidrio y presentan un bajo contenido de cristales (~6 wt.%), que incluyen: plagioclasa, biotita, titanomagnetita, apatito y circón (Guerstein, 1993; Stern et al., 1984). La biotita y el circón han sido utilizados en la aplicación de técnicas geocronológicas para obtener la edad de la erupción. Las edades obtenidas varían de manera significativa. Stern et al., (1984) realizaron dataciones con el método de *fission track* en circones y obtuvieron edades de 0.45±0.06 Ma. Se han realizado dataciones con el método $^{40}Ar/^{39}Ar$ en biotitas que han entregado edades de ~2.3±0.3 Ma (Wall et al., 2001). Por otro lado, dataciones con el método (U-Th)/He en circones entregaron edades de ~0.15 Ma (Lara et al., 2008), consistente con dataciones realizadas con el método U-Pb en circones que entregaron edades de ~0.13 Ma (Pineda, 2015).

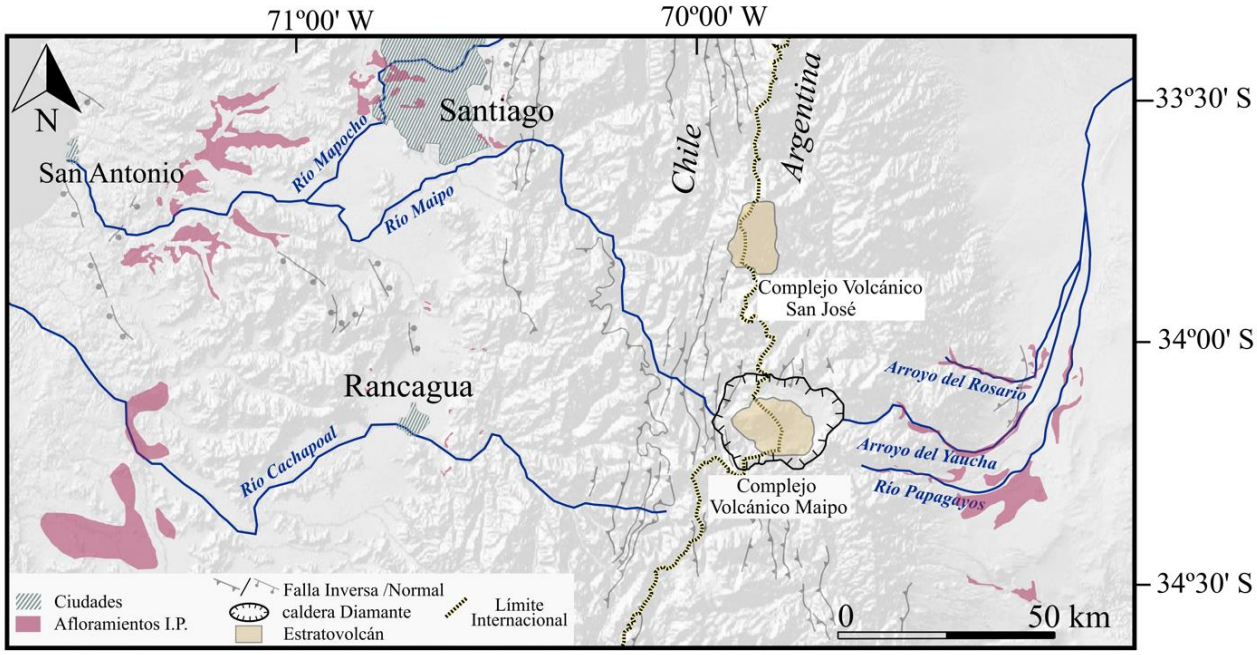

Figura 3: Ubicación regional local y contexto tectónico. Modelo de Elevación Digital mostrando los afloramientos de la Ignimbrita Pudahuel (I.P.), datos de (Gana et al., 1996; Sellés and Gana, 2001; SERNAGEOMIN, 2003; Sruoga et al., 2005a; Stern et al., 1984; Wall et al., 1999, 1996). Se indica la ubicación de la caldera Diamante, volcán Maipo y de las principales ciudades del área.

7. Referencias

Burkert, C., Freundt, A., Gilbert, D., Kutterolf, S., 2010. Origin of magmatic components in the Diamante Tuff, in: SFB 574 Subduction Workshop. Pucón.

DeMets, C., Gordon, R.G., Argus, D.F., Stein, S., 1990. Current plate motions. Geophys. J. Int. 101, 425–478. https://doi.org/10.1111/j.1365-246X.1990.tb06579.x

Dewey, J.F., Lamb, S.H., 1992. Active tectonics of the Andes. Tectonophysics 205, 79–95. https://doi.org/10.1016/0040-1951(92)90419-7

Futa, K., Stern, C.R., 1988. Sr and Nd isotopic and trace element compositions of Quaternary volcanic centers of the Southern Andes. Earth Planet. Sci. Lett. 88, 253–262. https://doi.org/10.1016/0012-821X(88)90082-9

Gana, P., Wall, R., Gutiérrez, Á., 1996. Mapa Geológico Del Área De Valparaíso- Curacaví, Regiones de Valparaíso y Metropolitana, Servicio Nacional de Geología y Minería, Mapa Geológico Nº 1, 1 mapa escala 1:100.000. Santiago.

Guerstein, P.G., 1993. Origen y significado geológico de la asociación piroclástica pumícea. Preistoceno de la Provincia de Mendoza entre los 33º30' y 34º40' L.S. Universidad Nacional de La Plata, La Plata.

Harrington, R., 1989. The Diamante Caldera and Maipo Caldera Complex in the Southern Andes of Argentina and Chile (34º 10' south). Rev. la Asoc. Geológica Argentina 19, 186–193.

Hynek, S.A., Marchetti, D.W., Fernandez, D.P., Cerling, T.E., 2010. Composition, pre-eruptive zonation, and geochronologic significance of the ~450ka Diamante Tuff, Andean Cordillera (34°S), Argentina. Quat. Geochronol. 5, 591–601. https://doi.org/10.1016/j.quageo.2010.02.002

Jarrard, R.D., 1986. Relations among subduction parameters. Rev. Geophys. 24, 217–284. https://doi.org/10.1029/RG024i002p00217

Kozlowski, E., Manceda, R., Ramos, V.A., 1993. Estructura, in: Geología y Recursos Naturales de Mendoza. Asociación Geológica Argentina Buenos Aires, pp. 235–256.

Lara, L., Wall, R., Stockli, D., 2008. La ignimbrita Pudahuel (Asociación Piroclástica Pumícea) y la caldera Diamante (33° S): nuevas edades U–Th–He, in: XVII Congreso Geológico Argentino. p. 1365.

Pineda, C., 2015. Geocronología U-Pb en circones de la Ignimbrita Pudahuel. Universidad

de Chile, Santiago, p. 105. Geologist Professional Degree Thesis.

Polanski, J., 1963. Estratigrafía, neotectónica y geomorfología del Pleistoceno pedemontano entre los ríos Diamante y Mendoza: Provincia de Mendoza, Revista de la Asociación Geológica Argentina.

Ramos, V.A., 1988. The tectonics of the Central Andes; 30 to 33 S latitude. Spec. Pap. Geol. Soc. Am. 218, 31–54. https://doi.org/10.1130/SPE218-p31

Ramos, V.A., Alvarez, P.P., Aguirre Urreta, M.B., Godoy, E., 1997. La Cordillera Principal a la latitud del paso Nieves Negras (22 50'S), Chile–Argentina. VIII Congreso Geológico Chileno. Actas 3, 1704–1708.

Scheuber, E., Bogdanic, T., Jensen, A., Reutter, K.-J., 1994. Tectonic Development of the North Chilean Andes in Relation to Plate Convergence and Magmatism Since the Jurassic. Tectonics South. Cent. Andes 121–139. https://doi.org/10.1007/978-3-642-77353-2_9

Sellés, D., Gana, P., 2001. Geología del área Talagante-San Francisco de Mostazal, Regiones Metropolitana de Santiago y del Libertador General Bernardo O'Higgins, Servicio Nacional de Geología y Minería, Carta Geológica de Chile, Serie Geología Básica 74, 1 mapa escala 1:100.000. Santiago.

SERNAGEOMIN, 2003. Mapa Geológico de Chile: versión digital, Servicio Nacional de Geología y Minería, Pubilicación Geológica Digital, Nº 4 (CD-ROM, versión 1.0). Santiago.

Sruoga, P., Etcheverria, M., Folguera, A., Repol, D., 2005a. Programa Nacional de Cartas Geológicas Hoja Geológica 3569-I Volcán Maipo, provincia de Mendoza. Buenos Aires.

Sruoga, P., Llambías, E.J., Fauqué, L., Schonwandt, D., Repol, D.G., 2005b. Volcanological and geochemical evolution of the Diamante Caldera-Maipo volcano complex in the southern Andes of Argentina (34°10′S). J. South Am. Earth Sci. 19, 399–414. https://doi.org/10.1016/j.jsames.2005.06.003

Stern, C.R., Amini, H., Charrier, R., Godoy, E., Herve, F., Varela, J., 1984. Petrochemistry and age of rhyolitic pyroclastic flows which occur along the drainage valleys of the río Maipo and río Cachapoal (Chile) and the río Yaucha and río Papagayos (Argentina). Rev. Geológica Chile 23, 39–52.

Stern, C.R., Moreno, H., López-Escobar, L., Clavero, J.E., Lara, L.E., Naranjo, J.A., Parada, M.A., Skewes, M.A., 2007. Chilean volcanoes. Geol. Soc. Spec. Publ. 147–178. https://doi.org/10.1144/goch.5

Troncoso, C., 2012. Estudio Estratigráfico y de volcanología física de la Ignimbrita Pudahuel. Universidad de Chile.

Wall, R., Gana, P., Gutiérrez, Á., 1996. Mapa Geológico Del Área De San Antonio-Melipilla, Regiones de Valparaíso, Metropolitana y del Libertador General Bernardo O'Higgins, in: Servicio Nacional de Geología y Minería, Mapa Geológico Nº 2, 1 Mapa Escala 1:100.000. Santiago.

Wall, R., Sellés, D., Gana, P., 1999. Area Tiltil-Santiago, Región Metropolitana, Servicio Nacional de Geología y Minería, Mapa Geológico Nº 11, 1 mapa escala 1:100.000. Santiago.

Wall, R.M., Lara, L.E., Perez de Arce, C., 2001. Upper pliocene-lower pleistocene $^{40}Ar/^{39}Ar$ ages of Pudahuel ignimbrite (Diamante-Maipo volcanic complex), Central Chile ($33.5^{0}S$).

Chapter 3. Monazite as a control on Th/U in magmatic zircon

Abstract

Zircon is one of the most widely studied minerals for geochronology, and it has been successfully used to determine the age of young eruptions (< 300 ka) through U-Th dating. However, the processes leading to Th/U variations between cogenetic zircon crystals that are often much larger than expected from partitioning considerations are still not fully understood, despite the critical importance of zircon Th/U for the disequilibrium correction of radiometric ages, and for identifying different zircon generations. Here, we present ^{238}U-^{230}Th disequilibrium ages and trace element abundances of zircon from the Quaternary Pudahuel Ignimbrite, a caldera-forming eruption associated to the Maipo volcanic complex in central Chile. Zircon chemical signatures show a decrease of Th/U along with decreasing Ti-in-zircon temperatures that can be related to the presence of accessory minerals which incorporate Th over U into its structure. At higher temperatures, apatite fractionation could influence Th/U partitioning and in consequence U-Th activity ratios in zircon, but at lower temperatures monazite would exert the main control. These variations can also be identified along individual depth profiles, suggesting that monazite co-crystallization is the key cause for a sharp rimward decrease in zircon Th/U. The isochron age calculated from zircon with low Th/U (^{238}U/^{232}Th activity > 5.2) crystallized at low temperature below monazite saturation (167 ± 8 ka; 1σ error) is younger than for zircon with high Th/U (^{238}U/^{232}Th < 5.2). This presents the most precise age constraint available for Pudahuel Ignimbrite, albeit as a maximum eruption age. These results are particularly important in the study of young eruptions, where accurate ages are improtant to reliably interpret eruptive recurrence and volcanic chronostratigraphy, which in turn can affect the hazard awareness of volcanic systems.

Keywords: Zircon, Monazite, U-Th dating, Andes

1. Introduction

Constraining eruption ages for individual volcanoes or volcanic provinces is a first-order requirement to determine eruptive recurrence and assess volcanic hazards. In the case of silicic eruptions, this becomes a critical issue considering that they are one of the most dangerous types of volcanism because of their explosivity (Lipman, 2000; Self, 2015). One successful approach is to determine the age of young eruptions (< 300 ka) via U-Th geochronology of accessory minerals, especially zircon (e.g., Cooper and Reid, 2008). Zircon records the timing of crystallization, which is a maximum age for the eruption. If zircon crystallization is rapid relative to the critical half-life of ^{230}Th (75,584 ka; Cheng et al., 2013), and occurs briefly before the eruption, U-Th isochron ages are obtained that are reasonably close approximations for the eruption ages (Burgess et al., 2021). Despite many successful applications of this method, some fundamental aspects regarding the processes leading to an isochronous spread of data in the U-Th disequilibrium diagram, and the interpretation of often overdispersed data that result from protracted zircon crystallization and recycling of zircon remain poorly understood. On one hand, there is the question, why cogenetic zircon that crystallized within a duration that is much shorter than the half-life of ^{230}Th (based on the formation of an isochron) still can vary widely in Th/U? On the other hand, Th/U has been proposed as an easily obtainable indicator to distinguish between near-eruption (= cold, autocrystic) from older, potentially recycled (= hot, antecrystic) zircon, but why Th/U in zircon might change with magmatic temperature remains ambiguous (e.g., Kirkland et al., 2015). One possibility is the presence of accessory minerals such as monazite that can modify Th/U in the melt and consequently in zircon crystallizing from it (Breiter, 2016). Monazite competes with zircon for Th (and to lesser extent U), as well as trace elements such the light rare earth elements (REE). Co-saturation of zircon and monazite in melts could thus strongly

affect Th/U in zircon. Constraining the causes of Th/U variability in zircon could provide insights into the thermochemical evolution of the melt and aid in identifying different generations of zircon whose age difference cannot be easily resolved by dating methods alone.

Here, we studied over 200 crystals of zircon as well as cogenetic monazite for the Quaternary Pudahuel Ignimbrite, a caldera forming eruption associated to the Maipo volcanic complex located in central Chile in the Andes Cordillera (Fig. 1). This massive (135 km^3 Dense Rock Equivalent, DRE) ignimbrite is spread through one of the most populated areas in Chile. Using the chemical signature imprinted on zircon by the presence of monazite in the melt as a discriminating parameter, we were able to fit an isochron on a chemically coherent population, leading to, in this case, slightly younger zircon crystallization and hence maximum eruption ages for the Pudahuel Ignimbrite.

2. Geological Setting

The Maipo volcanic complex is located in the border region between Chile and Argentina, in the Andean Cordillera (34º09'S, 69º49'W), in the northern area of the Southern Volcanic Zone, and is formed by the Diamante caldera and the Maipo stratocone (Fig. 1). The caldera formed in a VEI 7 eruption (Guerstein, 1993) which generated a voluminous ignimbrite, first described by Polanski (1963), and termed Asociación Piroclástica Pumícea. The deposit has been otherwise termed the Pudahuel Ignimbrite in Chile and the Diamante Tuff in Argentina (e.g., Wall et al., 1996 and Harrington, 1989 respectively). Its volume has been estimated at 270 km^3 (135 km^3 dense rock equivalent; DRE), distributed as 20 km^3 for two plinian fall deposits and 250 km^3 for the pyroclastic density current (PDC) deposits (Guerstein, 1993; Troncoso, 2012). The Pudahuel Ignimbrite is formed by matrix-supported PDC deposits that

are present in the valleys of the Maipo and Cachapoal rivers in Chile and the valleys of the Yaucha, Rosario, and Papagayos rivers in Argentina (Fig.1). The matrix comprises a mixture of glass shards and coarse pumiceous ash. Larger clasts, in order of decreasing volumetric abundance, are composed of larger pumice lapilli and blocks (up to 18 cm), crystals (dominantly plagioclase and biotite), lithics of basement rock (Hynek et al., 2010; Troncoso, 2012) and obsidian (Troncoso, 2012). Pumice with color variations between pink, light gray and white and gray banded, have been described by Burkert et al., (2010). Pumice clasts are mainly glassy (~98%) with phenocrysts of plagioclase (~2%) and biotite (~0.5%), as well as accessory minerals such as magnetite, ilmenite, zircon, monazite, and apatite (Pineda et al., 2021). On the Argentinian side, a pumice–rich fall deposit beneath the PDC has been identified as the initial plinian phase of the eruption.

Both PDC and fallout deposits are classified as rhyolitic (~73 wt.% SiO_2) and show subtle compositional variations as some fallout samples are slightly enriched in Ca, Fe, and Sr and depleted in Rb (Pineda et al., 2021). Chemical and isotopic characteristics such as high Rb and Ba (up to 156 ppm and 769 ppm respectively), low Sr and Zr (~74 ppm and ~73 ppm respectively), and high $^{87}Sr/^{86}Sr$ combined with low $^{143}Nd/^{144}Nd$ (0.70594 and 0.51255 respectively) suggest an origin from extensively fractionated mantle-derived melts strongly contaminated by a crustal component (Futa and Stern, 1988; Stern et al., 1984).

The eruption age has long been controversial as different methods yielded incoherent results. Stern et al. (1984) first applied the fission track method to zircon and obtained ages of 0.45 ± 0.06 Ma (errors are stated at 1 sigma level here and beyond); Wall et al., (2001) reported even older ages of 2.3 ± 0.3 Ma obtained by the $^{40}Ar/^{39}Ar$ biotite method, whereas Lara et al., (2008) obtained a much younger ages of ~0.15 Ma from (U–Th)/He dating of zircon. The

(U–Th)/He age is consistent with the U-Pb zircon age of 0.13 ± 0.03 Ma obtained by Pineda, (2015).

3. Methods

3.1. Sample preparation

Three composite pumices samples were selected for this study from PDC deposits located in the Chilean valleys of Maipo and Cachapoal rivers (Fig. 1), where a bag of ~15 kg of fresh and unweather pumices clasts was collected from each deposit. Pumice clasts were individually cleaned with tap water to remove any adhering ash. Then they were soaked in ultra-pure water and put into an ultrasonic cleaner for half an hour to clean out any loose material remaining in vesicles. Afterwards, the samples were dried at 100 ºC for 12 hours and gently crushed in pieces of 3 cm inside a plastic bag to prevent contamination. Crushed samples were put into a tungsten swing mill for 30–40 seconds until most material was <0.5 mm. Powders were then sieved into the 0.5 mm size fraction with a plastic sieve cloth. Samples went through a Gemini table in order to wash the sample and remove excessively tiny particles. This process allowed separating the sample into a heavy, middle, and light fractions that were dried with infrared light at ~80–90 ºC. The heavy fraction was immersed into bromoform (SG 2.89 g/cm^3) to separate the denser fraction, which was then collected and washed to remove any trace of the liquid. Zircon crystals were picked from this fraction with a brush under a binocular microscope. Crystals were briefly immersed into cold 10% HF to remove any adhering glass form their surface.

About 50 zircon crystals per sample were pressed into indium with its prismatic face parallel to the surface in order to analyze the rim of the crystal. Another 30 zircon crystals of each sample along with several monazite grains, were mounted in epoxy and polished until cores

were exposed. Both types of mounts, indium and epoxy, were carefully cleaned using ammoniacal ethylenediaminetetraacetic acid, deionized water, and methanol, and subsequently gold coated. For the indium-mounted samples, backscatter images (BSE) were taken in a scanning electron microscope (SEM) to ensure no dust particles remained in the surface. For the epoxy-mounted zircon, cathodoluminescence (CL) images were obtained to identify the inner zonation patterns of the crystals.

3.2. U-Th and U-Pb

Zircon U-Th dating and REE analyses were obtained using the CAMECA ims 1280-HR ion microprobe at the Institute of Earth Sciences at Heidelberg University, Germany. Since the indium mounted zircon allows to get information of the youngest domain of the crystals, we prioritized analyzing the central area of the epoxy mounted zircon crystals to obtain complementary information on the crystallization of the potentially oldest domains. When zircon grains were large enough and CL images showed textural variations, multiple analyses were performed per crystal. The U-Th relative sensitivity factor was calibrated for AS3 as described by (Reid et al., 1997). A primary $^{16}O^-$ beam intensity of ~40 nA was used for U-Th analysis with analytical parameters for dynamic multi-collection as described in Friedrichs et al. (2020). Replicate analysis of secular equilibrium zircon reference AS3 during the course of the analytical session yielded average (^{230}Th)/(^{238}U) values of 0.990 ± 0.006 (mean square of weighted deviates MSWD = 1.29; n = 10) and 0.995 ± 0.005 (MSWD = 0.72; n = 23) for the indium and epoxy mounts, respectively.

U–Pb analyses were performed on zircons located over the equiline, in the same location of the U–Th analysis following routine procedures described in Friedrichs et al. (2020). Analytical conditions were adjusted from those of the U-Th dating session, mainly by using a weaker (and smaller) primary ion beam of ~10 nA and O_2-flooding of the sample chamber

to enhance Pb yields. In addition, U-Th-Pb monazite analyses were carried out following the zero-offset procedure in Catlos et al., (2020). As a primary reference for age, Comfort monazite (481 Ma; J. Crowley, pers. comm.) was used; additional analyses of monazite 554 (45 Ma and 130 ppm U; Harrison et al., 1999) were analyzed as a secondary reference for the Th-Pb age and to estimate U abundances. Thorium abundances were then calculated from measured $^{232}Th/^{238}U$ with a relative sensitivity calibrated from $^{208}Pb/^{206}Pb$ on Comfort monazite following Reid et al. (1997).

Five crystals from the indium-mounted samples were re-mounted in epoxy by rotating them 90° relative to their original orientation during SIMS depth profiling. This was done to carry out CL imaging across laterally exposed crystal domains that were penetrated by the ion beam in SIMS depth profiling. Surface profiles were recorded on a pair of indium-mounted zircon crystals with a Bruker DektakXT stylus profilometer to measure crater depths on the zircon surfaces.

3.3. Zircon trace elements

Key trace elements including the complete suite of REE were also analyzed by SIMS for some of the zircons mounted in epoxy. The analysis was made in the same spot that the U-Th data was collected. An additional location was picked on each of these crystals near the outer rim to detect any variation along the growth of zircon.

Phosphorous, Mn, Mg and Fe were measured along with REE to monitor beam overlap onto inclusions accidentally sampled by the ion beam. Data with relatively high amount of P (>2500 ppm) or a high Fe, Ti, Mn and Mg were considered to be affected by apatite or Fe–Ti oxide inclusions, and hence discarded (see Appendix A). Contamination by non-zircon phases was also tested by applying the LREE index (LREE-I = Dy/Nd+Dy/Sm) (Bell et al.,

2019) with a value of 50 as a threshold. Data with anomalous REE patterns were also excluded from further consideration (Appendix A).

3.4. Accessory mineral temperatures and fO_2

Zircon crystallization temperatures were determined by applying the Ferry and Watson (2007) Ti-in- zircon thermometer, where Titanium dioxide activity ($a\mathrm{TiO_2}$ =0.8) was calculated from ilmenite and magnetite pairs present in sample CPIP13 according to the Fe–Ti oxide geothermobarometer (Ghiorso and Evans, 2008). Even though quartz has not been described in the ignimbrite, its high amount of silica allows us to consider a silica activity of unity for the thermometer application ($a\mathrm{SiO_2}$ = 1). Resulting temperatures were used alongside the Smythe and Brenan (2016) model to determine magmatic oxygen fugacity for zircons, considering whole rock published values and a water content of 6 wt.% (Pineda et al., 2021). The Loucks et al. (2020) pressure-corrected calibration was also applied to compare the obtained temperatures and oxygen fugacities for zircon.

Saturation temperatures for apatite, monazite and zircon were calculated from published whole rock pumice values which in this case are good proxies for the melt composition as crystallinity is only ~ 3%. Apatite saturation temperatures were determined using the Harrison and Watson (1984) model. For monazite we used the Montel (1993) model considering the recommended value of X^{REE}_{Mnz}= 0.83; when applied, this model yielded coherent magmatic temperatures whereas the pressure-corrected Maimaiti et al., (2019) model reaches temperatures significantly below the solidus (<650 ºC; Holtz and Johannes, 1994), which seems inconsistent with the idiomorphic crystal morphology of monazite suggestive of magmatic crystallization. Zircon saturation temperatures were calculated using the Shao et al. (2020) model 2.

4. Results

4.1. Cathodoluminescence imaging

Zircon crystals analyzed are on average 220 μm in length with an average aspect ratio of 5. CL images show usually a faintly visible zoning pattern in many of the crystals (Fig. 2a), with common features such as partial resorption and overgrowth in the last rim (Fig. 2c, Appendix B). Some crystals feature oscillatory zonation with smooth grey scale variations (Fig. 2b). Most crystals display grey bright cores, although some of them present a darker core surrounded by a bright grey zone (Fig. 2d).

4.2. U–Th ages

U–Th ages were obtained for surfaces and interiors of 120 crystals and were calculated from linear regression of the zircon data, as no information of whole rock U–Th isotopic composition is available. For calculating the age, we carefully examined intensity variations in each U–Th analysis. Although Th/U in zircon often remained invariant a single analysis (Fig. 3a), in some cases marked differences in these values were identified during the 45 cycles of an individual analysis, generally with elevated Th/U towards the end (Fig. 3b), or in some cases the middle of the depth profile (Fig. 3c).

The calculated U–Th isochron age after integration over all analysis cycles (“all”) is 186 ± 4 ka (MSWD = 0.99; n =108) (Fig. 4a, Appendix C.1). However, if the Th/U variations within each analysis profile are considered, the analysis can be divided into "first" and "last" cycles of variable length. These considerations change the U-Th isochron age to 180 ± 3 ka (MSWD =1.3; n = 142) (Fig. 4b, Appendix C.2). Separation between zircon surfaces and interiors alone produced no significant differences in ages. The effects of dividing the entire population according to zircon Th/U are presented in the discussion.

4.3. U-Pb and Pb-Th ages

For 11 zircon crystals that were in or above the equiline (considering the error bar) U–Pb ages were obtained (Appendix C.3). Most of them (9 crystals) are xenocrysts with ages that vary between 1145 ± 30 Ma to 2.0 ± 0.3 Ma. Pb-Th ages and compositional data were also obtained for six monazite crystals to confirm that they were not xenocrysts and that they grew along with zircon (Appendix D). In all cases, the low radiogenic ^{208}Pb in monazite indicates ages close to or below the limit of quantification. Thorium abundances vary widely between 1.9 and 8.0 wt.% ThO_2, confirming the strong preference of monazite for Th over U (Th/U monazite = 129 – 275).

4.4. Ti zircon temperatures

Ti-in-zircon temperatures obtained using the Ferry and Watson (2007) Ti-in-zircon thermometer (Appendix C.4), excluding xenocrysts, vary from 647 to 872 ºC, with an average value of 728 ± 53 ºC (n = 116). In general, when center and intermediate domains were analyzed for the same crystal, temperature decreased toward the outer parts with only two exceptions, in which temperature showed minor increases (between 4 and 22 ºC). In other crystals, variations between center and intermedium parts are on average ~89 ºC. This trend continues for zircon surfaces where Ti-in-zircon temperatures are on average 25 ºC lower than for cores (730 ºC and 755 ºC respectively). Temperatures obtained with the Loucks et al. (2020) pressure-corrected model are ~55 ºC higher when storage pressures of 350 MPa are considered (Pineda et al., 2021), and even higher at lower pressures.

4.5. Other accessory minerals constraints

Ti-in-zircon temperatures were used in the Smythe and Brenan (2016) model to determine melt redox conditions during zircon crystallization. For crystals interiors, values of $\log fO_2$ range from -19.5 to -10 (average = -15.7), and for zircon surfaces, $\log fO_2$ values range from

-19.4 to -11.3 (average = -15.1); broadly similar values were obtained by using the Loucks et al., (2020) calibration adjusted for P = 300 MPa. Saturation temperatures calculated for apatite, zircon, and monazite show a systematic decrease with temperatures of 856 ± 5 ºC, 755 ± 9 ºC, and 714 ± 5 ºC, respectively. Stated uncertainties are from averaging the compositional variability of the samples investigated; systematic uncertainties of the calibrations are typically ± 35 °C (Putirka, 2017).

4.6. Trace elements

Chondrite-normalized REE patterns for zircon show LREE-depleted patterns with an $(Sm/La)_N$ average value of ~108 (total range 1.3 – 495) and HREE enrichment with a $(Lu/Gd)_N$ average value of 40 (total range 14.8 – 72.5) (Fig. 5). Patterns display positive Ce anomalies (Ce/Ce*=1.86 – 202.5), whereby zircon surfaces have lower values than mantle and core areas. Negative Eu anomalies (Eu/Eu*=0.04 – 0.67) where marked CL differences between the analyzed zones of the crystal are lacking. Values for Ce/Ce* and Eu/Eu* in zircon decrease with lower Ti-in zircon temperatures (Fig. 6a–c). Hafnium abundances vary between ~7600 and ~16000 ppm (Appendix C.4), with the lowest values also associated with low Ti-in-zircon temperatures, whereas Zr/Hf ratios, computed for an invariant stoichiometric Zr abundance (500,000 ppm), range from ~32 to ~66 (Fig. 6d). Thorium concentrations varies from 1.7 to 3029 ppm, with corresponding U values ranging from 62 to 2696 ppm, resulting in Th/U ratios of 0.005 to 1.91, where zircon with lower Ti-in-zircon temperatures usually correspond to lower values (Fig. 7).

5. Discussion

Zircon chemical signatures vary significantly between crystals surfaces and interiors, showing not only a variation in Th/U, but also a decrease in Ce/Ce*, Eu/Eu*, Zr/Hf, and Y

with decreasing Ti abundance, which in turn corresponds to a decrease in temperature (Fig. 6). This implies that for many zircon crystals, their last stage of crystallization occurred in melts with different compositions and temperatures compared to the earlier stages of their crystallization history. While some of the variations such as down-temperature decreases in Eu/Eu* can be explained by major phase fractionation (specifically plagioclase), the generally decreasing REE availability with decreasing temperature also indicates a strong influence of accessory minerals, which we further evaluate in terms of zircon Th/U.

5.1. Zircon thermometry and oxybarometry

Average surface Ti-in-temperatures (~730 ºC) show a good correlation with pre-eruptive temperature conditions determined for the Pudahuel magma reservoir (Pineda et al., 2021). Both mineralogical and experimental constrains showed low reservoir temperatures of 700 – 750 ºC, equivalent to the lower range of Ti-in-zircon temperatures. Minor reheating prior to eruption may have occurred as suggested by Ti-in-zircon temperatures at near-liquidus temperatures of ~650 °C. Zircon would respond very sluggishly to reheating, whereas Fe-Ti-oxides would approach new equilibrium conditions more rapidly. Oxygen fugacity (fO_2) estimated for zircon yielding low temperatures agrees well with that obtained from Fe-Ti oxides (Fig 8; Ghiorso and Evans, 2008). However, when the Loucks et al. (2020) pressure correction (for 300 MPa; Pineda et al., 2021) is applied, apparent zircon crystallization temperature increase by ~50 to 100 °C, and fO_2 associated with zircon would generally exceed those obtained from Fe-Ti oxides.

There is a clear decrease in fO_2 with temperature, which correlates with other indicators such as Eu/Eu*, Ce/Ce* and Th/U in zircon. Europium and Ce can be present in the melt not only as trivalent cations but also as Eu^{2+} and Ce^{4+} respectively, so their incorporation into the zircon lattice will ultimately depend on cation valence. Partitioning of these elements into

the zircon would be influenced by the prevailing oxygen fugacity conditions, but in the case of Eu^{3+}/Eu^{2+}, as mentioned before, it can also be explained by fractional crystallization of plagioclase. Although there is a decrease in zircon surface fO_2, the Ce anomaly remains relatively constant, whereas for interior crystal zones there is a wider range of Ce/Ce* variation along with fO_2. We suspect that co-crystallization of another phase competing for Ce^{4+} affects zircon Ce/Ce* at low temperatures, monazite being the prime candidate.

5.2. Monazite controlling Th/U in zircon

The sudden and pronounced variations of Th/U along depth in individual zircon analyses are suggestive of a change in the availability of these elements in the magma where zircon crystals grew. The incorporation of any element into a crystal lattice is influenced by the thermochemical variations in bulk composition of the whole system and further modulated by changes in crystal-melt partitioning behavior expressed by partitioning values D (e.g., Rubatto and Hermann, 2007). Variations in the abundance of elements in melts that are preferentially incorporated into the zircon lattice such as Y, HREE, Th, and U are often strongly controlled by accessory minerals, whereas fractionation of major minerals plays a lesser role (Bea, 1996; Miller and Mittlefehldt, 1982; Nardi et al., 2013). Zircon-melt D values for Th and U (D_{Th}, D_U) increase with decreasing temperature, but available experiments (e.g., Rubatto and Hermann, 2007; Luo and Ayers, 2009) lack evidence for a strong temperature-dependent change in D_{Th}/D_U (cf. Kirkland et al., 2015). Another factor influencing D_U is oxygen fugacity, where UO_2^{2+} present under high-fO_2 conditions would be less compatible in zircon compared to U^{4+} prevalent under low-fO_2 conditions (Burnham and Berry, 2012). Our data show a decrease in oxygen fugacity with temperature and Th/U in zircon (Fig. 8) which evidence a gradually reducing magmatic environment upon crystallization, which in turn could contribute to changing D_{Th}/D_U. However, changes in

Th/U in Pudahuel Ignimbrite zircon depth profiles are mostly due to variability in Th (Fig. 3), and thus variability in D_U is deemed of secondary importance. We therefore honed in on exploring the fractionation of accessory minerals progressively changing the availability of Th vs. U in the melt.

Pudahuel Ignimbrite samples show petrographic evidence for accessory minerals such as magnetite, ilmenite, apatite, zircon, and monazite. Apatite and monazite incorporate REE into their structures and therefore will affect zircon compositions if they are growing in the same melt. Monazite incorporates Th, U and REE, and strongly prefers Th over U (Breiter, 2016), which implies that Th/U in zircon will decrease when the melt becomes saturated in monazite because of the progressively reduced availability of Th in the remaining melt. Because zircon incorporates more easily U^{4+} than Th^{4+} due to the smaller ionic radius of U^{4+} being closer to the ideal, near-Zr^{4+} cation radius (Shannon, 1976), the melt will also become more depleted in U relative to Th. The effect of monazite fractionation is therefore somewhat mitigated by an expected increase in Th/U resulting from zircon fractionation. At the same time, Zr/Hf in zircon decreases with zircon fractionation in progressively more differentiated and colder melts (Linnen and Keppler, 2002). Co-precipitation of a Th-scavenging phase is thus required to explain the positive relation observed between Th/U and Zr/Hf in zircon (Schaltegger and Davies, 2017).

Apatite is also an accessory mineral present in Pudahuel rhyolite which, like monazite, incorporates into is structure REE elements, Th^{4+} and in lesser amount U^{4+} (Pan and Fleet, 2019). Therefore, its presence could also explain, in a similar way as the presence of monazite, the progressive Th/U decrease as zircon crystallized. The saturation temperature for apatite in the Pudahuel melt is 856 ± 5 ºC (Harrison and Watson, 1984), near the highest Ti-in-zircon temperatures recorded by some zircon crystals, whereas the saturation

temperature for zircon is 755 ± 9 ºC (Shao et al., 2020). This indicates that both minerals crystallized together and thus apatite could also affect Th/U in zircon. However, although apatite continues to crystallize in the melt until the solidus is reached, most apatite will crystallize within 60–100 ºC of its saturation temperature (Piccoli and Candela, 1994, 2019). This implies that apatite has little effect on zircon below temperatures of ~760 ºC, where most zircon appears to have crystallized. This is also supported by a lack of correlation between Ti and P in zircon (correlation factor r = 0.24). The saturation temperature of monazite is 714 ± 5 ºC according to the model of Montel (1993), which in comparison with Ti-in-zircon temperatures indicates that both accessory phases co-precipitated at near-solidus temperatures (Fig. 7). Therefore, and because of the much higher D_{Th} for monazite compared to apatite, monazite likely exerts the strongest control on Th/U in zircon, at least at low magmatic temperatures. This is supported independently of the absolute temperatures estimated from different saturation and trace element partitioning calibrations by evidence from depth profiling that indicates a sudden rimward drop in zircon Th/U suggestive of a down-temperature change in melt composition due to crystallization of a high-Th phase.

Many zircon crystals, however, also display higher Ti-in-zircon temperatures than the zircon saturation temperatures calculated for Pudahuel Ignimbrite. This could be due to systematic uncertainties in the different thermometer calibrations, but Bacon (1989) pointed to an alternative explanation: crystallization of accessory minerals such as zircon can occur before the saturation temperature in the melt is reached, as they can nucleate adjacent to crystallizing phenocrysts where the crystal-melt interface can become locally supersaturated. Zircon with Ti-in-zircon temperatures above the zircon saturation temperature could have formed in this way, growing near ferromagnesian minerals such as biotite, whose crystals in rhyolite often contain zircon inclusions. This process also enhances fractionation of accessory minerals that

are enclosed in phenocrysts which are more readily mechanically separable (Bacon, 1989; Harrison and Watson, 1984). Taking the ~100°C difference between the zircon saturation temperature and the highest Ti-in-zircon temperatures as a measure for the temperature interval where local supersaturation sensu Bacon (1989) can occur, and adding this to the monazite saturation temperature, suggests that local monazite saturation could be reached at temperatures as high as 800 °C. This encompasses the entire range of Ti-in-zircon temperatures where a decrease of Th/U in zircon with decreasing temperature is observed (Fig. 7; Kirkland et al., 2015). Data from Pudahuel Ignimbrite thus suggest that monazite saturation plays a predominant role in controlling zircon Th/U over a wide temperature range. Whether similar considerations also apply to allanite in zircon-crystallizing melts awaits further study.

5.3. Implications for Th-U ages

Th/U in zircon with Ti-in-zircon temperatures below monazite saturation is <0.6, and the corresponding (^{238}U)/(^{232}Th) activity ratios are >5.2 (Fig. 7). Zircon (^{238}U)/(^{232}Th) >5.2 were mainly detected for zircon surfaces, and at lesser degrees for intermediate crystal domains. By contrast, zircon analyses with (^{238}U)/(^{232}Th) <5.2 correspond mainly to the last cycles of individual depth profiles and thus predate those with higher (^{238}U)/(^{232}Th) (Fig. 9). Using the thermometric constraint on monazite saturation (Fig. 7) as a filter for absence vs. presence of monazite during zircon crystallization, we calculated regression ages for zircon crystallized at higher temperatures (monazite-absent or scarce) and lower temperatures (monazite-present or abundant), and obtained ages of 177 ± 4 ka (MSWD=0.91) and 167 ± 8 ka (MSWD= 1.7), respectively. Although both ages overlap within uncertainty, we prefer the younger age as a more realistic proxy for the eruption age.

6. Conclusions

Zircon chemistry from the Pudahuel ignimbrite shows diminishing Th/U along with a decrease in Ti-in-zircon temperatures that can be explained by the presence of accessory monazite which strongly depletes the remaining melt in Th. Monazite saturation temperatures for Pudahuel glass compositions suggest that the coolest zircon crystals grew along with monazite and therefore their chemical signature was affected by it. This influence is also identified in individual U–Th geochronology depth profiles showing that the influence of monazite can be recorded in a single crystal and that it is most prevalent at the crystal rims. Ages calculated after separating zircon domains according to their U–Th activity ratios differ slightly from those calculated without this consideration. Cooler zircon domains that crystallized coexisting with monazite yielded the youngest age of all attempted regressions. The resulting age of 167 ± 8 ka overlaps with previously published U-Pb and (U–Th)/He zircon ages, but is much younger than $^{40}Ar/^{39}Ar$ ages reported in the literature. Although strictly a minimum age for the eruption, the zircon crystallization age filtered to only include late crystallized, and (in the case of Pudahuel Ignimbrite) low-temperature zircon, is presently the most precise estimate for the eruption age. This stresses the importance of taking into account chemical indicators in zircon when dating, especially when investigating Quaternary eruptions where accurate determination of the eruption age is important to assess volcanic hazards.

Down-temperature decreasing Th/U in zircon which crystallized at temperatures higher than monazite saturation could be affected by apatite fractionation, which also preferentially incorporates Th over U into its structure. However, its influence will be mainly restricted to 60–100 ºC below apatite saturation in the melt, and may be minor due to overall low D_{Th} and D_U in apatite. Zircon crystals with Ti-in-zircon temperature above the zircon saturation

temperature are often interpreted to originate from melt-phenocryst interfaces, where local chemical differentiation promotes supersaturation and crystallization of accessory minerals (Bacon, 1989). When trapped in phenocrysts, these accessory minerals can be efficiently scavenged from the melt. If this not only applies to zircon but also monazite, then monazite could exert a strong control on Th/U in zircon over a significant range of the zircon stability field in evolved magmas.

7. Acknowledgments

This study was made possible by funding from the ANID-Fondap 15090013 & 15200001 project "Andean Geothermal Center of Excellence (CEGA)" and by National Agency for Research and Development (ANID)/ Scholarship Program/ Doctorado Nacional/ 2016-21160376. We thank Alejandro Cisneros de León for assistance collecting and analyzing ion microprobe and SEM data. We thank Christian Betancourt for comments and suggestions.

8. References

Bacon, C.R., 1989. Crystallization of accessory phases in magmas by local saturation adjacent to phenocrysts. Geochim. Cosmochim. Acta 53, 1055–1066. https://doi.org/10.1016/0016-7037(89)90210-X

Bea, F., 1996. Residence of REE, Y, Th and U in granites and crustal protoliths; implications for the chemistry of crustal melts. J. Petrol. 37, 521–552. https://doi.org/10.1093/petrology/37.3.521

Bell, E.A., Boehnke, P., Barboni, M., Harrison, T.M., 2019. Tracking chemical alteration in magmatic zircon using rare earth element abundances. Chem. Geol. 510, 56–71. https://doi.org/10.1016/j.chemgeo.2019.02.027

Breiter, K., 2016. Monazite and zircon as major carriers of Th, U, and Y in peraluminous granites: examples from the Bohemian Massif. Mineral. Petrol. 110, 767–785. https://doi.org/10.1007/s00710-016-0448-0

Burgess, S.D., Coble, M.A., Vazquez, J.A., 2021. Zircon geochronology and geochemistry of Quaternary rhyolite domes of the Coso volcanic field, Inyo County, California. J. Volcanol. Geotherm. Res. 417, 107276. https://doi.org/10.1016/j.jvolgeores.2021.107276

Burkert, C., Freundt, A., Gilbert, D., Kutterolf, S., 2010. Origin of magmatic components in the Diamante Tuff, in: SFB 574 Subduction Workshop. Pucón.

Burnham, A.D., Berry, A.J., 2012. An experimental study of trace element partitioning between zircon and melt as a function of oxygen fugacity. Geochim. Cosmochim. Acta 95, 196–212. https://doi.org/10.1016/j.gca.2012.07.034

Catlos, E.J., Perez, T.J., Lovera, O.M., Dubey, C.S., Schmitt, A.K., Etzel, T.M., 2020. High-Resolution P-T-Time Paths Across Himalayan Faults Exposed Along the Bhagirathi Transect NW India: Implications for the Construction of the Himalayan Orogen and Ongoing Deformation. Geochemistry, Geophys. Geosystems 21, 1–29. https://doi.org/10.1029/2020GC009353

Cheng, H., Lawrence Edwards, R., Shen, C.C., Polyak, V.J., Asmerom, Y., Woodhead, J., Hellstrom, J., Wang, Y., Kong, X., Spötl, C., Wang, X., Calvin Alexander, E., 2013. Improvements in 230Th dating, 230Th and 234U half-life values, and U-Th isotopic measurements by multi-collector inductively coupled plasma mass spectrometry. Earth Planet. Sci. Lett. 371–372, 82–91. https://doi.org/10.1016/j.epsl.2013.04.006

Cooper, K.M., Reid, M.R., 2008. Uranium-series crystal ages. Rev. Mineral. Geochemistry 69, 479–544. https://doi.org/10.2138/rmg.2008.69.13

Ferry, J.M., Watson, E.B., 2007. New thermodynamic models and revised calibrations for the Ti-in-zircon and Zr-in-rutile thermometers. Contrib. to Mineral. Petrol. 154, 429–437. https://doi.org/10.1007/s00410-007-0201-0

Friedrichs, B., Schmitt, A.K., McGee, L., Turner, S., 2020. U–Th whole rock data and high spatial resolution U–Th disequilibrium and U–Pb zircon ages of Mt. Erciyes and Mt. Hasan Quaternary stratovolcanic complexes (Central Anatolia). Data Br. 29, 105113. https://doi.org/10.1016/j.dib.2020.105113

Futa, K., Stern, C.R., 1988. Sr and Nd isotopic and trace element compositions of Quaternary volcanic centers of the Southern Andes. Earth Planet. Sci. Lett. 88, 253–262. https://doi.org/10.1016/0012-821X(88)90082-9

Gana, P., Wall, R., Gutiérrez, Á., 1996. Mapa Geológico Del Área De Valparaíso- Curacaví, Regiones de Valparaíso y Metropolitana, Servicio Nacional de Geología y Minería, Mapa Geológico Nº 1, 1 mapa escala 1:100.000. Santiago.

Ghiorso, M.S., Evans, B.W., 2008. Thermodynamics of rhombohedral oxide solid solutions and a revision of the Fe-Ti two-oxide geothermometer and oxygen-barometer. Am. J. Sci. 308, 957–1039. https://doi.org/10.2475/09.2008.01

Guerstein, P.G., 1993. Origen y significado geológico de la asociación piroclástica pumícea. Preistoceno de la Provincia de Mendoza entre los 33º30' y 34º40' L.S. Universidad Nacional de La Plata, La Plata.

Harrington, R., 1989. The Diamante Caldera and Maipo Caldera Complex in the Southern Andes of Argentina and Chile (34º 10' south). Rev. la Asoc. Geológica Argentina 19, 186–193.

Harrison, T.M., Watson, E.B., 1984. The behavior of apatite during crustal anatexis: Equilibrium and kinetic considerations. Geochim. Cosmochim. Acta 48, 1467–1477. https://doi.org/10.1016/0016-7037(84)90403-4

Holtz, F., Johannes, W., 1994. Maximum and minimum water contents of granitic melts: implications for chemical and physical properties of ascending magmas. Lithos 32, 149–159. https://doi.org/10.1016/0024-4937(94)90027-2

Hynek, S.A., Marchetti, D.W., Fernandez, D.P., Cerling, T.E., 2010. Composition, pre-eruptive zonation, and geochronologic significance of the ~450ka Diamante Tuff, Andean Cordillera (34°S), Argentina. Quat. Geochronol. 5, 591–601. https://doi.org/10.1016/j.quageo.2010.02.002

Kirkland, C.L., Smithies, R.H., Taylor, R.J.M., Evans, N., McDonald, B., 2015. Zircon Th/U ratios in magmatic environs. Lithos 212–215, 397–414. https://doi.org/10.1016/j.lithos.2014.11.021

Lara, L., Wall, R., Stockli, D., 2008. La ignimbrita Pudahuel (Asociación Piroclástica Pumícea) y la caldera Diamante (33° S): nuevas edades U–Th–He, in: XVII Congreso Geológico Argentino. p. 1365.

Linnen, R.L., Keppler, H., 2002. Melt composition control of Zr/Hf fractionation in magmatic processes. Geochim. Cosmochim. Acta 66, 3293–3301. https://doi.org/10.1016/S0016-7037(02)00924-9

Lipman, P.W., 2000. Calderas. Encycl. Volcanoes 643–662.

Loucks, R.R., Fiorentini, M.L., Henriquez, G.J., 2020. New magmatic oxybarometer using trace elements in zircon. J. Petrol. 61. https://doi.org/10.1093/petrology/egaa034

Maimaiti, M., Fabbrizio, A., Carroll, M.R., Ertel-Ingrisch, W., Abudureheman, A., Paris, E., Dingwell, D.B., 2019. Experimental study of monazite solubility in haplogranitic melts: a new model for peraluminous and peralkaline melts. Eur. J. Mineral. 31, 49–59. https://doi.org/10.1127/ejm/2019/0031-2801

Miller, C.F., Mittlefehldt, D.W., 1982. Depletion of light rare-earth elements in felsic magmas. Geology 10, 129–133. https://doi.org/10.1130/0091-7613(1982)10<129:DOLREI>2.0.CO;2

Montel, J.M., 1993. A model for monazite/melt equilibrium and application to the generation of granitic magmas. Chem. Geol. 110, 127–146. https://doi.org/10.1016/0009-2541(93)90250-M

Nardi, L.V.S., Formoso, M.L.L., Müller, I.F., Fontana, E., Jarvis, K., Lamarão, C., 2013. Zircon/rock partition coefficients of REEs, Y, Th, U, Nb, and Ta in granitic rocks: Uses for provenance and mineral exploration purposes. Chem. Geol. 335, 1–7. https://doi.org/10.1016/j.chemgeo.2012.10.043

Pan, Y., Fleet, M.E., 2019. Compositions of the apatite-group minerals: Substitution mechanisms and controlling factors. Phosphates Geochemical, Geobiol. Mater. Importance 48, 13–50. https://doi.org/10.2138/rmg.2002.48.2

Piccoli, P., Candela, P., 1994. Apatite in felsic rocks: a model for the estimation of initial halogen concentrations in the Bishop Tuff (Long Valley) and Tuolumne Intrusive Suite (Sierra Nevada batholith) magmas. Am. J. Sci. https://doi.org/10.2475/ajs.294.1.92

Piccoli, P.M., Candela, P.A., 2019. Apatite in igneous systems. Phosphates Geochemical, Geobiol. Mater. Importance 48, 255–292. https://doi.org/10.213 8/rmg. 2002.48.6

Pineda, C., 2015. Geocronología U-Pb en circones de la Ignimbrita Pudahuel. Universidad de Chile, Santiago, p. 105. Geologist Professional Degree Thesis.

Pineda, C., Hammer, J., First, E., Morata, D., 2021. Storage conditions of a caldera-forming volcanic eruption: Insights from the Pudahuel rhyolitic ignimbrite in central Chile (32° 10′S). Lithos 400–401, 106382. https://doi.org/10.1016/J.LITHOS.2021.106382

Polanski, J., 1963. Estratigrafía, neotectónica y geomorfología del Pleistoceno pedemontano

entre los ríos Diamante y Mendoza: Provincia de Mendoza, Revista de la Asociación Geológica Argentina.

Putirka, K., 2017. Geothermometry and geobarometry. Encycl. geochemistry a Compr. Ref. source Chem. Earth. Springer Int. Publ. Cham 1–19.

Reid, M.R., Coath, C.D., Harrison, T.M., McKeegan, K.D., 1997. Prolonged residence times for the youngest rhyolites associated with Long Valley Caldera: 230Th-238U ion microprobe dating of young zircons. Earth Planet. Sci. Lett. 150, 27–39. https://doi.org/10.1016/s0012-821x(97)00077-0

Rubatto, D., Hermann, J., 2007. Experimental zircon/melt and zircon/garnet trace element partitioning and implications for the geochronology of crustal rocks. Chem. Geol. 241, 38–61. https://doi.org/10.1016/j.chemgeo.2007.01.027

Schaltegger, U., Davies, J.H.F.L., 2017. Petrochronology of Zircon and Baddeleyite in Igneous Rocks: Reconstructing Magmatic Processes at High Temporal Resolution. Rev. Mineral. Geochemistry 83, 297–328. https://doi.org/10.2138/rmg.2017.83.10

Self, S., 2015. Explosive Super-Eruptions and Potential Global Impacts, Volcanic Hazards, Risks and Disasters. Elsevier Inc. https://doi.org/10.1016/B978-0-12-396453-3.00016-2

Sellés, D., Gana, P., 2001. Geología del área Talagante-San Francisco de Mostazal, Regiones Metropolitana de Santiago y del Libertador General Bernardo O'Higgins, Servicio Nacional de Geología y Minería, Carta Geológica de Chile, Serie Geología Básica 74, 1 mapa escala 1:100.000. Santiago.

SERNAGEOMIN, 2003. Mapa Geológico de Chile: versión digital, Servicio Nacional de Geología y Minería, Pubilicación Geológica Digital, Nº 4 (CD-ROM, versión 1.0). Santiago.

Shannon, R.D., 1976. Revised effective ionic radii and systematic studies of interatomic distances in halides and chalcogenides. Acta Crystallogr. Sect. A 32, 751–767. https://doi.org/https://doi.org/10.1107/S0567739476001551

Shao, T., Xia, Y., Ding, X., Cai, Y., Song, M., 2020. Zircon saturation model in silicate melts: a review and update. Acta Geochim. 39, 387–403. https://doi.org/10.1007/s11631-019-00384-4

Smythe, D.J., Brenan, J.M., 2016. Magmatic oxygen fugacity estimated using zircon-melt

partitioning of cerium. Earth Planet. Sci. Lett. 453, 260–266. https://doi.org/10.1016/j.epsl.2016.08.013

Sruoga, P., Etcheverria, M., Folguera, A., Repol, D., 2005. Programa Nacional de Cartas Geológicas Hoja Geológica 3569-I Volcán Maipo, provincia de Mendoza. Buenos Aires.

Stern, C.R., Amini, H., Charrier, R., Godoy, E., Herve, F., Varela, J., 1984. Petrochemistry and age of rhyolitic pyroclastic flows which occur along the drainage valleys of the río Maipo and río Cachapoal (Chile) and the río Yaucha and río Papagayos (Argentina). Rev. Geológica Chile 23, 39–52.

Stern, C.R., Moreno, H., López-Escobar, L., Clavero, J.E., Lara, L.E., Naranjo, J.A., Parada, M.A., Skewes, M.A., 2007. Chilean volcanoes. Geol. Soc. Spec. Publ. 147–178. https://doi.org/10.1144/goch.5

Troncoso, C., 2012. Estudio Estratigráfico y de volcanología física de la Ignimbrita Pudahuel. Universidad de Chile.

Wall, R., Gana, P., Gutiérrez, Á., 1996. Mapa Geológico Del Área De San Antonio-Melipilla, Regiones de Valparaíso, Metropolitana y del Libertador General Bernardo O'Higgins, in: Servicio Nacional de Geología y Minería, Mapa Geológico Nº 2, 1 Mapa Escala 1:100.000. Santiago.

Wall, R., Sellés, D., Gana, P., 1999. Area Tiltil-Santiago, Región Metropolitana, Servicio Nacional de Geología y Minería, Mapa Geológico Nº 11, 1 mapa escala 1:100.000. Santiago.

Wall, R.M., Lara, L.E., Perez de Arce, C., 2001. Upper pliocene-lower pleistocene $^{40}Ar/^{39}Ar$ ages of Pudahuel ignimbrite (Diamante-Maipo volcanic complex), Central Chile ($33.5^{0}S$).

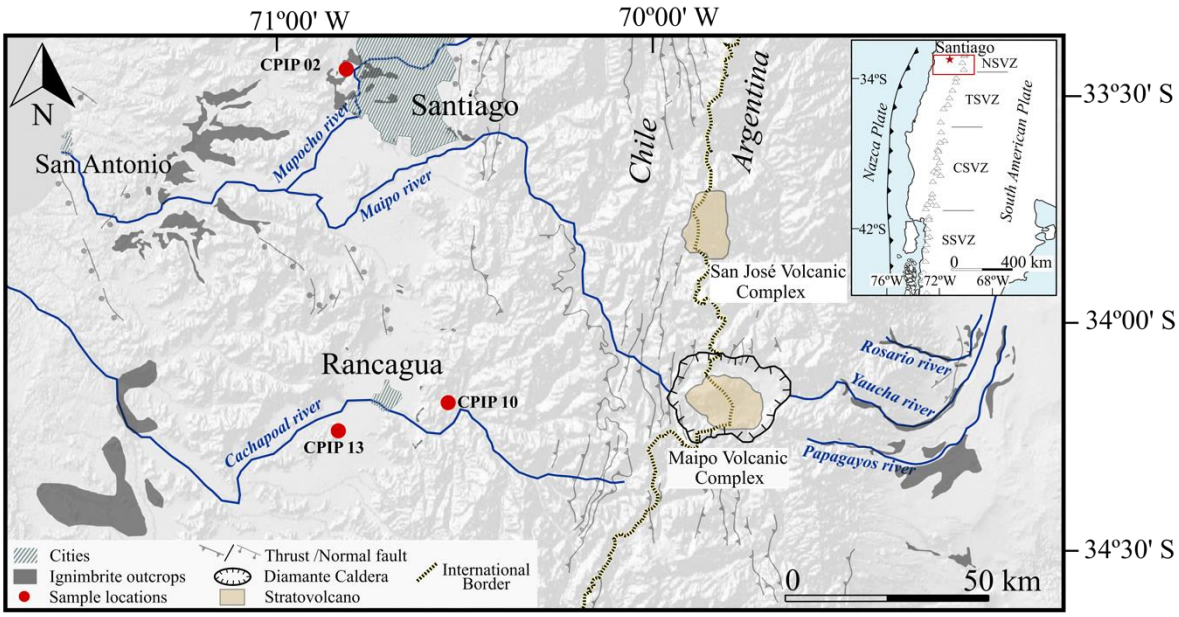

Figure 1: Regional location. Digital elevation model of Central Chile showing the outcrops of the Pudahuel Ignimbrite in grey; (data from Gana et al., 1996; Sellés and Gana, 2001; SERNAGEOMIN, 2003; Sruoga et al., 2005; Stern et al., 1984; Wall et al., 1999, 1996). Diamante caldera, Maipo volcano and cities are indicated. Locations of samples used in this study are shown in red circles. Inset figure shows location and volcanoes of the South Volcanic Zone (SVZ) and its segments: northern, transition, central and southern volcanic zones (NSVZ, TSVZ, CSVZ and SSVZ respectively), modified from Stern et al., (2007).

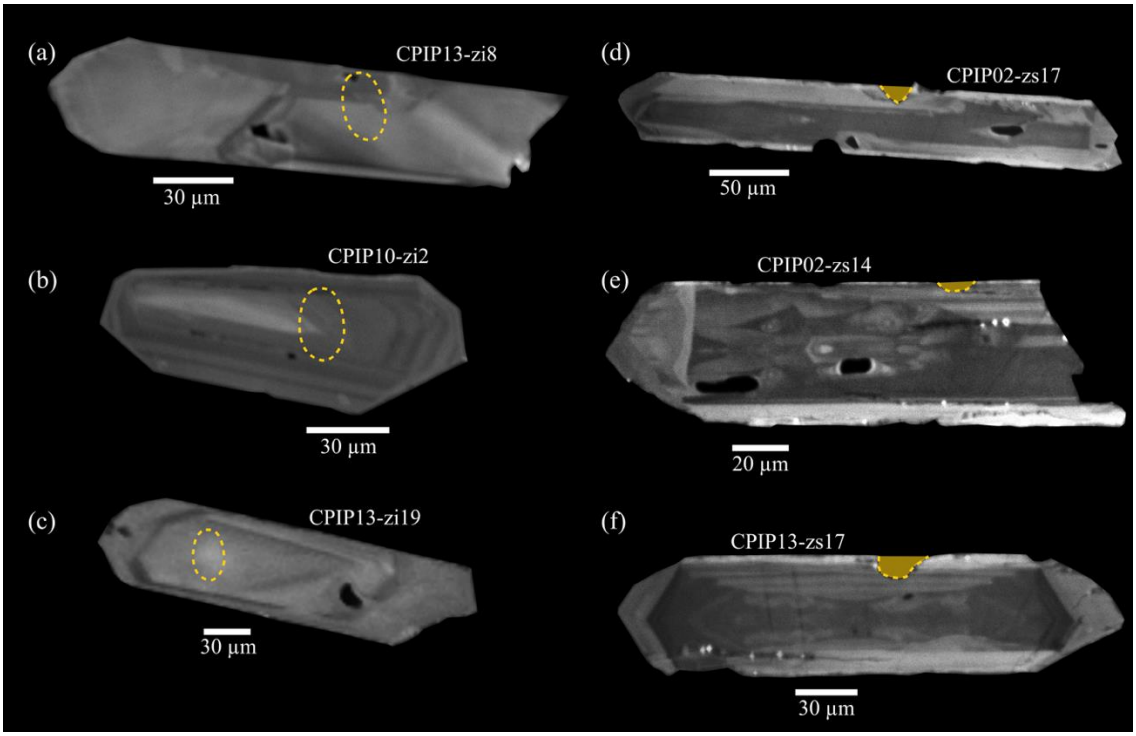

Figure 2: Representative zrn CL images to show textural variations. Analysis area showed in yellow; a—c show zrn where analyses were made in crystal interiors (zi); d–f show zrn where analyses were made in crystal surfaces (zs). a) faintly visible zoning pattern, b) oscillatory zonation, c) minor oscillatory zonation with partially resorbed core and CL-dark mantle, d) oscillatory zonation with thin CL-bright overgrowth, e) apparent xenocrystic core with thin CL-bright overgrowth, f) oscillatory zonation with sector zoning in the core and CL-bright prism faces.

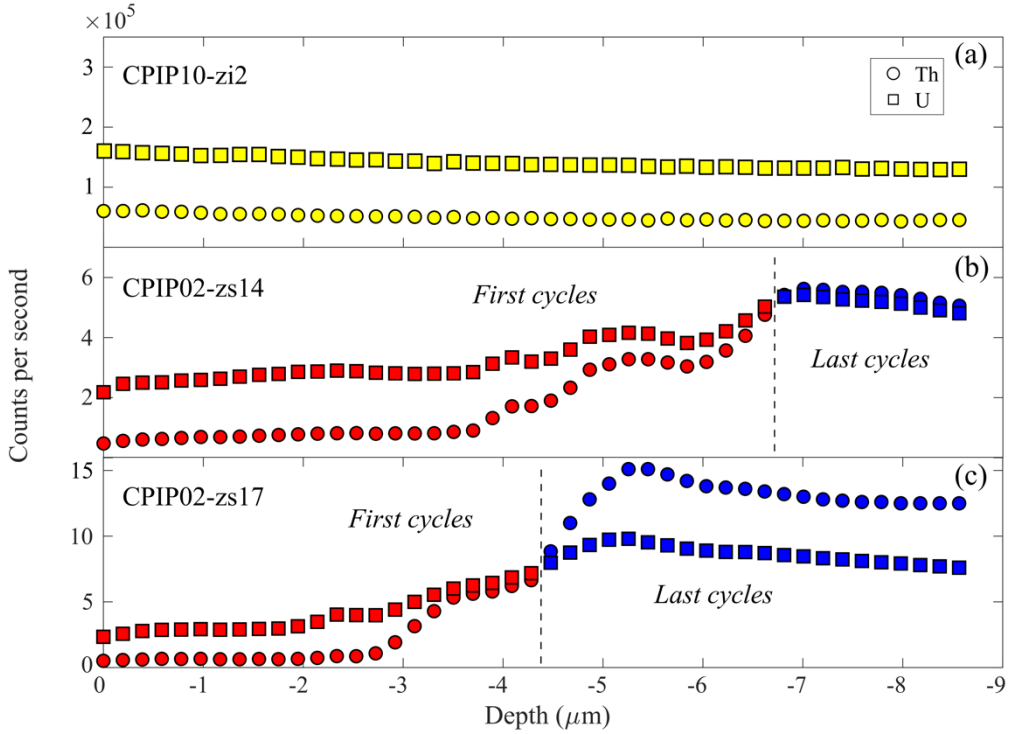

Figure 3: U-Th counts per second along a single zircon analysis. (a) U-Th measure relatively constant along zircon depth, (b) U-Th variation along zircon depth, (c) U-Th ratio variation along zircon depth. Differentiation between first and last cycles marked in (b) and (c).

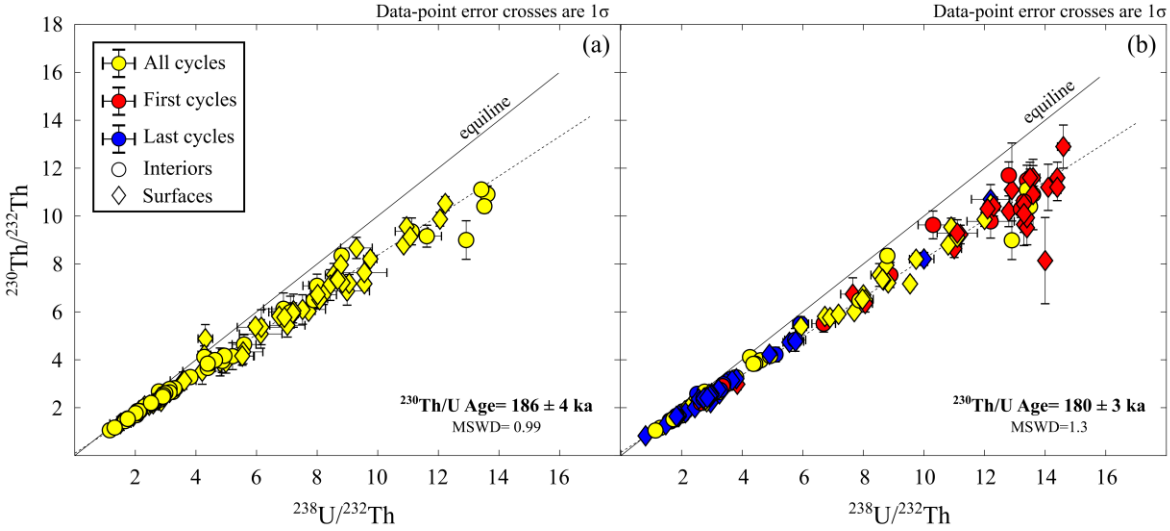

Figure 4: $^{230}Th/^{232}Th$ versus $^{238}U/^{232}Th$ isochrons for zircons regression of the Pudahuel Ignimbrite. (a) Age calculated for zircon with no cycle separation, (b) age calculated for zircon separating first and last cycles according to the U–Th behaviour.

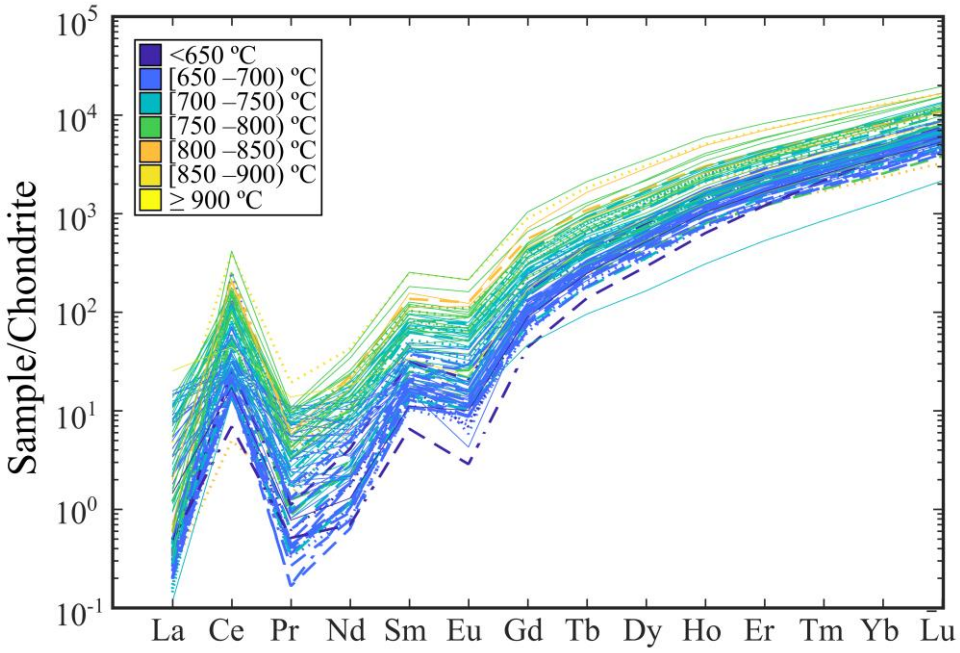

Figure 5: REE patterns normalized to chondrite for zircon crystals. Dotted, dashed and solid lines represent cores, intermedium, and surfaces crystal areas respectively. Ti-in-zircon temperatures are shown.

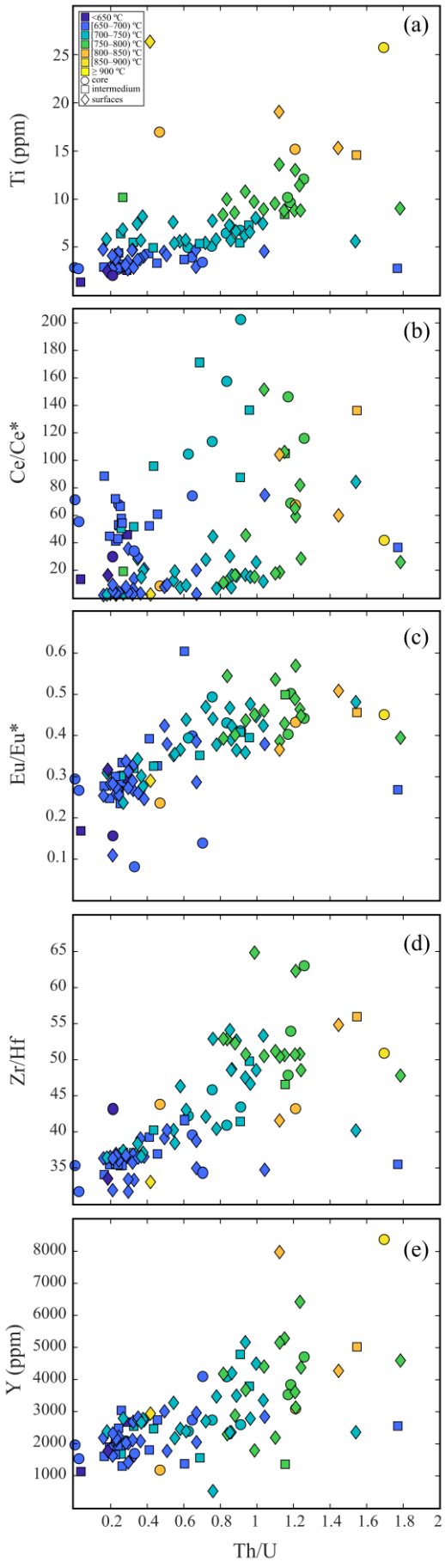

Figure 6: Zircon trace elements. Ti-in-zircon temperatures calculated using the Ferry and Watson (2007) calibration and assuming $aSiO_2 = 1$ and $aTiO_2 = 0.8$ (see text) are show.

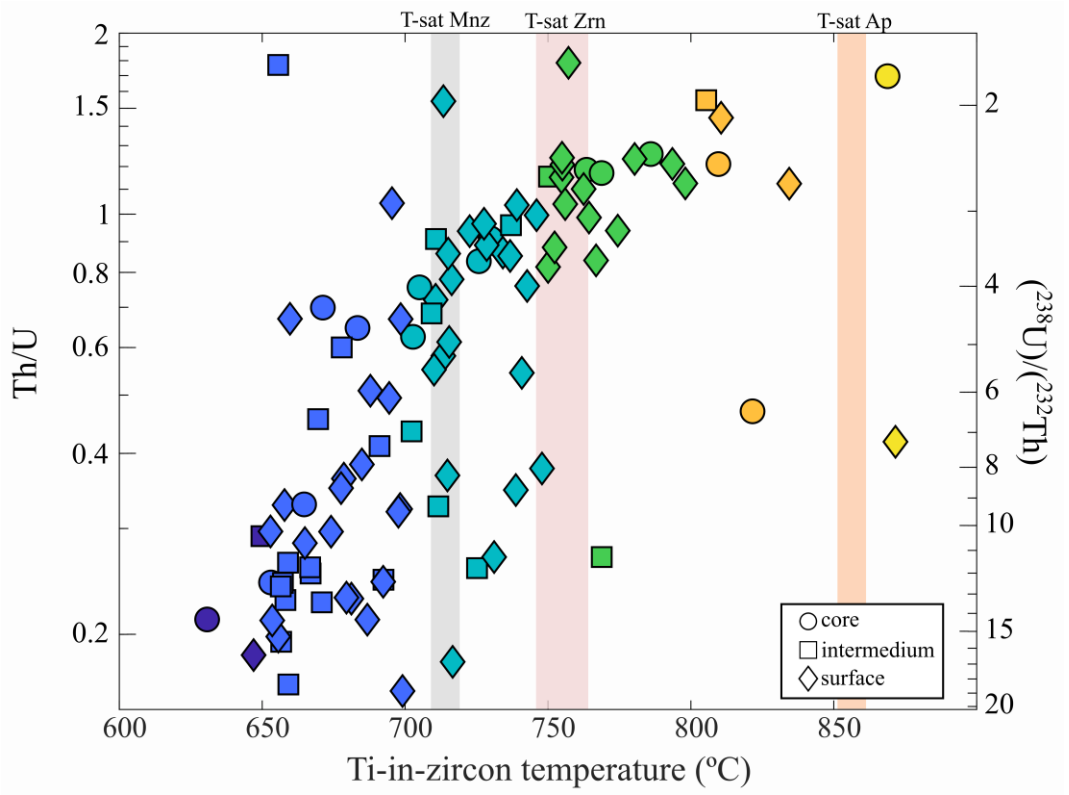

Figure 7: Zircon temperature relation with Th/U ratios and U–Th activity ratio. T-sat mnz, T-sat zrn, T-sat ap are respectively monazite and zircon saturation temperatures calculated for Pudahuel rhyolite.

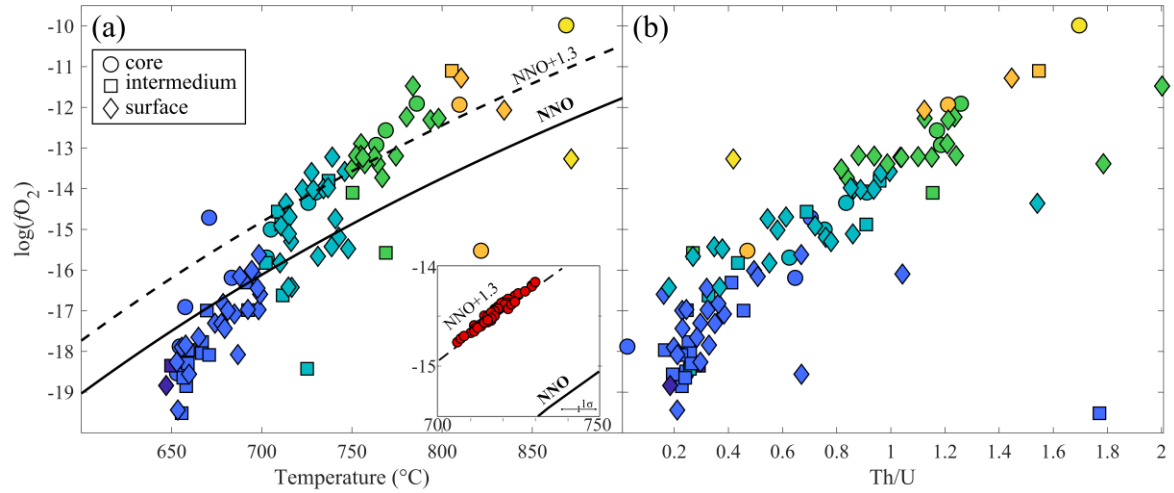

Figure 8: Oxygen fugacity relation with (a) Temperature and fO_2 (NNO + 1.3) calculated for zircon trace elements (Ti, Ce, U; see text) and for Fe-Ti oxides (using the calibration of Ghiorso and Evans, 2008; inset) and (b) fO_2 vs. Th/U ratios for zircon. Symbols as in Figure 7.

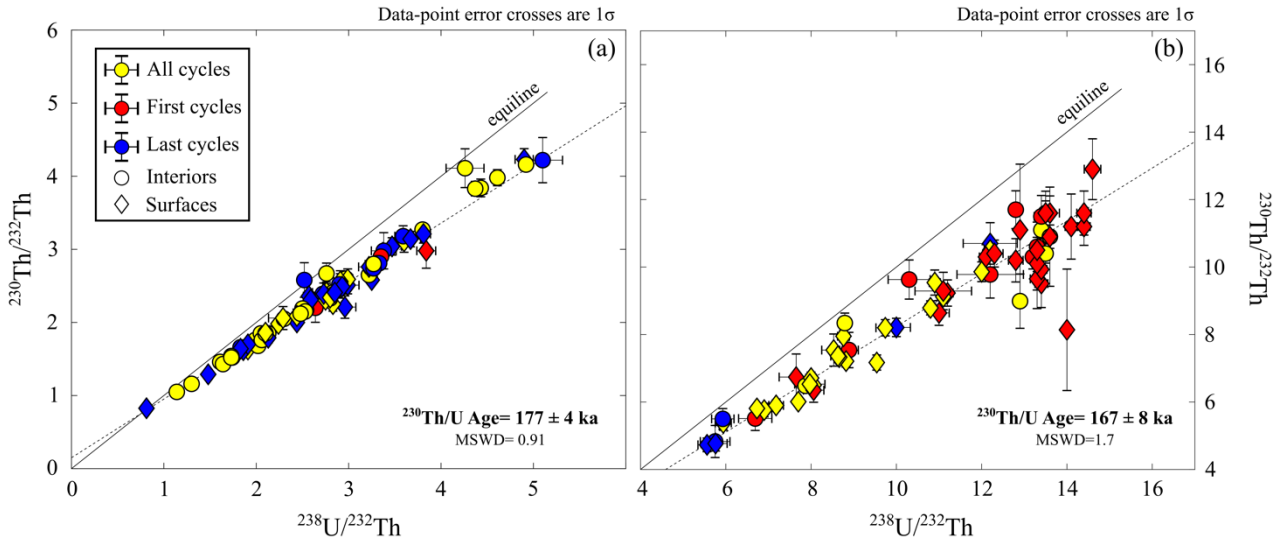

Figure 9: $^{230}Th/^{232}Th$ versus $^{238}U/^{232}Th$ isochrons for zircons regression separating according Ti-in-zircon temperature over and under monazite saturation temperature in the Pudahuel Ignimbrite (see text discussion).

Chapter 4: Storage conditions of a caldera-forming volcanic eruption: Insights from the Pudahuel rhyolitic ignimbrite in central Chile (32º 10'S)

Abstract

The Pudahuel Ignimbrite is a rhyolitic, crystal poor deposit associated with the formation of the Diamante caldera in the Southern Volcanic Zone of the Andes. This Quaternary ignimbrite is the result of a massive eruption in what is now a densely populated area. The goal of this study is to understand the origin of this caldera-forming eruption by determining the pre-eruptive magmatic conditions through analytical and experimental approaches. The Fe-Ti oxide geothermometer and the plagioclase hygrometer were used to determine the temperature-X_{H2O}^{fl} conditions that produce the glass, feldspar, and Fe-Ti oxide compositions observed in the natural sample. The results were combined with a composition-dependent water solubility model to constrain the magma storage pressure. This methodology was extended to temperatures up to 850 ºC to define a band of P-T-H_2O conditions that satisfy the natural plagioclase and glass compositional pairs, from 700 ºC at 310 MPa to 850 ºC at 85 MPa. Phase equilibrium experiments were performed at conditions within the band at H_2O-vapor saturated and undersaturated conditions using a representative pumice sample as the starting material. The purely analytical approach, based on Fe-Ti oxide geothermometry and plagioclase hygrometry of the pumice phases, suggests pre-eruptive temperatures of 717±7 ºC, P_{H2O} of 200-360 MPa and between 6.9 and 7.6 wt. % H_2O. The natural phase assemblage and the glass composition was best reproduced by experiments performed at low temperatures (700-750 ºC) and high P_{Total} (>275 MPa, more likely 300-350 MPa), with water contents of at least 6 wt.%. A compositional match between synthetic and natural glasses occurred in some H_2O-undersaturated experiments, suggesting that the melt was not necessarily saturated with H_2O-rich fluid. Overall, our work highlights that the source region related to the caldera-forming Pudahuel ignimbrite was relatively deep (> 10 km). This depth, combined with the low crystallinity of the magma, and the possibility of an H_2O-undersaturated melt, suggest that caldera formation was likely initiated by an external trigger rather than internal pressurization due to volatile buildup in the reservoir. The storage

conditions determined in this study lay the groundwork for continuing work to understand the Maipo volcanic complex and the future hazards it poses.

Keywords

Andes, rhyolite, experimental petrology, caldera-forming eruption

1. Introduction

Caldera-forming eruptions produce large volumes (>100 km^3) of magma, typically involving highly evolved crystal-poor melt (Deering et al., 2011; Hildreth, 1981; Lindsay et al., 2001a; Lipman, 2007). These eruptions are among the most destructive geologic events on Earth and, depending on their magnitude, could change the climate at a regional or even global scale (Gottsmann and Martí, 2008; Lipman, 2000). Moreover, volcanoes poised to generate caldera-forming eruptions in the vicinity of densely populated areas pose a significant risk to life and property (Self, 2015). A complete characterization of the volcanic system, combined with volcanic monitoring, can help to anticipate and prevent possible catastrophes (National Academies of Sciences and Medicine, 2017). A characterization of the conditions culminating in a caldera-forming eruption— particularly the depth from which magma is staged prior to eruption— is therefore crucial to improving our understanding of these catastrophic events, and ultimately, mitigating the associated hazards. These eruptions can start when magmatic overpressure generates upward-propagating dikes which ultimately lead to the evacuation of a substantial magma volume and culminate with caldera collapse (Druitt and Sparks, 1984). This mechanism, a type of internal trigger, can be related, for instance, to the arrival of a hotter melt into the system (e.g., Bachmann, 2010; Pallister et al., 1992). Alternatively, magmatic overpressure can lift the chamber roof, causing shallow crustal deformation in the form of downward-propagating faults. If these structures reach the reservoir and result in eruption and caldera collapse, the process is considered externally triggered (Gottsmann et al., 2009; Gregg et al., 2012; Gudmundsson, 2008). Lastly, there are cases where these eruptions can be tectonically triggered when the magmatic system occurs in an area undergoing regional deformation (Allan et al., 2012). Intensive variables such as magma storage depth, water content and temperature are therefore directly related to the factors that control the beginning and the ongoing development of a caldera-forming eruption. Although some caldera-forming eruptions are associated with very shallow reservoirs (<5 km) (e.g. Larsen, 2006; Coombs and Gardner, 2001), the reservoirs at several caldera complexes are located at relatively deeper crustal levels (e.g., Chesner, 1998; Johnson and Rutherford, 1989; Pamukçu et al., 2020).

In order to characterize the volcanic system, petrologic constraints from old eruptions may provide important insight for future volcanic unrest. The Maipo volcano complex in Central

Chile is of particular interest, as it has produced a voluminous caldera-forming eruption in close proximity to now densely populated areas. This center produced the Pudahuel Ignimbrite, which is exposed throughout Santiago de Chile. A first step in understanding the dynamic aspects of this eruption is to determine the storage conditions of the magma prior to eruption (Andrews, 2014; Befus and Gardner, 2016; Hammer et al., 2002). The composition (including dissolved H_2O content) and intensive variables (e.g., temperature and pressure) play important roles in the eruption process and, in combination with conduit geometry and transport dynamics, control eruption style and intensity (Wilson et al, 1980; Sparks, 1986; Blundy and Cashman, 2008). Temperature, composition and crystallinity control magma viscosity and therefore magma mobility, gas exsolution and outgassing during ascent, and eruption explosivity (Dingwell, 1998; Giordano et al., 2008; Papale, 1999; Pinkerton et al., 2002; Rutherford, 2008). Storage pressure constrains the depth of the reservoir, and along with other parameters such rock strength and reservoir shape, influences the sequence culminating in a caldera-forming eruption (Jellinek and DePaolo, 2003; Marti et al., 1994). Moreover, along with temperature and composition, pressure controls the concentrations of volatile constituents that can be dissolved in the magma (Liu et al., 2005; Moore et al., 1998; Zhang et al., 2007), which in turn influence the magma's potential explosivity (Jaupart and Allègre, 1991; Wilson et al., 1980). Determining these parameters for as many individual systems as possible is a path forward for understanding the physical and chemical attributes and processes that culminate in catastrophic caldera collapse events. The Pudahuel Ignimbrite is the result of a large quaternary caldera-forming eruption and is part of an active volcanic complex. Constraints on the underlying magmatic system are needed to characterize the caldera-forming event that occurred >100 ka and to assess the risk still posed by the Maipo volcano complex today.

The magma storage conditions preceding the caldera-forming eruption that generated the Pudahuel Ignimbrite have not been defined previously. It is possible to estimate the storage conditions, including temperature, pressure, H_2O concentration, and oxygen fugacity (fO_2) using the abundances, textures, and compositions of magmatic phases (e.g. Barclay et al., 1998; Castro et al., 2013; Coombs and Gardner, 2002; Lindsay et al., 2001b; Ruprecht et al., 2012; Rutherford et al., 1985). A complementary approach to resolving these parameters, generally to a greater precision, is the reproduction of the natural phase assemblage and

mineral rim compositions in laboratory phase equilibrium experiments (e.g. Castro et al., 2013; Hammer and Rutherford, 2002; Rutherford et al., 1985). In the hybrid approach taken here, mineralogical geothermometers and geobarometers are applied to phases in the Pudahuel Ignimbrite pumice. This allows us to provide an initial matrix of possible environmental conditions that is then explored experimentally to tighten constraints on the pre-eruptive magmatic conditions.

Here we present new petrological and geochemical characterization of pumice from fall deposits and pyroclastic density current (PDC) deposits collected in the Maipo, Cachapoal (Chile) and Yaucha valleys (Argentina), and bracket the magma storage conditions. The subsequent experiments are designed to (a) test the efficacy of mineral-based thermometry and hygrometry as applied to this rhyolite; (b) further refine, if possible, the P_{H2O}-temperature combinations that produce the phase assemblage, mode and compositions of the natural pumice; and (c) evaluate the possibility that the silicate liquid was undersaturated with respect to H_2O (i.e., contained dissolved H_2O content lower than the solubility concentration) in the storage area, and if so, to determine the total pressure (P_{Total}).

2. Geologic Setting

The Maipo volcano complex is located in central Chile in the Andean Cordillera, on the border between Chile and Argentina (34º09'S, 69º49'W), in the northern part of the Southern Volcanic Zone (Fig. 1). It lies ~100 km upstream on the Maipo river from Santiago de Chile, and with >2500 m of relief along the Maipo river, it poses a significant risk for well over 6 million people. The complex includes the Diamante caldera and the Maipo volcano (Stern et al., 2007). The Diamante caldera in the Maipo volcano complex was produced by a VEI 7 eruption that resulted in the emplacement of a voluminous ignimbrite known as the Asociación Piroclástica Pumícea (Guerstein, 1993; Polanski, 1963). The deposit has been variably termed the Pudahuel Ignimbrite in Chile and the Diamante Tuff in Argentina (e.g., Wall et al., 1996 and Harrington, 1989 respectively). Volume estimates have varied over the years, but the current best estimates from mapping and stratigraphy suggest a total volume of 270 km^3 (135 km^3 DRE), distributed as 20 km^3 for two plinian fall deposits and 250 km^3 for the PDC deposits (Guerstein, 1993; Troncoso, 2012). This volume is considerably higher than that recently erupted by other volcanic centers in the SVZ (Hildreth and Moorbath, 1988). For example, the Quizapu 1932 eruption, which is the largest historic explosive

eruption in the Andean Cordillera, has an estimated volume of 4 km^3 (DRE) (Hildreth and Drake, 1992). However, the nearby Laguna del Maule volcanic field has generated 350 km^3 of mainly rhyolitic volcanism over the past 1.5 million years and is currently in a state of unrest (Hildreth et al., 2010; Singer et al., 2018) making our study of the Pudahuel Ignimbrite all the more timely.

The Pudahuel Ignimbrite is composed of discrete dominantly matrix-supported PDC deposits that occupy the valleys of the Maipo and Cachapoal rivers in Chile and the valleys of the Yaucha, the Rosario and the Papagayos rivers in Argentina (Fig. 1). Deposit characteristics vary between the valleys. The most notable differences are (1) elutriation pipes in the Maipo valley and in distal portions of the Yaucha and Papagayos valleys, (2) variation in pumice size and the size and type of lithics, and (3) the degree of welding, from non-welded to moderately welded in some areas of the Maipo and Rosario valleys (Fig. 1) (Guerstein, 1993; Troncoso, 2012). With respect to the lithics, Troncoso (2012) identified plutonic and volcanic lithics in both Chilean valleys, whereas in distal facies from the Maipo valley, she also identified volcaniclastic lithics, limestone, and obsidian (west area of the city of Santiago in Figure 1). PDC deposits in the Papagayos and Yaucha valleys contain sedimentary lithics and obsidian, in addition to volcanic and intrusive lithics. Proximal deposits only contain volcanic lithics (Guerstein, 1993). In all valleys the larger clasts consist, in order of decreasing volumetric abundance, of highly vesicular (60-90%) pumices (up to 18 cm) and lithics of basement rock (Guerstein, 19993; Hynek et al., 2010; Troncoso, 2012). Pumices with color variation, between pink, light gray and white and gray banded, have been described by Burkert et al., (2010).

The paucity of accessible and coherent outcrops and their distribution across an international border have stymied efforts to develop a consensus view of the key physical aspects of the eruption. For example, Guerstein (1993) suggests that PDCs flowed simultaneously down several valleys, whereas Troncoso (2012) interprets a sharp vertical variation in the abundance of obsidian lithics in the upper part of the Maipo valley deposit as evidence against simultaneous flow emplacement. Working within the outcrops on the Argentinian side of the caldera complex, Guerstein (1993) describes a pumice-rich fall deposit beneath the PDC (Fig. 2c–e), which he interprets as an initial plinian phase of the eruption. The presence of an oxidized contact between an ash-rich band and a pumice-rich layer within this fall sequence

suggests short time breaks and/or unsteadiness in the eruption column, supporting Guerstein's (1993) inference that the fall deposit is comprised of two packages. The putative initial fallout deposit is not exposed elsewhere and is not treated further in this study.

The whole rock (pumice as well as ash matrix) composition of the Pudahuel Ignimbrite is consistently rhyolitic (~74 wt.% SiO_2) as assessed by analyses of the PDC outcrops in different valleys (Guerstein, 1993; Hynek et al., 2010; Sruoga et al., 2005; Stern et al., 1984). Trace element analyses of PDC pumices show high values of Rb and Ba (103-156 ppm and 715-769 ppm respectively) and low values of Sr and Zr (62-86 ppm and 57-89 ppm, respectively), and a marked negative Eu anomaly (Stern et al., 1984). This, along with their isotopic composition, which is characterized by high $^{87}Sr/^{86}Sr$ and low $^{143}Nd/^{144}Nd$ average values (0.70594 and 0.51255 respectively), suggests a strong crustal component combined with extensive crystal fractionation (Futa and Stern, 1988; Stern et al., 1984). Subtle variations in Fe_2O_3(0.41-0.67%), Cl (0.068-0.117%) and CaO (0.44-0.53%) concentrations within individual pumice clasts and glass shards have been reported in a single stratigraphic section exposed between the Papagayos and Yaucha valleys (Fig. 1) (Hynek et al., 2010).

Although the rhyolite pumice and ash composing the PDCs is dominantly glass, the low cognate crystal content (~6 wt.%) includes a large number of mineral phases: plagioclase, biotite, titanomagnetite, apatite and zircon (Guerstein, 1993; Stern et al., 1984). Specifically, biotite and zircon have been used to constrain the eruption age. However, current age estimates for the caldera-forming eruption vary significantly. Stern et al., (1984) date the eruption with the fission track method in zircons at 0.45±0.06 Ma. $^{40}Ar/^{39}Ar$ dating of biotite (Wall et al., 2001) yields an older age of ~2.3±0.3 Ma. More recent (U-Th)/He age dating of zircons (Lara et al., 2008) yields a much younger age of ~0.15 Ma, which is consistent with U-Pb dating of zircons yielding 0.13 Ma (Pineda, 2015).

3. Methods

3.1. Sample collection

Pumice samples from PDC deposits were collected from twenty-one locations along valleys that drain the Maipo volcano: The Maipo and the Cachapoal valleys near the Chilean cities of Santiago and Rancagua, respectively, and the Yaucha valley in Mendoza province in Argentina (Fig. 1). Although we did not perform a detailed stratigraphic analysis of the

deposits in any locality, our observations are consistent with previous descriptions of the PDC deposits (Guerstein, 1993; Stern et al., 1984; Troncoso, 2012). In general, the PDC deposits are massive (Fig. 2a–b), with an ashy matrix containing pumices of variable sizes, crystals (mainly plagioclase and biotite), and variable abundance of lithics. Samples were collected at the outcrops that were suitably coarse-grained and pumice rich from Maipo, Cachapoal and Yaucha valleys (marked in Fig. 1 with purple, green and yellow circles respectively). Color variations (from pale white ash to reddish ash) were observed in several of the thicker deposits (Fig. 2a–b); in these cases, samples of each level were collected. In the cases where pumices were not big enough, bulk samples were collected. In each case, care was taken to select unoxidized and unaltered material.

We collected an additional three samples of the plinian fall deposits preserved on the Argentinian side, described by Guerstein (1993). The first one is a pumice lapilli fallout bed overlain by an ash layer, and the second is also a pumice lapilli fallout bed with normal and reverse grading. The plinian fall in this area is overlain by the PDC deposits, with an erosional boundary in between, interpreted to have been created by the density current (Guerstein, 1993).

Our sampling strategy is predicated on prior work that demonstrated first-order compositional uniformity. We collected material specifically to facilitate the exploration of magmatic pre-eruptive intensive conditions through mineral thermobarometry and reconnaissance-style phase equilibrium experimentation. Additional field work, sampling, and textural assessment would be needed to constrain the eruption sequence, including evaluating the conduit and column dynamics that produced widespread ignimbrite deposition and fallout dispersal (Carey and Sigurdsson, 1989).

3.2. Analytical methods

Thin sections of a representative pumice clast for each location were made and then characterized petrographically using a polarizing light microscope and scanning electron microscope (SEM, FEI Quanta 250) at the Andean Geothermal Center of Excellence (CEGA) in the Department of Geology at the Universidad de Chile. Analytical conditions for the SEM were 15 kV accelerating voltage and a spot size of 5 microns; back-scattered electron imaging and semi-quantitative energy-dispersive spectroscopy (EDS) analyses were performed with software INCA (Inca x-act, Oxford Instruments).

Fifteen samples from proximal locations that appear fresh on all scales (marked with filled dots in Fig. 1) were selected for whole rock analysis, and two of them were rejected because of anomalously high values of LOI (>5 wt.%). Analyses were performed at Actlabs Ltda. by ICP (major elements) and ICP-MS (trace elements).

One sample (CPIP13), representative of the texture, mineralogy and composition of the ignimbrite, was selected for mineralogical quantitative analysis and served as the starting material for phase equilibrium experiments. Fe-Ti oxide grains were separated from the pumice with a hand magnet, mounted, sectioned, and polished for petrographic and electron microprobe (EMP) analysis. Other phases were analyzed from polished sections of pumice clasts. Quantitative analysis of Fe-Ti oxides, plagioclase, and glass was conducted on the JEOL JXA-8500F electron microprobe at University of Hawai'i at Manoa (UHM). Fe-Ti oxides were analyzed using a 20 keV accelerating voltage, a beam current of 20 nA, and a beam diameter of 5-10 μm. Glass and plagioclase analyses were conducted using an accelerating voltage of 15 keV, beam current of 10 nA, and beam diameters of 10 μm and 5-10 μm, respectively. All electron microprobe data, including analyses of standards that we used to monitor drift and assess analysis reproducibility are in Appendix A.

3.3. Experimental strategy

We apply established mineral thermobarometers to newly acquired compositional analyses to estimate the temperature, oxygen fugacity (fO_2) and P_{H2O}; i.e., the pressure assuming magma saturation with H_2O-rich fluid (c.f. Rutherford and Hill, 1993). These estimates guide our application of the 'phase match' experimental method for constraining magmatic environments prior to eruption (*e.g.* Rutherford et al., 1985; Hammer and Rutherford, 2002; Castro et al., 2013). First, we apply Fe-Ti oxide thermometry (Ghiorso and Evans, 2008) to natural titanomagnetite and ilmenite crystals to obtain the temperature and oxygen fugacity combinations at which the oxides last equilibrated via coupled exchange mediated by the liquid phase. Second, we apply the plagioclase-liquid hygrometer (Waters and Lange, 2015) to the compositions of feldspar crystal rims and the matrix glass to solve for the concentration of dissolved H_2O at the Fe-Ti oxide equilibration temperature. We also apply the hygrometer to temperatures up to 850 ºC, well above the value represented by Fe-Ti oxide equilibration, in order to define a larger range of plausible H_2O contents representing equilibrium between the natural glass and feldspar and, in this way, consider the possibility that Fe-Ti oxide

temperature is a minimum. Finally, the composition-dependent H_2O solubility model (Zhang et al., 2007) is applied in reverse to solve for P_{H2O} at the specified temperature.

The success in matching natural crystallization conditions is evaluated by comparing experimental run products with the natural pumice starting material. If the run conditions are dissimilar from the pre-eruptive magmatic environment, then the run product phase compositions and abundances differ substantially from those of the starting material and bear textural evidence of chemical reaction in the form of new phases and/or corroded or thickly rimmed relict mineral grains. Conversely, if an experiment is performed at the conditions corresponding to equilibration conditions in the magma reservoir, then the run products are identical to the pumice starting material in terms of the phase compositions (on an anhydrous basis), phase assemblage, and mode (Pichavant et al., 2007; Rutherford et al., 1985).

3.4. Experimental methods

Pumice clasts from CPIP13 were brushed and rinsed with tap water and subsequently ultrasonicated in deionized water for 30 minutes to remove adhering ash particles. Then they were dried at ~100 ºC for 10 hours and crushed very gently. Minimal crushing serves two functions. First, it sequesters crystal interiors, preserving to the extent possible the thermodynamically appropriate 'reactive magma' (c.f. Pichavant et al., 2007) as the interstitial liquid and crystal rims. This minimizes the undue influence of compositional zoning in the natural phenocrysts. Second, it provides a textural advantage for post-run analysis. Whereas microlites are difficult to analyze because of their small size and high aspect ratio, rim growth on pre-existing (relict) grains is typically larger in area and extends deeper into the section. These practical and energetic considerations, combined with the desire to maximize the mass of each run product, led us to adopt the method of loading capsules with ~3 mm diameter pumice particles (Brugger and Hammer, 2010; Hammer and Rutherford, 2002; Coombs et al., 2000; Cottrell et al., 1999).

Twelve isothermal-isobaric experiments were performed at H_2O-vapor saturated conditions (i.e., $P_{H2O} = P_{TOT}$) in cold-seal pressure vessels in the Experimental Petrology Laboratory at UHM. Between 0.07 and 0.16 g of pumice fragments were loaded into Ag and $Ag_{70}Pd_{30}$ capsules along with distilled, deionized water, sufficient to ensure saturation with H_2O-rich fluid at the run conditions with minimal overage (c.f. Rutherford and Hill, 1993). Capsule fidelity was verified before each experiment by checking for mass change after 10 minutes

immersion in acetone and then again after 4-8 h in a warm oven; after the run, capsule integrity was confirmed by an audible hiss upon piercing. All the run products included in tables and figures passed these tests. In order to evaluate (in reconnaissance fashion) the effect of pressure independently from dissolved H_2O content, a set of three experiments was performed at the same P_{Total} but different (lower) P_{H2O}. These charges were prepared using chips of previously run material, sealed without additional H_2O, inside new capsules and run at a higher pressure than in the preceding experiment. These experiments are 'vapor-absent'; the amount of dissolved H_2O is less than that required for H_2O-rich fluid saturation (hereafter 'H_2O-saturation'), i.e., $P_{H2O}<P_{Total}$ and no additional volatile constituents (such as CO_2) were added.

Run temperature and pressure set points were normally achieved within 30 minutes of placing a vessel in the furnace. Run pressure was checked 1-2 times per day against a factory calibrated Heise bourdon tube gauge. Pressure was maintained throughout the 162-356 h (average 282 h) dwell times within 6 MPa of the setpoint value. Experiments were quenched while maintaining pressure within ±10 MPa of the set point, by means of a manually operated pressure intensifier.

Two ambient fO_2 environments, corresponding to the Ni-NiO (NNO) buffer and two log units below it (NNO-2, as described in First et al., 2021), were applied to separate charges at four of the in-band temperatures-pressure nodes. Subsequent experiments (numbered above 7) were performed at NNO.

3.5. Selection of run conditions: in-band vs. out-of-band

As described above, the selection of experimental conditions was guided by the application of Fe-Ti oxide thermometry (Ghiorso and Evans, 2008), plagioclase-glass hygrometry (Waters and Lange 2015), and a water solubility model (Zhang et al., 2007) to establish the best estimate of temperature and pressure (at $X_{H2O}^{fl} = 1$) conditions that would produce the least chemical change in the starting material, and thus indicate a match to the natural magmatic environment. Also, experiments were performed at other P-T-X_{H2O} combinations, as independent tests of the thermobarometers (c.f. Gardner et al., 2014). Experimental run conditions are shown in pressure-temperature space in Figure 3. The group of experiments performed at conditions satisfying the plagioclase-liquid hygrometry model are referred to as "in-band" experiments. The out-of-band experiments, at P-T conditions both above and

below the band, were run to verify the plagioclase-liquid hygrometry model calculations. The out-of-band experiments facilitate evaluation of the sensitivity of the system to environmental conditions proximal to thermometer-hygrometer temperature-pressure combinations. Because the band is roughly parallel to crystallinity isopleths for this composition (as informed by prior studies of evolved magmas: Coombs and Gardner, 2001; Gardner et al., 1995; Hammer et al., 2002; Rutherford et al., 1985) the out-of-band runs provide a test of the null hypothesis, "the rhyolite starting material is unchanged by exposure to run conditions". That is, if the stable phase assemblage at each of the in-band experiment nodes buffers the liquid with respect to major element variation, then the glass compositions of these charges would be unchanged (accounting for H_2O) after exposure to magmatic temperature and pressure. We would be unable to reject the null hypothesis. As the out-of-band experiments were run outside the pressure-temperature space where the plagioclase-liquid hygrometer is satisfied, they should manifest marked compositional changes, especially in the glass.

Run products recovered from the capsules were mounted in epoxy, sectioned, polished, and analyzed by EMP at UHM using the same methods as applied to natural samples (described above).

3.6. Approach to Equilibrium

Melt viscosity, element diffusivity, and time, control the attainment of chemical equilibrium in an experiment. At our experimental conditions, melt viscosities are high (~10^5 Pa·s) (after Giordano et al., 2008; see Appendix B) and element diffusivities (D) range from 4 to 0.06 $\mu m^2/s$ for K and Si respectively at the higher run temperatures (after Jambon, 1982 and Baker, 1992, respectively; see Appendix B). Using the approximation D~ $length^2$/time, these rates translate into melt diffusion distances of ~1860 μm for K and ~240 μm for Si over our run durations (>10 days in all cases except one). Similarly long experimental durations are common in phase equilibria experiments of rhyolite melts, although they do reduce the total number of experiments that can be performed (e.g., Befus and Gardner, 2016; Gardner et al., 1995; Martel, 2012). Further mitigation of low component mobility comes from the use of lightly crushed natural starting material, which contains substrates on which growth may begin at low undercooling (Hammer 2008). Finally, intracrystalline distances between

microlites in our experiments are small relative to diffusion distances, enabling the liquid to approach equilibrium,

The changed glass compositions in the out-of-band run products (reported below) demonstrate that mass transfer between phases occurs in the experimental run times: net dissolution and crystallization occurred in experiments 07 (above band) and 17 (below band), respectively. This demonstration is not, in itself, proof that the run times are sufficient for chemical equilibrium between liquid and crystal rims. In fact, the heterogeneity of the glass compositions within many individual charges indicates failure to equilibrate. We mitigate this problem by evaluating element co-variation trends and developing a normative basis for comparison.

The multiply-saturated aphyric rhyolite poses challenges as well as some advantages in application of the phase-match method (Barclay et al., 1998; Befus et al., 2014; Larsen, 2006). The presence of five mineral phases in the natural sample is a tremendous asset: the magma had to equilibrate in a region of P-T space in which plagioclase (An_{20-17}), biotite, magnetite and ilmenite are stable, and sanidine and quartz are absent. However, the low crystallinity also presents challenges. Many crystals are small and not typically encountered at center-cutting orientations in thin section, rendering their identification (and analysis) in experimental charges difficult or impossible. On the other hand, high melt fraction is also an advantage because it leverages the greater diffusivities of molecular components in the liquid (as opposed to solid) state and thus promotes global chemical communication among all phases (Waters and Lange, 2015). Further, large pools of glass, unlike interstitial pockets, can be analyzed using a defocused electron beam, minimizing the loss of alkalis (Devine et al., 1995).

4. Results

4.1. Petrography, whole rock geochemistry and mineral chemistry

Pumices have porphyritic and cumulophyric textures with plagioclase and biotite phenocrysts, and oxide microphenocrysts in a glassy groundmass (Fig. 4a). Some mineral grains are fragmental, suggesting syn-eruptive or depositional breakage. All PDC samples examined under petrographic microscopy possess the same mineralogy and textures. Four of them (one of each valley where samples were recollected and one additional from the location

where the experimental sample was picked), were selected for a meticulous standard point counting (3000-5000 points per slide) in BSE and polarizing light microscopy images. The identified phases during this process are: glass (96.8% ±1σ =0.3), plagioclase (1.8% ±1σ =0.3), biotite (0.4% ±1σ =0.1), magnetite (>1%), ilmenite (tr), zircon (tr), monazite (tr), and apatite (tr). The crystals are euhedral-subhedral, equant, and except for the optically-distinguishable zonation in large plagioclase phenocrysts, appear to be in chemical equilibrium with the surrounding rhyolite glass (Fig. 4). One sample contains a trace amount of porous (i.e., corroded) iron sulfide grains. Crystals of all major phases are phenocrystic or microphenocrystic; microlites (crystals ≤30 μm) do not exist in the pumice. Accessory phases occur in the groundmass or as inclusions in plagioclase and biotite.

The ignimbrite samples are rhyolite (74.5-76.6 wt.% SiO_2, Table 1; Fig. 5) and show very limited variation between the fallout and PDC samples, other than the fallout samples being slightly enriched in Sr. The glass composition is very close to the whole rock composition (76.6 wt. %, Table 1 and Table A. 4). Plagioclase crystals can be separated into two compositionally distinct groups. Group 1 consists of unzoned phenocrysts with compositions of An_{20-17}, and group 2 consists of phenocrysts with normal zoning from An_{48-40} in the core and An_{20-17} in the rim (Fig. 4c; Table A.1).

4.2. Temperature, fO_2 and P_{H2O} constraints from natural samples

Application of the Fe-Ti oxide thermometer (Ghiorso and Evans, 2008) requires a minimum of one pair of crystals, representing titanomagnetite ("magnetite") and hemoilmenite ("ilmenite") solid solutions, respectively. Ideally the crystals are contiguous or at least closely spaced and separated by glass. A thermometry result is considered robust if it includes many unique pairs, and further strengthened by confirmation of inter- and intra-grain chemical homogeneity. A search of hundreds of grains mounted and sectioned from the magnetic fraction of the CPIP13 crystal separate revealed just two magnetite-ilmenite pairs in contact and several isolated ilmenite and magnetite crystals surrounded by glass. The compositions of extant crystals of both phases are uniform (Table A.6). The analyses were paired each with the other to yield 80 combinations passing the Mn-Mg equilibrium test of Bacon and Hirschmann (1988), from which temperature and oxygen fugacity fO_2 were calculated (Fig. 6 and Appendix C). The average temperature obtained with the geothermometer is 717 ± 7 ºC and the average oxygen fugacity is 1.35 log units above the

nickel-nickel oxide (NNO) buffer (±1σ = 0.03 ΔNNO). The accuracy of the Fe-Ti oxide thermometer has been assessed independently (Blundy and Cashman, 2008) as ± 44 ºC. Given the paucity of unique pairs, we take the range of 673-761 ºC as a conservative estimate of the Fe-Ti oxide exchange equilibrium temperature represented by the Pudahuel crystals.

The average Fe-Ti oxide temperature (717 ºC) was used as an input to the plagioclase hygrometer (Waters and Lange, 2015), along with the measured glass composition (Table 2, A.4) and the most evolved plagioclase composition (Table A.1), to calculate the amount of H_2O dissolved in the liquid. Incorporating uncertainties, we calculate 7.3±0.4 wt.%, which corresponds to an H_2O-saturation pressure range of 200-360 MPa according to the solubility model of Zhang et al., (2007) applied to the CPIP13 pumice composition (Fig. 7a). This procedure was repeated for higher temperatures (Fig. 7b) to generate the band of P_{H2O}-T conditions that satisfy the plagioclase hygrometer and the solubility model. This band guides the selection of experimental run conditions shown in Figure 3.

A subset of the in-band runs falls within the temperature produced by Fe-Ti oxide thermometry. The runs in this overlapping section of pressure-temperature space were anticipated to produce run products most closely matching the phase assemblage, compositions, modes, etc. of the natural pumice. Experiments were focused within this region in an attempt to confirm and possibly refine storage pressure within this range of values (200-360 MPa). Several H_2O-undersaturated experiments ($P_{H2O}<P_{Total}$) were performed to explore the effect of total pressure on the phase assemblage and liquid composition, etc., separately from dissolved H_2O content (and thus P_{H2O}).

4.3. Experimental results

Plagioclase is generally present in the experiments, except for the experiment run above the band performed at 310 MPa and 750 ºC (Table 3, Fig. 8), which is devoid of plagioclase rim growth and microlites. Plagioclase crystals present in run products usually exhibit faceting, unmodified fracture surfaces, growth rims, and/or growth protuberances (Fig. 9 a-c). These features are consistent with mineral phase saturation or supersaturation at the run conditions. In some cases, parts of the crystals contain textural evidence of both undersaturation (dissolution), such as rounded corners and internal sieve-texturing, and saturation (growth), such as sharp apices and flat faces of rims with markedly different composition from the interior (Fig. 9a). Biotite is present in experiments run at and below 800 ºC (Table 3, Fig. 8).

It appears as isolated crystals in the groundmass usually as euhedral crystals; it also appears surrounding Fe-Ti oxides (Fig. 9f). The presence of high-Ca pyroxene varies according to the fO_2 at which runs were performed. At the higher fO_2 (NNO), high-Ca pyroxene appears only in the experiment performed at 130 MPa and 800 ºC, whereas for experiments performed at the lower fO_2 (NNO-2), it is only present in the experiment performed at 200 MPa and 750 ºC. Low-Ca pyroxene is present in all experiments above 800 ºC. Both types of pyroxene occur as euhedral crystals in the groundmass, sometimes isolated and sometimes as clusters with plagioclase (e.g., at 800 ºC; Fig. 9d). In some cases, low-Ca pyroxene is associated with rounded Fe-Ti oxides and plagioclase (Fig. 9e). Quartz is present in NNO-2 experiments below 750 ºC; crystals are anhedral and with rounded edges. Quartz is not identified in the NNO experiments, but its overall scarcity (just one crystal in each of the NNO-2 charges) permits the possibility that it is present but undetected in the observed section. Fe-Ti oxides are observed in most of the experimental run products, exceptions being several NNO experiments.

The compositions of experimental matrix glasses all fall within a relatively narrow range within the rhyolite spectrum (See Table 2, Fig. 10 and Appendix D). All elements (expressed in metal oxide weight percent) except K_2O are positively correlated with MgO and anticorrelated with SiO_2. The maximum SiO_2 and K_2O occur in the below-band experiment 17 (700 ºC, $P_{Total}=P_{H2O}$=200 MPa, 6.2 wt.% H_2O, NNO), consistent with these run conditions producing the greatest amount of crystallization. The maximum MgO, Al_2O_3, FeO_T, Na_2O, CaO and P_2O_5 occur in above-band experiment 7 (850 ºC, $P_{Total}=P_{H2O}$=200 MPa, 5.8 wt.% H_2O, NNO-2), consistent with dissolution of crystals that were present in the starting material. The matrix glasses of the in-band experiments span the compositional space between these extremes.

Plagioclase is the most abundant mineral phase in the natural sample and is the only mineral phase in the run products forming crystals large enough for EMP analysis (Fig. 11, Table A.2). In the natural samples, we report analyses of rims of compositionally unzoned crystals as well as rims of zoned crystals; in experimental run products, we report analyses of faceted crystal cores, and rims in contact with glass (Tables A.1 and A.2). The plagioclase compositions of experiment 04 and undersaturated experiments 13 and 15 are similar to the plagioclase in equilibrium with natural glass (Fig. 11). Experiments performed at

temperatures higher than 717 ºC yielded plagioclase with more anorthitic compositions (An_{30-50}). They typically occur as reversely zoned crystals, characterized by a bright growth rim and a relict dark core of less calcic composition (An_{20}, e.g., Fig. 9b).

5. Discussion

The new whole rock data reinforce findings from earlier work and indicate our samples are representative of the deposit as a whole (Fig. 5). Both major and trace elements are uniform among the samples and similar to previously reported analytical results (Futa and Stern, 1988; Guerstein, 1993; Hynek et al., 2010; Sruoga et al., 2005b; Stern et al., 1984). Thus, in the following sections, we integrate the analyses of natural minerals and glass with new data from isobaric-isothermal experiments to infer the most likely pre-eruption storage temperature, depth, and H_2O contents. These constraints are then discussed within the regional geologic context, including structure and spatio-temporal patterns of volcanism.

5.1. Pre-eruptive conditions: constraints from mineral indicators

The low crystallinity, relatively unzoned crystals, and the apparent geochemical similarity among all whole rock samples across the deposit types and locations make the Pudahuel rhyolite well suited to the application of mineral-melt oxythermometry and hygrometry for the estimation of pre-eruptive storage conditions. The titanomagnetite and ilmenite crystals are homogeneous micro-phenocrysts, and although Fe-Ti exchange equilibrium is restored relatively quickly in response to changes in temperature and/or fO_2 (Hammond and Taylor, 1982; Venezky and Rutherford, 1999), we interpret them to have formed prior to the eruption. All pairings of analyzed magnetite and ilmenite grains pass the Mg-Mn equilibrium test (Bacon and Hirschmann, 1988) and yield a restricted range of T-fO_2 values (717 ± 7 ºC, 1.35 ± 0.03 ΔNNO), further supporting their formation prior to eruption. At this temperature the compositions of coexisting feldspar and glass indicate that the rhyolite is capable of dissolving high H_2O contents (~6.9-7.6 wt.% H_2O) if stored at P_{H2O} ~200-360 MPa.

5.2. Pre-eruptive conditions: constraints from experiments

Starting with the constraints on temperature, P_{H2O}, and fO_2, outlined above, the experiments sought the particular combination of conditions that produces a match between the synthetic and natural mineral phases, abundances and compositions. As is commonly observed in experiments, feldspar occurs as rims on inherited crystals and as newly-grown microlites

(e.g., Gardner et al., 1995; Hammer and Rutherford, 2002; Martel, 2012). Textural and compositional indications of new growth, such as faceting and zoning, were taken into account while filtering compositional data. Nevertheless, the range of rim compositions was significant in some charges (Fig. 11). Furthermore, because all of the biotite crystals are too small to analyze (biotite and feldspar being the volumetrically dominant phases), we were unable to apply the method of mass balance to determine the abundance of minerals in the experimental run products. As a result of these challenges, the assessment of pre-eruption conditions hinges on variations in matrix glass compositions of the experimental run products. It was not possible to apply the mineral-composition match method, so the revised strategy is that of glass-match. Admittedly, even the glass-match approach was problematic to apply because (a) multi-saturation and intrinsic near-minimum nature of the liquid buffered the liquid against change, and (b) the relatively low component mobilities prevented full diffusive homogenization of the liquid on the experiment time scale.

Fortunately, the glass is the single most sensitive indicator of intensive conditions, because it responds to all the other properties of the system: the mineral assemblage, mode and mineral compositions (c.f. glass-match approach used in other studies involving high-silica compositions: First et al., 2021; Gardner et al., 1995; Hammer and Rutherford, 2002). A strong positive correlation between FeO_T and MgO (Fig. 10a) indicates compatible behavior of these elements in the crystallizing assemblage. MgO is deemed the best indicator of liquid evolution along the path of differentiation by crystallization because of this consistent compatibility in the fractionating assemblage. A monotonic decrease in SiO_2 with respect to MgO (Fig. 10b) indicates that the incipient formation of quartz (observed in experiments run below 750 ºC at fO_2 NNO-2), has had little or no effect on the liquid. However, there is a slight variation among experiments in the rate at which SiO_2 increases per-unit and MgO decrease, at least in the range where MgO is still declining (from 0.15 to 0.08 wt.%). Along with Al_2O_3 (Fig. 10c) and K_2O (Fig. 10d), the fanning-out of these element concentrations indicates that the proportions of minerals being fractionated varied in response to different environmental conditions. Given that K-feldspar is not observed in any experiment and K_2O contents of the experimental plagioclase (0.18-1.18 wt.%) are similar to that of the starting material (0.19-1.04 wt.%), the only mineral capable of decreasing K_2O in the liquid by its formation is biotite. Indeed, biotite crystals in the natural sample (large enough to be

analyzed) have up to 8.6 wt.% K_2O (Appendix E). Recalling that the diagonally sloping band of experimental run conditions was designed to satisfy a given combination of plagioclase and glass compositions, it is unsurprising that the abundance of plagioclase is relatively constant in the experiments. In contrast, the amount of biotite and thus the biotite/plagioclase ratio in the crystallizing assemblage increases with pressure, as shown by the inverse correlation between pressure and glass K_2O among the experiments at 700 ºC (Fig. 10c and Appendix D). Although the small grain size in the experimental charges prevents analysis of crystalline phases except feldspar, the increase in the biotite/plagioclase ratio in the crystallizing assemblage with increasing pressure is consistent with the compositions of these natural minerals and the synthetic glasses. Moreover, an increasing prominence of biotite with increasing P_{H2O} over the examined range is consistent with a general understanding of phase equilibria in hydrous high-silica systems (e.g. Blatter et al., 2017; First et al., 2021; Rutherford and Devine, 2003).

Notably, the glass compositions of the three H_2O-undersaturated experiments (13,14 and 15) are very weakly dependent on the H_2O saturation state (Appendix D); they largely overlap with the composition of the H_2O-saturated run performed at the same P_{Total} (350 MPa, experiment 16), rather than the runs at the same P_{H2O} (10, 11 and 12 respectively). The dissolved H_2O contents of these experiments were evidently sufficient to stabilize biotite and thus promote biotite control over the liquid composition.

The MgO variation diagrams, particularly those in which element concentrations vary systematically as a consequence of pressure over a small range in MgO (Fig. 10) guide the application of a glass-match method for refining the magma equilibration conditions from among the in-band experimental run products. The concentration of K_2O is the least correlated with MgO, and yet K_2O is sensitive to the proportion of biotite in the crystallizing assemblage.

None of the analyses of the natural glass contain more than 0.12 wt.% MgO. Together with concentrations of and trends with other elements (Fig. 10 and Appendix D), it is concluded that the experiments that produced the higher MgO glasses are unsuitable as matches. This includes the out-of-band experiment 17 as well as in-band experiments above 750 ºC. The nature of compositional shifts indicates that these experiment conditions caused net dissolution of crystals. Below 0.15 wt.% MgO, the concentrations of other elements (Al_2O_3

and K_2O, Figs. 10c and 10d, respectively) spread out, as discussed above, as a consequence of the varying proportion of biotite. With respect to MgO-Al_2O_3, the cloud of natural glass analyses overlaps the glasses of experiments 3 and 10 and out-of-band experiment 17, all performed at 200 MPa and 700-750 ºC. With respect to MgO-K_2O, the natural glasses overlap strongly with the glasses at 700 ºC at P_{Total} of 350 MPa (experiments 13, 14, 15 and 16), and overlap moderately with experiments at P_{Total} of 280-300 MPa (4 and 12) There is no overlap in the K_2O contents of the natural glass and the glass of experiments performed at $P_{Total} \leq$ 200 MPa.

A glass composition barometer was developed from the in-band experiments and applied to the Pudahuel glass, as follows. First, we note that the SiO_2-K_2O systematics within each charge comprise a negatively sloping array (Fig. 12). The SiO_2-K_2O correlation is interpreted to reflect spatial variation within the charge in the progress toward equilibrium crystallinity, rather than random scatter. (A complete graphical presentation of oxide abundances is presented in the Appendix D). Having established the dependence of glass composition on P_{Total} through the influence of biotite, we sought to account for the effect variable intra-charge biotite crystallinity. We fit the K_2O-SiO_2 glass data from each run product with a line and find (generally by interpolation rather than an extrapolation) the K_2O content corresponding to SiO_2 concentration of 76.6 wt.% (the average SiO_2 content of the natural glass; Fig. 12a). The resulting value, $[K_2O]_{76.6}$, is plotted in Figure 12b against pressure. The shift in $[K_2O]_{76.6}$ is subtle (decreasing just 10% relative with a quadrupling of pressure from 85 to 350 MPa), but the correlation is statistically significant (R^2=0.76). The experimentally calibrated K_2O-in-glass barometer is consistent with equilibration at P_{Total} of 250-350 MPa. Importantly, the H_2O-undersaturated experiments demonstrate that given sufficient dissolved H_2O (here, > 6.3 wt.%), the glass-match occurs even if $P_{H2O}<P_{Total}$. Thus, the glass-match method applied to the in-band experimental run products provides two constraints on the storage depth of the Pudahuel rhyolite: (a) P_{Total} was likely >275 MPa (~10 km depth, considering a crust density of 2700 kg m^{-3} (Anderson, 1989)), and more likely near 300-350 MPa (~11-13 km depth), and (b) the magma may not have been saturated with H_2O; the compositional match occurs when the magma contains sufficient dissolved H_2O to stabilize biotite, whether or not it is H_2O-saturated.

In-band H_2O saturated experiments were expected to produce plagioclase with an anorthite content similar to the natural sample for a range of different P-T-H_2O conditions. However, most of them produce crystals with a more calcic composition (except for one run at 700 ºC, 310 MPa, fO_2 NNO-2, which has plagioclase An_{15-23}, Fig. 11). This is consistent with plagioclase-liquid equilibrium: higher dissolved melt H_2O drives plagioclase to higher An content (Gardner et al., 1995; Sisson and Grove, 1993; Waters and Lange, 2015). This functional dependence is slightly stronger for plagioclase $<An_{30}$. On the other hand, an undersaturated experiment (run 15) reproduces plagioclase crystals with An content that matches the natural crystals. The other in-band undersaturated experiment contains plagioclase crystals that match the natural plagioclase composition, but the crystal textures are ambiguous, and stability is hard to establish. This ambiguity may be related to the multi-stage experimental history of these charges, having been used in predecessor (H_2O-saturated) experiments, coupled with extremely sluggish diffusive homogenization kinetics associated with coupled Ca-Al for Na-Si exchange (Grove et al., 1984). The fact that the H_2O-undersaturated run 15 fulfills the glass match criterion, as mentioned above, further indicates that magmatic H_2O-undersaturation cannot be ruled out on the basis of the experimental results.

5.3. Storage conditions of Pudahuel eruption

Caldera forming eruptions are often associated with very shallow reservoirs (< 5 km) (e.g., Coombs and Gardner, 2001; Larsen, 2006), but there are some cases where evidence has been found of deeper magma accumulation (Chesner, 1998; Johnson and Rutherford, 1989; Masturyono et al., 2001; Pamukçu et al., 2020). In the case of the magma that generated the Pudahuel Ignimbrite, our results suggest depths of >10 km (11-13 km). Although this is higher than the most common depths of reservoirs, it correlates well with the complex structural setting of the region. The Diamante caldera is located in an active margin, with the caldera structure itself at the limit between the Aconcagua fold-and-thrust belt to the north, and the Malargüe fold-and-thrust belt to the south (Sruoga et al., 2005a). Beneath the area, a flat detachment at ~10 km depth crosses the entire mountain belt and is the last part of a major east verging ramp-detachment structure that connects the subduction zone with the cordillera and that plays a fundamental role in accommodating shortening during Neogene mountain building (Farías et al., 2010). This last structure could promote magma

accumulation at deep levels, as pre-existing structures favor magma chamber growth and evolution (Hughes and Mahood, 2011). The presence of the fold-and-thrust belt structures can also play a role in the formation and development of the caldera structure, as they represent areas of weakness where the caldera structure can more likely develop but are also useful as potential places of magma accumulation and, therefore, may exert control over the vent location (Acocella, 2007; Cole et al., 2005).

High pressures, especially >300 MPa, work against caldera-forming eruptions of silicic magma. Crystallization of anhydrous minerals, which increases volatile concentrations and drives exsolution ('second boiling') is commonly invoked as a mechanism for developing overpressure that leads to eruption (Caricchi et al., 2014; Cashman and Scheu, 2015; Malfait et al., 2014). However, this mechanism is more relevant to lower pressure storage (i.e., shallow crustal levels), where vapor exsolution into bubbles is sufficient to induce the necessary overpressure and internally trigger the eruption (Tramontano et al., 2017). In contrast, crystallization-driven volatile saturation in deep-seated crustal magma requires commensurately higher extents of crystallization. Moreover, the nearly-aphyric Pudahuel Ignimbrite rhyolite, with biotite as a dominant mineral phase, is a poor candidate for this mechanism. To be viable, the Pudahuel rhyolite would have had to efficiently separate from a mush of anhydrous minerals shortly before eruption. When the reservoir pressure is high, as in the Pudahuel case, the conditions for caldera-forming eruption are less likely to be met via internal mechanisms alone, so external factors are needed to explain the eruption (Allan et al., 2012; Gregg et al., 2012; Pallister et al., 1992).

An important consideration is the geological setting of the region in which the Diamante caldera is located. Regional uplift of between 2 and 1.5 km occurred within the Andean Cordillera, which subsequently denuded at a high rate (Farías et al., 2008). Muñoz-Gómez et al., (2019) propose that this intense denudation took place between 1.1 and 0.1 Ma. They further suggest that crustal melting driven by denudation produced silicic magmas in the region, and specifically the magma that erupted as the Pudahuel Ignimbrite. According to their numerical simulations of magmatic liquid lines of descent, the magma eventually developed overpressure intrinsically when the system achieved saturation with a fluid phase. As their model assumes an ambient starting pressure of 200 MPa, it is not consistent with our finding that the Pudahuel magmatic phase assemblage equilibrated at confining pressures ≥

275 MPa. A numerical modeling effort considering higher pressures (and consequently greater depth), as indicated by the present study, would need to be done in order to determine whether denudation could affect the reservoir.

Given the evidence at hand, volatile-driven magma pressurization is not likely to have triggered the eruption. Other possibilities, such as the injection of fresh magma, must be considered. Burkert et al., (2010) describe different compositions for gray domains within pumices they examined, which could imply such an injection. However, we have not observed such evidence; in fact, BSE imaging and EDS analysis in this study reveal that differences in clast color are associated with local variation in vesicularity rather than composition (Klug and Cashman, 1994). Also, we did not uncover any differences in mineralogy or major element glass compositions among the pumice clasts we examined. Still, dispelling those possibilities requires a concerted effort with targeted sampling and analysis.

6. Conclusions

The storage conditions for the explosive caldera forming Pudahuel eruption were determined in this work by different approaches. Mineralogical constraints indicate a temperature of 717±7 ºC, 6.9-7.6 wt.% H_2O and P_{H2O} of 200-360 MPa. Constraints from reproduction of the natural major phase assemblage and its compositions by equilibrium phase experiments are consistent with mineralogical results. They point to low temperature conditions (700-750 ºC), high P_{Total} (>275 MPa, more likely 300-350 MPa) and high water contents (at least 6 wt.%). Our results indicate that this melt was not necessarily H_2O- saturated, which is reinforced by plagioclase and glass compositions in H_2O-undersaturated experiments closely matching those of the natural sample. Regional settings are also consistent with storage conditions for aphyric magma at relatively deep depths (~10 km). Major crustal structures present beneath the caldera zone at 10 km depth (Farías et al., 2010) may delineate the magma storage zone. An eruption trigger is still not clear, as we find no evidence of external or internal processes having caused pressurization. Nevertheless, there are tectonic events that affected the region over a period of time in which the magmatic system developed and the caldera-forming eruption occurred, and it is reasonable to think that they may be connected. Moreover, the low crystallinity of the erupted magma makes a second-boiling triggering mechanism unlikely. Further research focused on this eruption, complemented by the new constraints on

storage conditions, is necessary to evaluate the hazard posed by future eruptive activity from the Maipo volcano complex.

Acknowledgments

This study was made possible by funding from the ANID-Fondap 15090013 & 15200001 project “Andean Geothermal Center of Excellence (CEGA)”, by National Agency for Research and Development (ANID)/ Scholarship Program/ Doctorado Nacional/ 2016-21160376, and NSF EAR-1347887 to JH. We thank Eric Hellebrand, Will Nelson, Tom Shea for assistance collecting and analyzing microprobe data. We thank Christian Betancourt for comments and suggestions. We are grateful for the very thoughtful and careful reviews by L. Waters, P. Ruprecht, and an anonymous reviewer. This is SOEST publication number 11372.

Table 1. Natural samples pumices and fallout major and trace element compositions

Major elements	d.l. (%)	Analysis method	DAC 1	DAC 4	DAC 5	DAC 6	DAC 8	DAC 10	DAC 11	DAC 12	DAC 13	DAC 14	CPIP 02	CPIP 10	CPIP 12	CPIP 13
SiO_2	0.01	FUS-ICP	73.5	73.78	73.11	73.21	74.09	73.48	72.17	72.98	72.6	72.81	72.23	73.14	74.03	72.94
Al_2O_3	0.01	FUS-ICP	12.78	13.04	12.92	12.8	13.01	12.85	13.59	13.2	13.34	12.79	13.06	12.92	12.88	12.65
TiO_2	0.001	FUS-ICP	0.115	0.12	0.115	0.119	0.118	0.121	0.111	0.142	0.148	0.129	0.122	0.12	0.113	0.113
FeO	0.1	TITR	b.d.l.	b.d.l.	b.d.l.	b.d.l.	b.d.l.	0.4	0.5	0.3	0.2	b.d.l.	1	0.4	0.4	0.3
Fe_2O_3	0.01	FUS-ICP	0.76*	0.77*	0.72*	0.82*	0.8*	0.4	0.17	0.69	0.84	0.84*	b.d.l.	0.35	0.33	0.46
MnO	0.001	FUS-ICP	0.074	0.076	0.071	0.075	0.076	0.077	0.07	0.077	0.076	0.073	0.078	0.075	0.076	0.074
MgO	0.01	FUS-ICP	0.14	0.15	0.15	0.15	0.14	0.15	0.14	0.22	0.24	0.18	0.17	0.14	0.14	0.14
CaO	0.01	FUS-ICP	0.79	0.71	0.77	0.69	0.62	0.63	1.1	1.02	1.48	1.39	0.72	0.61	0.58	0.6
Na_2O	0.01	FUS-ICP	4.11	4.21	4.24	4.2	4.09	4.03	4.34	4.08	4.2	4.06	3.51	3.51	3.47	3.15
K_2O	0.01	FUS-ICP	4.3	4.02	4.04	4.03	4.07	3.96	3.66	3.85	3.8	4.01	4.7	4.67	4.57	4.74
P_2O_5	0.01	FUS-ICP	0.04	0.04	0.05	0.03	0.03	0.03	0.03	0.04	0.05	0.03	0.03	0.03	0.03	0.03
LOI			3.39	3.2	3.54	3.65	3.21	4.32	4.07	3.65	3.39	3.72	4.63	3.17	3.84	4.61
Total			99.99	100.1	99.72	99.77	100.3	100.5	100	100.3	100.4	100	100.3	99.19	100.5	99.84
*Fe as $Fe_2O_{3(Tot)}$																
Trace elements	d.l (ppm)															
Sc	1	FUS-ICP	2	3	2	2	2	2	2	2	2	2	2	2	2	2
Be	1	FUS-ICP	3	3	3	3	3	3	3	3	3	3	3	3	3	3
Zn	30	FUS-MS	b.d.l.	40	30	40	30	30	40	40	40	160	50	50	40	40
Ga	1	FUS-MS	15	16	15	16	15	15	15	16	15	15	15	16	15	15
Rb	2	FUS-MS	148	148	147	143	145	144	133	141	129	141	144	149	142	142
Sr	2	FUS-ICP	69	71	77	75	67	68	131	110	120	81	71	68	62	67
Y	1	FUS-ICP	15	19	14	15	15	15	15	15	15	15	15	16	15	13
Zr	2	FUS-ICP	78	75	73	71	70	80	65	85	91	81	75	78	73	84
Nb	1	FUS-MS	9	9	9	9	10	10	9	10	9	10	10	10	10	10

Mo	2	FUS-MS	2	2	3	3	2	3	2	2	3	3	3	2	2	2
Cs	0.5	FUS-MS	4.2	4.3	4.2	4.2	4.1	4.2	3.9	4.2	4	4.1	4.3	4.2	4.1	4.2
Ba	2	FUS-ICP	747	755	742	746	748	735	728	735	741	762	745	746	762	752
La	0.1	FUS-MS	15.9	19.1	16.1	18.9	16.8	16	16.9	17.3	16.9	17.4	16.1	16.4	14.7	16.3
Ce	0.1	FUS-MS	32.5	37.9	33.6	36.3	34.3	32.7	32.2	35.6	34.2	35.5	33.1	33.9	30.5	33.7
Pr	0.05	FUS-MS	3.43	4.25	3.68	3.68	3.65	3.49	3.32	3.82	3.69	3.87	3.49	3.62	3.3	3.65
Nd	0.1	FUS-MS	11.5	14.3	11.8	12	12.2	11.8	11.2	12.7	12.2	13	11.3	12.3	11	11.9
Sm	0.1	FUS-MS	2.6	2.7	2.5	2.6	2.6	2.6	2.3	2.7	2.6	2.7	2.6	2.6	2.4	2.6
Eu	0.05	FUS-MS	0.4	0.45	0.41	0.41	0.44	0.41	0.54	0.46	0.43	0.44	0.42	0.44	0.39	0.41
Gd	0.1	FUS-MS	2.2	2.7	2.2	2.2	2.3	2.2	2.1	2.3	2.2	2.3	2.1	2.2	2.1	2.2
Tb	0.1	FUS-MS	0.4	0.5	0.4	0.4	0.4	0.4	0.4	0.4	0.4	0.4	0.4	0.4	0.4	0.4
Dy	0.1	FUS-MS	2.3	3.2	2.5	2.4	2.4	2.4	2.3	2.4	2.2	2.4	2.4	2.5	2.4	2.4
Ho	0.1	FUS-MS	0.4	0.7	0.5	0.5	0.5	0.5	0.5	0.5	0.4	0.5	0.5	0.5	0.5	0.5
Er	0.1	FUS-MS	1.3	2	1.3	1.3	1.4	1.4	1.4	1.3	1.3	1.4	1.4	1.4	1.3	1.3
Tm	0.05	FUS-MS	0.2	0.28	0.21	0.21	0.21	0.21	0.21	0.21	0.19	0.21	0.2	0.21	0.2	0.2
Yb	0.1	FUS-MS	1.5	1.8	1.4	1.3	1.4	1.4	1.3	1.5	1.2	1.4	1.4	1.4	1.3	1.4
Lu	0.01	FUS-MS	0.22	0.28	0.22	0.22	0.22	0.22	0.23	0.22	0.19	0.23	0.23	0.21	0.21	0.22
Hf	0.2	FUS-MS	2.6	2.6	2.4	2.3	2.5	2.8	2.2	2.8	2.7	2.7	2.6	2.6	2.5	2.7
Ta	0.1	FUS-MS	1.1	1.1	1.1	1.1	1.1	1.1	1	1.1	1	1.1	1.1	1.1	1.1	1.1
Tl	0.1	FUS-MS	0.8	0.8	0.8	0.8	0.7	0.8	0.7	0.7	0.7	1.2	0.8	0.7	0.7	0.7
Pb	5	FUS-MS	21	24	21	21	18	21	20	21	19	31	21	21	20	20
Th	0.1	FUS-MS	10.4	11.5	11.2	10.9	11.2	10.8	9.8	11.3	10.4	11.2	10.9	11	10.7	11.1
U	0.1	FUS-MS	5.1	5.4	5.3	5.1	5.2	5.1	4.8	5	4.6	5.2	5.1	5.2	5	5.1

b.d.l. below detection limit

Table 2. Natural and experimental glass compositions determined by EMPA.

Sample	*n*	SiO_2 *	σ	TiO_2	σ	Al_2O_3	σ	FeO	σ	NiO	σ	MnO	σ	MgO	σ	CaO	σ	Na_2O	σ	K_2O	σ	P_2O_5	σ	Cl	σ	Total[a]
CPIP13	21	76.64	0.16	0.11	0.03	13.38	0.07	0.63	0.03	-	-	0.09	0.02	0.11	0.01	0.49	0.02	4.25	0.15	4.16	0.13	0.04	0.02	0.10	0.01	96.67
exp 01	12	76.11	0.24	0.17	0.02	13.39	0.10	0.89	0.03	0.07	0.04	0.07	0.03	0.19	0.02	1.16	0.04	3.22	0.12	4.62	0.08	0.05	0.03	0.04	0.01	95.20
exp 02	12	75.78	0.13	0.20	0.03	13.37	0.09	1.07	0.03	0.06	0.05	0.07	0.02	0.23	0.02	1.17	0.02	3.32	0.08	4.62	0.06	0.05	0.02	0.05	0.01	95.74
exp 03	12	76.85	0.23	0.07	0.02	13.21	0.08	0.67	0.05	0.04	0.05	0.08	0.01	0.10	0.02	1.12	0.04	3.25	0.11	4.58	0.08	0.02	0.02	0.00	0.00	94.58
exp 04	15	76.06	0.24	0.07	0.03	13.82	0.12	0.58	0.04	0.06	0.05	0.07	0.02	0.10	0.02	1.40	0.05	3.51	0.11	4.30	0.09	0.03	0.02	0.00	0.00	92.99
exp 07	12	74.51	0.73	0.19	0.03	14.15	0.44	1.12	0.04	0.06	0.05	0.08	0.03	0.37	0.03	1.47	0.12	3.60	0.13	4.40	0.07	0.04	0.02	0.03	0.01	94.24
exp 08	10	75.70	0.14	0.15	0.03	13.49	0.08	1.06	0.02	-	-	0.08	0.02	0.23	0.02	1.35	0.02	3.52	0.10	4.37	0.02	0.03	0.02	0.03	0.01	94.93
exp 09	10	75.56	0.29	0.17	0.03	13.60	0.13	1.03	0.06	-	-	0.08	0.02	0.27	0.02	1.29	0.05	3.30	0.10	4.62	0.10	0.04	0.02	0.03	0.01	94.95
exp 10	10	76.52	0.17	0.08	0.02	13.37	0.08	0.73	0.03	-	-	0.08	0.02	0.11	0.01	1.35	0.04	3.26	0.12	4.44	0.09	0.02	0.02	0.03	0.01	91.86
exp 11	10	75.50	0.18	0.10	0.02	14.01	0.09	0.88	0.04	-	-	0.08	0.02	0.16	0.01	1.52	0.03	3.33	0.10	4.38	0.05	0.02	0.01	0.02	0.01	90.86
exp 12	10	76.19	0.30	0.07	0.02	13.73	0.19	0.66	0.04	-	-	0.08	0.01	0.11	0.02	1.44	0.04	3.43	0.09	4.28	0.03	0.01	0.01	0.00	0.00	92.27
exp 13	10	75.82	0.20	0.07	0.02	14.00	0.12	0.61	0.03	-	-	0.07	0.02	0.10	0.01	1.56	0.04	3.48	0.12	4.27	0.06	0.01	0.01	0.01	0.01	87.86
exp 14	10	76.06	0.18	0.07	0.02	13.81	0.06	0.59	0.02	-	-	0.08	0.01	0.10	0.01	1.48	0.09	3.49	0.10	4.28	0.04	0.03	0.04	0.02	0.01	89.00
exp 15	10	76.10	0.28	0.07	0.03	13.83	0.17	0.62	0.03	-	-	0.07	0.01	0.11	0.01	1.51	0.04	3.43	0.15	4.24	0.05	0.02	0.02	0.00	0.01	87.94
exp 16	10	75.97	0.33	0.07	0.02	13.80	0.13	0.65	0.05	-	-	0.07	0.02	0.11	0.02	1.71	0.04	3.44	0.18	4.11	0.04	0.02	0.01	0.07	0.06	88.58
exp 17	9	77.20	0.37	0.06	0.03	13.23	0.19	0.54	0.07	-	-	0.07	0.02	0.10	0.03	1.06	0.02	3.06	0.12	4.62	0.10	0.02	0.02	0.04	0.02	88.01

*SiO_2 corrected by drift when necessary

[a]Total before normalization value

Table 3. Experimental run conditions and products

Run	Starting Material	Duration (h)	Temperature (ºC)	Pressure Total (MPa)	Pressure H2O (MPa)	Buffer (ΔNNO)	H2O	Phases present[b]
CPIP13[a]	-	-	717±7	202-359	-	+1.35	7.3	Gl, Pl, Bt, Mag, Ilm, Zrn, Ap, Mnz
01	CPIP13	283.6	800	130	130	-2	4.9	Gl, Pl, Opx, Bt, FeTiOx
02	CPIP13	282.8	850	85	85	-2	3.7	Gl, Pl, Opx, FeTiOx, Ap
03	CPIP13	283.9	750	200	200	-2	6.3	Gl, Pl, Opx, Bt, Qzt, FeTiOx, Zrn, Ap, Mnz
04	CPIP13	288	700	310	310	-2	7.8	Gl, Pl, Bt, Qzt, FeTiOx, Ap
07	CPIP13	260.8	850	200	200	-2	5.8	Gl, Pl, Opx, Ap
08	CPIP13	356.3	800	130	130	0	4.9	Gl, Pl, Bt, Opx, Cpx, FeTiOx, Zrn, Ap
09	CPIP13	288.9	850	85	85	0	3.7	Gl, Plg, Opx, FeTiOx, Zrn, Ap
10	CPIP13	303.8	750	200	200	0	6.3	Gl, Pl, Bt, FeTiOx, Ap
11	CPIP13	287.5	750	310	310	0	7.6	Gl, Bt, Zrn, Ap
12	CPIP13	290.4	717	280	280	0	7.3	Gl, Pl, Bt, Zrn, Ap
13	Exp 10	285.9	700	350	200	0	6.3	Gl, Pl, Bt
14	Exp 11	286	700	350	310	0	7.6	Gl, Pl, Bt, Ap
15	Exp 12	286.1	700	350	280	0	7.3	Gl, Pl, Bt, FeTiOx, Zrn, Ap, Mnz
16	CPIP13	286.1	700	350	350	0	7.8	Gl, Pl, Bt, FeTiOx, Ap
17	CPIP13	162.2	700	200	200	0	6.2	Gl, Pl, Bt

a. Natural sample. T-P-H2O obtained by geothermometry and numerical solutions.

b. Gl=glass, Pl=plagioclase, Bt= biotite, Mag= magnetite, Ilm= ilmenite, Zrn=zircon, Ap= apatite, Mnz= monazite, Opx= orthopyroxene, FeTiOx= Fe-Ti oxides, Qzt= quartz, Cpx= clinopyroxene.

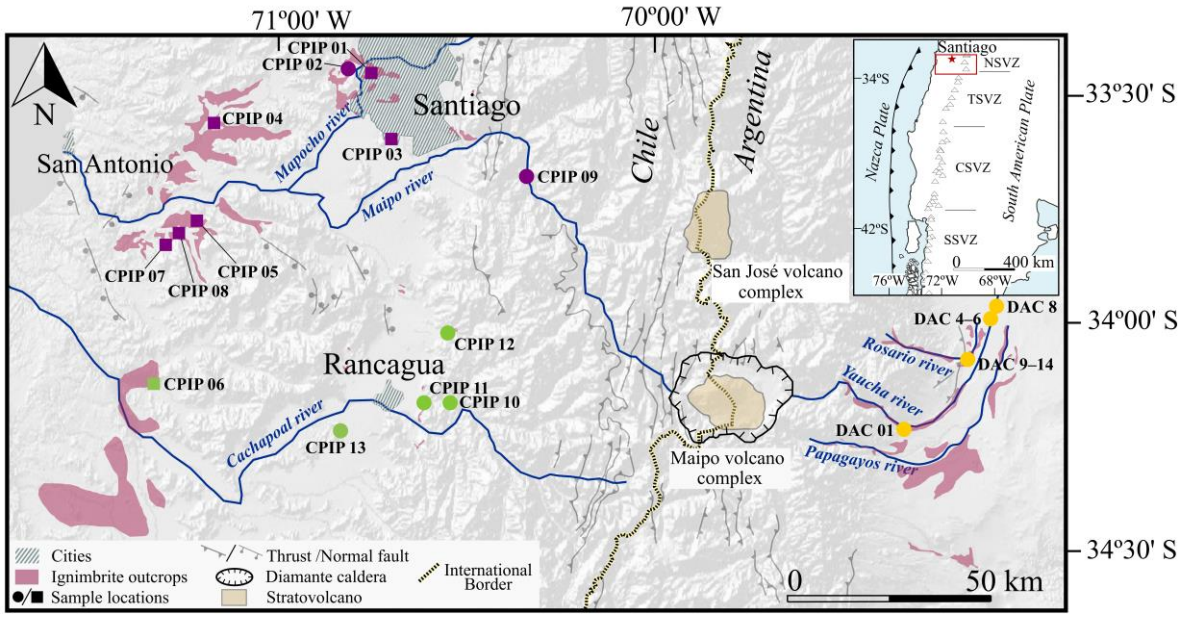

Figure 1: Regional location and tectonic context. Digital elevation model of Central Chile showing the outcrops of the Pudahuel Ignimbrite in pink; data from (Gana et al., 1996; Sellés and Gana, 2001; SERNAGEOMIN, 2003; Sruoga et al., 2005a; Stern et al., 1984; Wall et al., 1999, 1996). Diamante caldera, Maipo volcano, and cities are indicated. Locations of samples used in this study are shown: squares represent samples taken only for general description; circles represent samples taken for geochemical analyses (see text). Rivers are located in their homonymous valley, except for the Mapocho river, which belongs to the Maipo valley. Samples are colored according to the valley where they were taken: Samples from Maipo valley are purple, from Cachapoal valley are green and from Yaucha valley are yellow. Inset figure shows location and volcanoes of the South Volcanic Zone (SVZ) and its segments: northern, transition, central and southern volcanic zones (NSVZ, TSVZ, CSVZ and SSVZ respectively), modified from Stern et al., (2007).

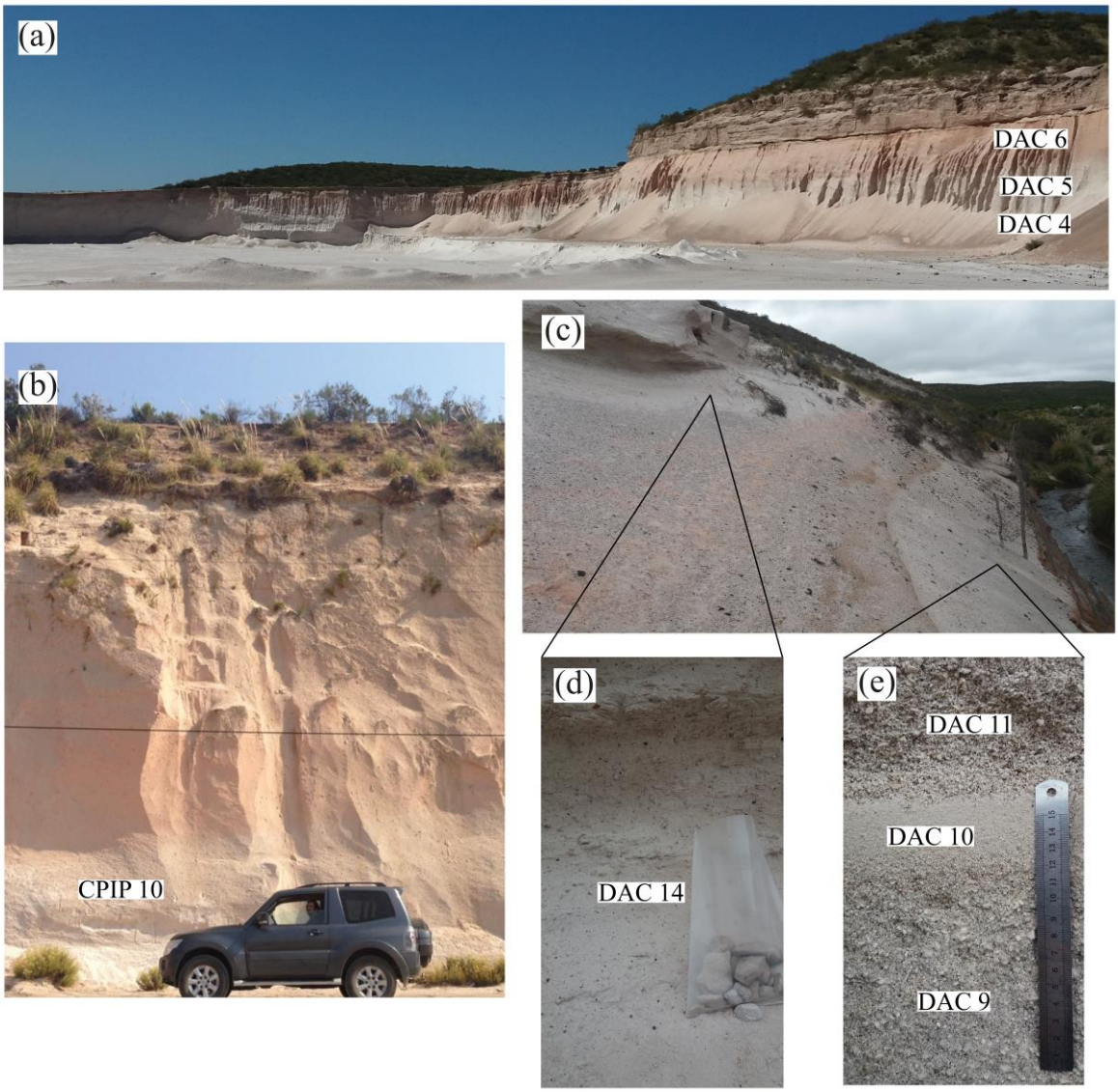

Figure 2: Main outcrop characteristics. a) Pyroclastic density current (PDC) outcrop in a quarry in Papagayos valley, Argentina; b) outcrop in Carretera del Cobre, Cachapoal valley, Chile; c) outcrop in Yaucha valley, Argentina; d) detail of the PDC; e) detail of fall deposit units. Dashes lines in a) and b) show the abrupt change in the ash color present in some outcrops in the PDC deposits.

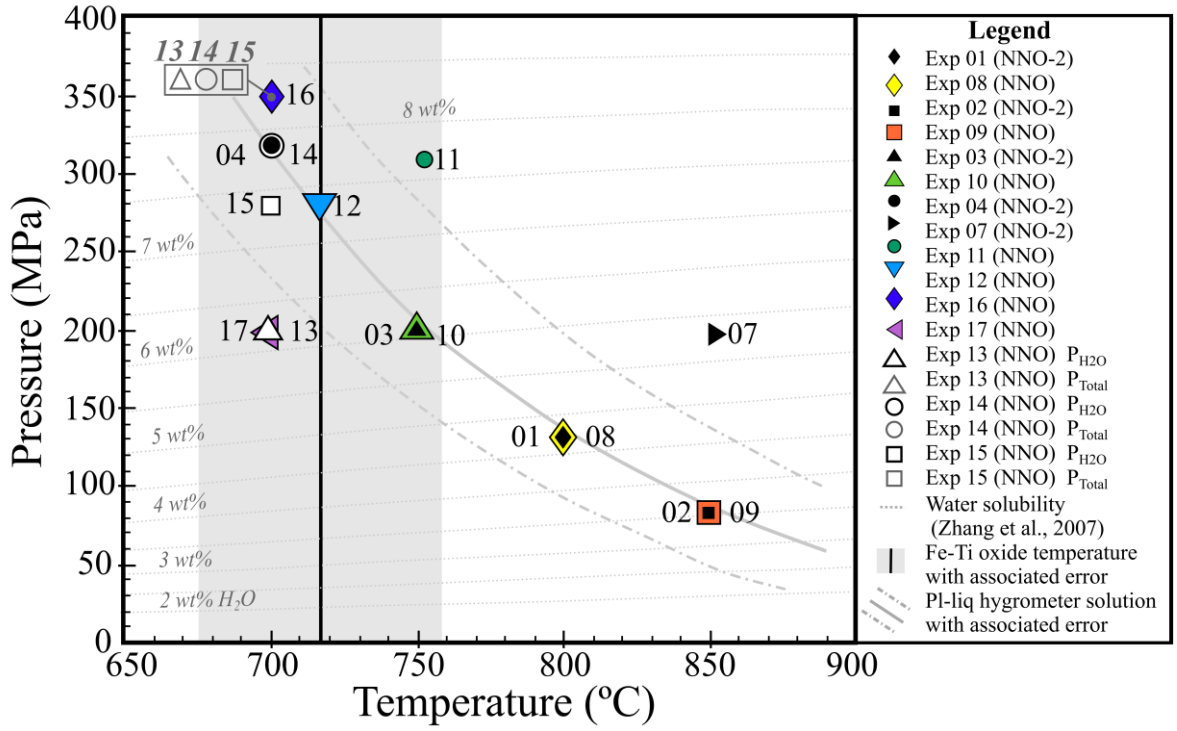

Figure 3: Pressure-temperature space showing experimental run conditions. The central gray line shows the conditions at which the plagioclase-liquid hygrometer is satisfied for the natural glass at different temperatures, the two parallel gray dash-dotted lines represent the associated error of the method. The vertical black line marks the temperature inferred from Fe-Ti oxide geothermometer (Ghiorso and Evans, 2008) and the gray vertical band around it represents the average absolute deviation for the method assessed by (Blundy and Cashman, 2008). Gray sub-horizontal dashed lines are the expected concentrations of H_2O for the melt (Zhang et al., 2007).

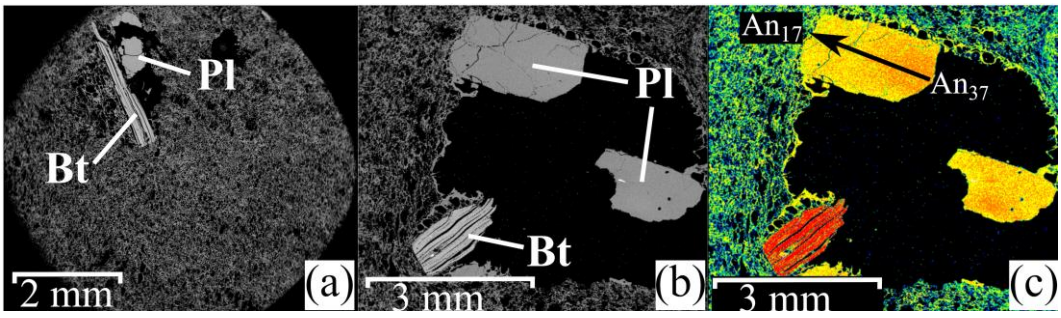

Figure 4: BSE images from CPIP13 sample. a) glass matrix, highly vesicular, with cumulus of an unzoned plagioclase and biotite phenocryst, b) detail of a zoned plagioclase and biotite cumulus, c) altered colors of image b to highlight the normal zonation of the plagioclase.

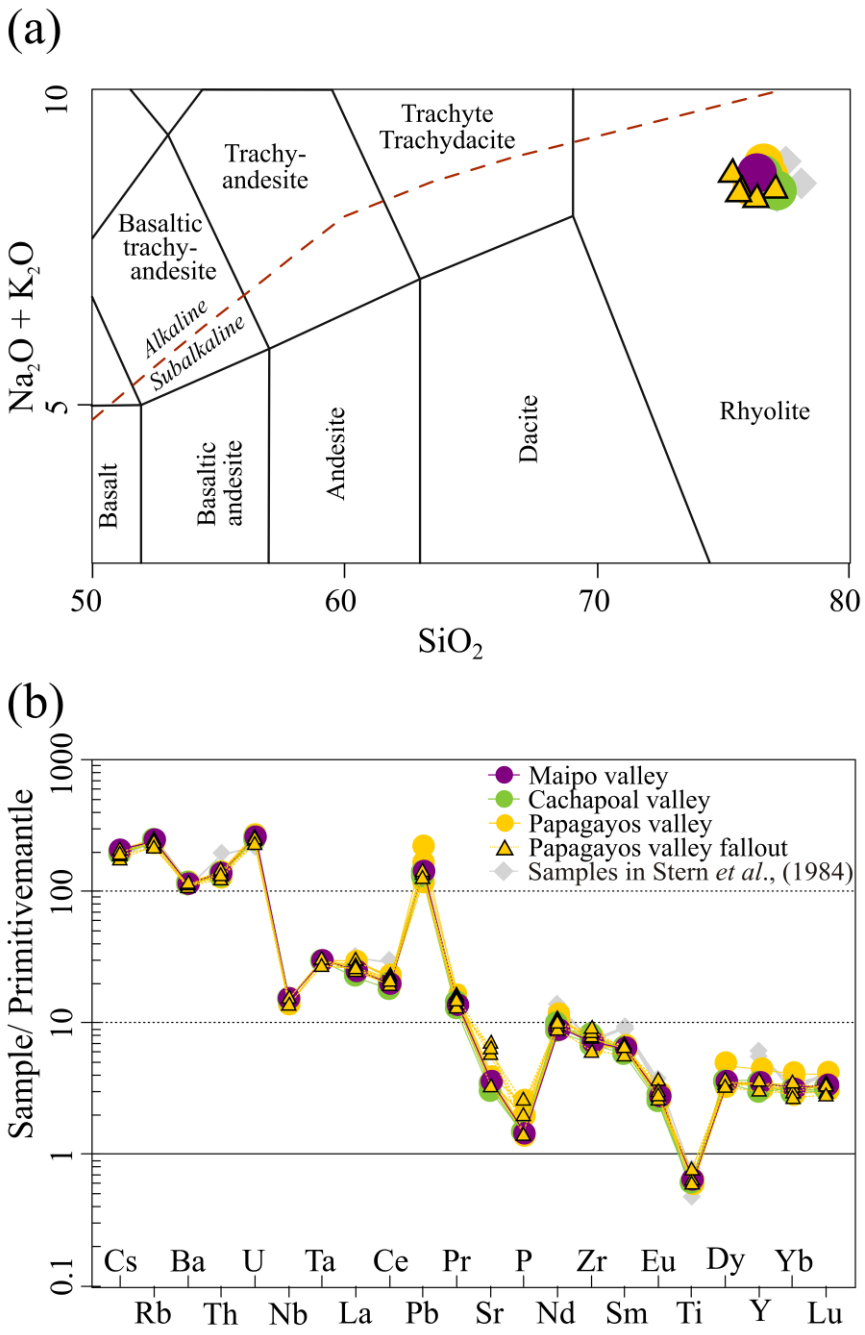

Figure 5: Main geochemical characteristics. a) TAS diagram showing the classification of the PDC samples from different valleys as rhyolite (Le Bas et al., 1986); b) Spider diagram normalized to primitive mantle (McDonough and Sun, 1995). Data from (Stern et al., 1984) are shown to compare.

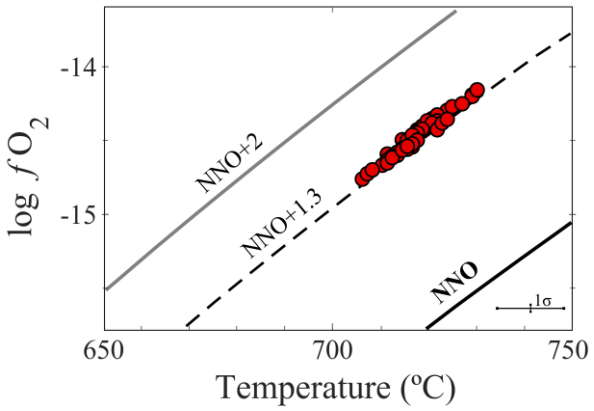

Figure 6: Temperature-oxygen fugacity relationships from Fe-Ti oxide geothermometry (Ghiorso and Evans, 2008).

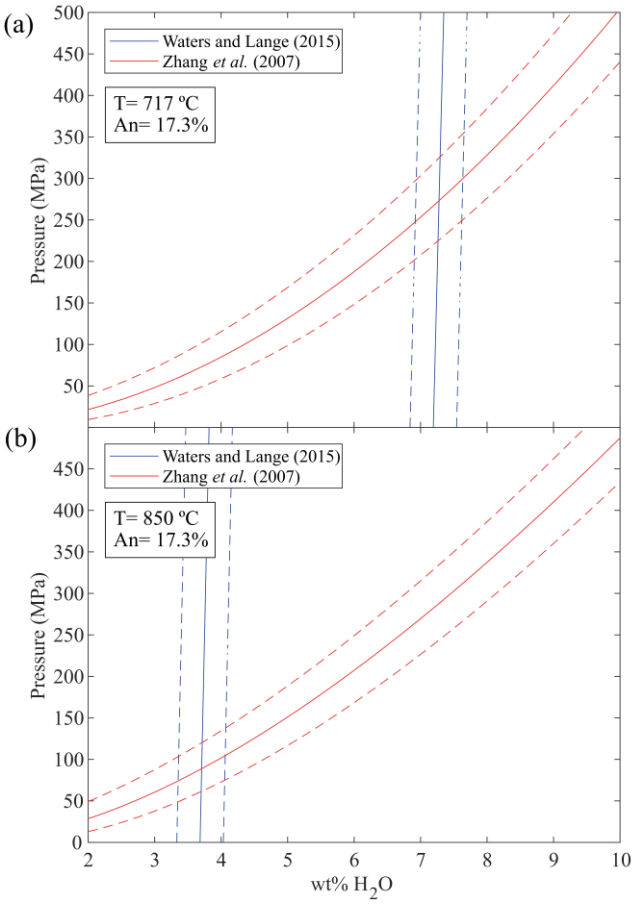

Figure 7: Numerical solution to determine pressure conditions and water content in samples. a) solution obtained with geothermometer temperature results; b) solution obtained for a higher temperature. Blue line represents the equation of Waters and Lange, (2015) and blue dashed lines its uncertainties, red line represents the equation of (Zhang et al., 2007) and the

red dashed lines its uncertainties. Each solution corresponds to a field, and the center was the point considered to perform an experiment.

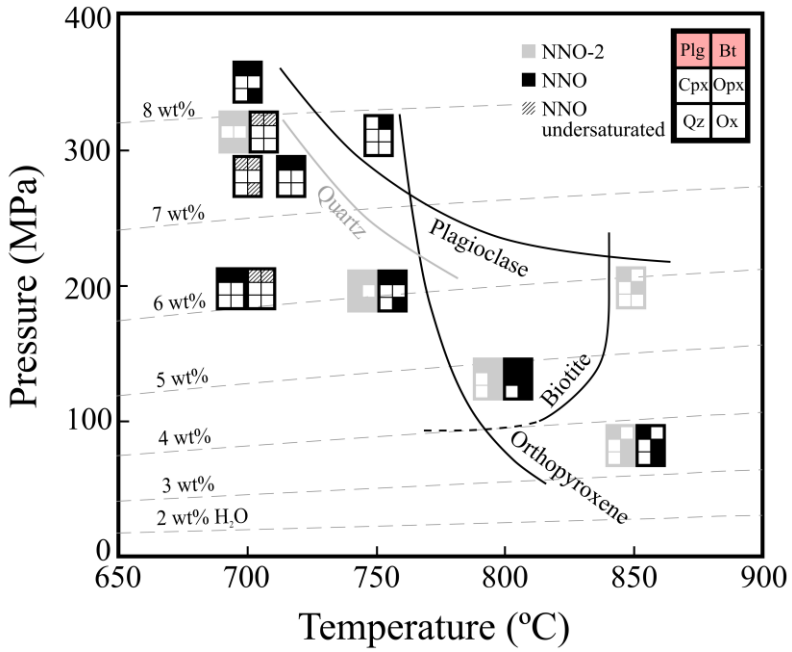

Figure 8: P-T phase diagram. Each symbol is an experiment; black symbols are H_2O saturated experiments conducted at fO_2 NNO; gray symbols are saturated experiments at fO_2 NNO-2. Symbols filled with line pattern show H_2O undersaturated experiments. Each sub-square shows the mineral phases grown in each experiment. Pink sub-square in the upper part indicates the phases present in the natural sample (plagioclase and biotite). Black curves show approximate region of mineral stability in both batches of experiments (the ones run at NNO and the ones run at NNO-2). Gray curves mark stability regions of minerals detected only for NNO-2 batches. Plg: plagioclase, Bt: biotite, Cpx: clinopyroxene, Opx: orthopyroxene, Qz: quartz, Ox: iron-titanium oxide (ilmenite or magnetite).

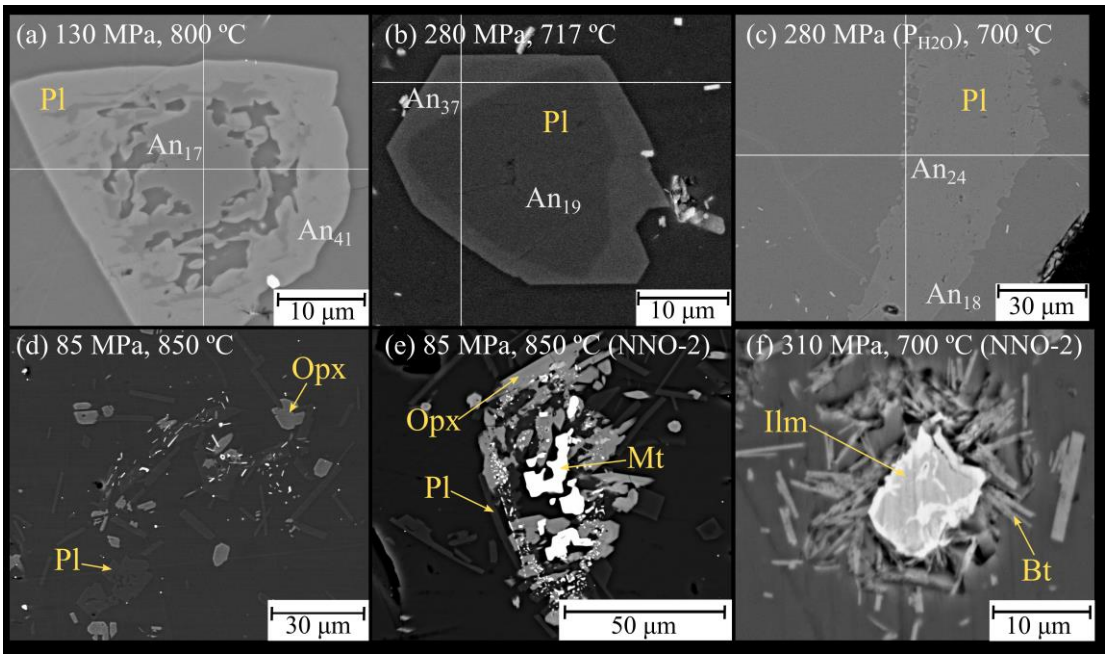

Figure 9: BSE images of experimental run products. a) Plagioclase from natural sample reacting (center) with an overgrowth rim with a calcic composition; b) overgrowth rim in plagioclase; c) plagioclase crystal from an undersaturated experiment (P_{Total} = 350 MPa); d) orthopyroxene (low-Ca pyroxene) with plagioclase in cumulus, both phases have euhedral crystals; e) orthopyroxene associated with plagioclase and magnetite; f) biotite surrounding ilmenite. Plg: plagioclase, An: anorthite, Opx: orthopyroxene, Mt: magnetite, Ilm: ilmenite, Bt: biotite.

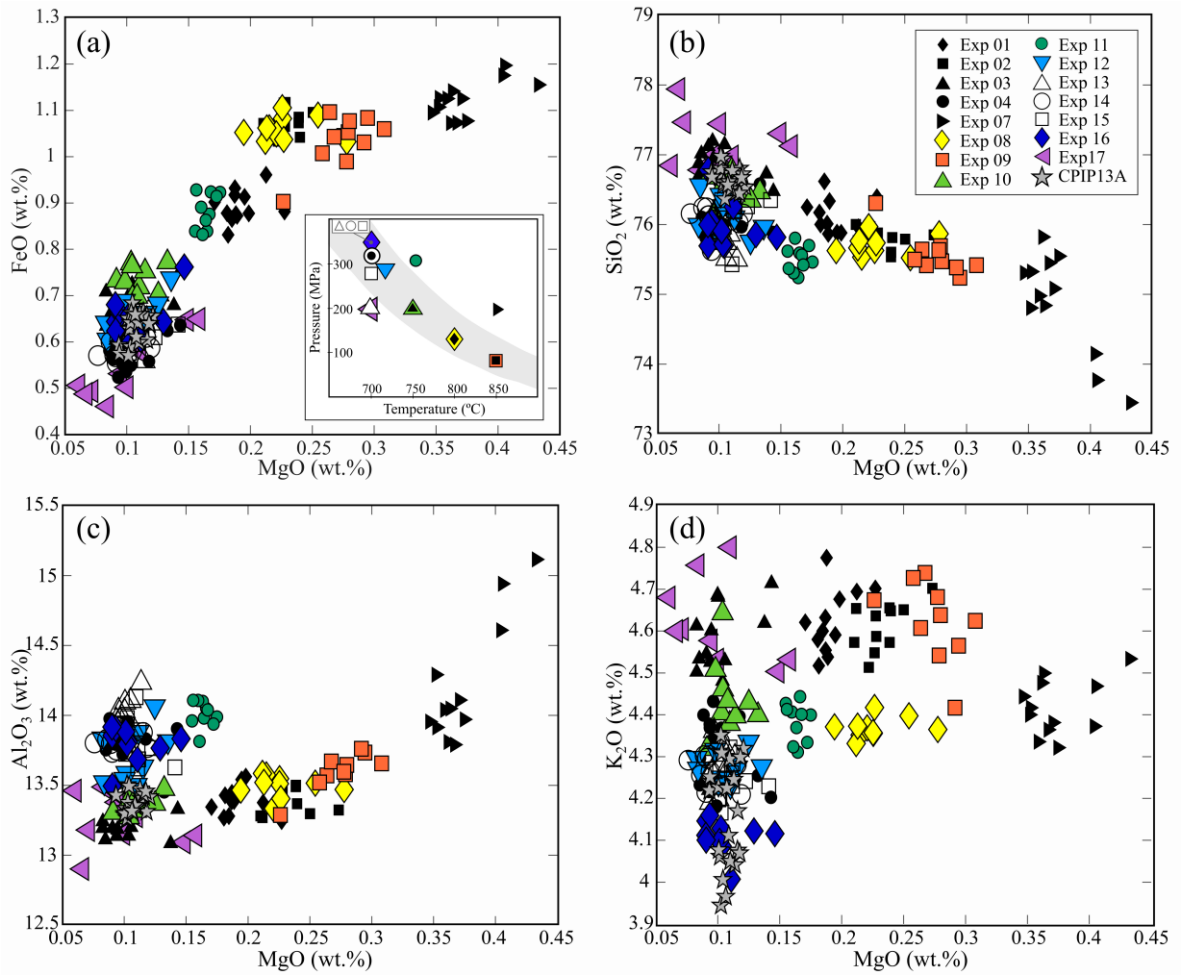

Figure 10: Experimental and natural glass compositions. Analytical errors are smaller than symbols.

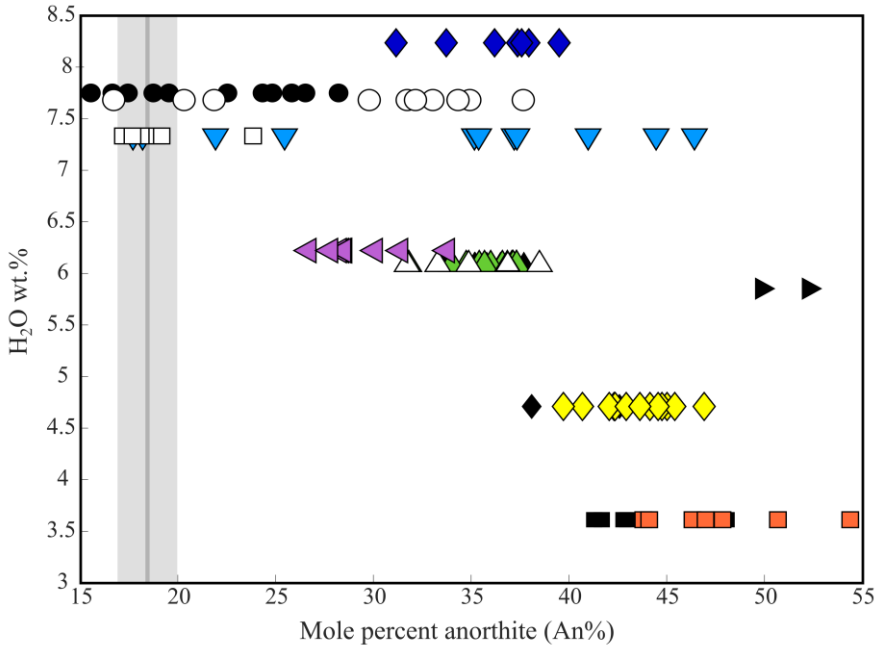

Figure 11: Plagioclase mole percent of anorthite (An%) in experimental and natural samples. Only compositions of the rims of the crystals in contact with glass are shown. The gray line represents the average natural plagioclase composition in contact with glass; the gray band is the standard deviation. Analytical errors are smaller than the symbols.

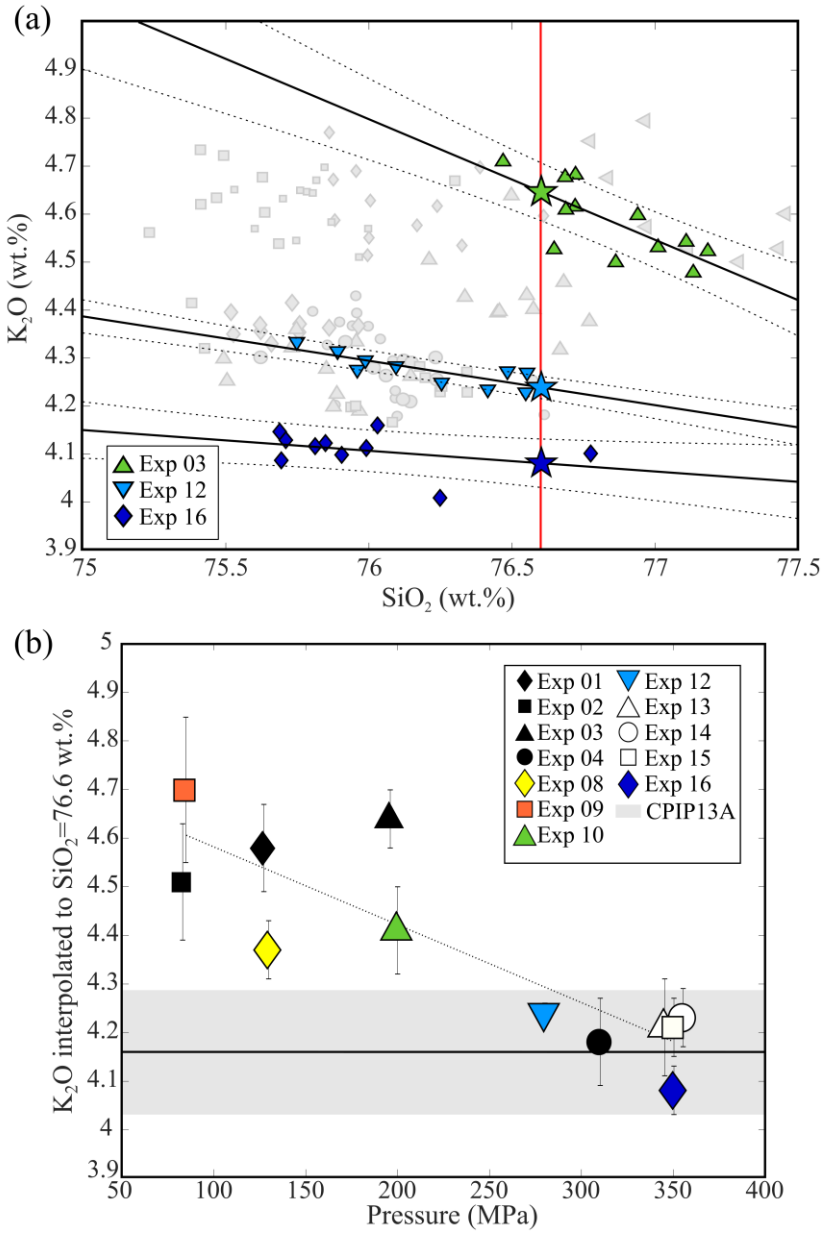

Figure 12: a) K_2O versus SiO_2, showing the fitted line (in black) for K_2O experimental data to the 76.6 wt.% SiO_2 content (red vertical line) for three in-band experiments (03, 12 and 16). Dotted lines show the standard error of the method. Other experimental and the natural glass compositions are shown in gray. b) $[K_2O]_{76.6}$ versus P_{Total} of the in-band experiments. For clarity, the low-fO_2 experiment symbols are plotted at 0.98 P_{Total} rather than P_{Total}. The error bars for each symbol are the standard error for the method at 76.6 wt.% SiO_2 shown in a). The horizontal black line is the natural glass mean K_2O content and the gray bar around it is its standard deviation.

7. References

Acocella, V., 2007. Understanding caldera structure and development: An overview of analogue models compared to natural calderas. Earth-Science Rev. 85, 125–160. https://doi.org/10.1016/j.earscirev.2007.08.004

Allan, A.S.R., Wilson, C.J.N., Millet, M.A., Wysoczanski, R.J., 2012. The invisible hand: Tectonic triggering and modulation of a rhyolitic supereruption. Geology 40, 563–566. https://doi.org/10.1130/G32969.1

Anderson, D.L., 1989. Theory of the Earth. Blackwell Scientific Publications.

Andrews, B.J., 2014. Magmatic storage conditions, decompression rate, and incipient caldera collapse of the 1902 eruption of Santa Maria Volcano, Guatemala. J. Volcanol. Geotherm. Res. 282, 103–114. https://doi.org/10.1016/j.jvolgeores.2014.06.009

Bachmann, O., 2010. The petrologic evolution and pre-eruptive conditions of the rhyolitic Kos Plateau Tuff (Aegean arc). Cent. Eur. J. Geosci. 2, 270–305. https://doi.org/10.2478/v10085-010-0009-4

Bacon, C.R., Hirschmann, M.M., 1988. Mg/Mn partitioning as a test for equilibrium between coexisting Fe-Ti oxides. Am. Mineral. 73, 57–61.

Baker, D.R., 1992. Tracer diffusion of network formers and multicomponent diffusion in dacitic and rhyolitic melts. Geochim. Cosmochim. Acta 56, 617–631. https://doi.org/10.1016/0016-7037(92)90086-X

Barclay, J., Rutherford, M.J., Carroll, M.R., Murphy, M.D., Devine, J.D., Gardner, J., Sparks, R.S.J., 1998. Experimental phase equilibria constraints on preemptive storage conditions of the Soufriere Hills magma. Geophys. Res. Lett. 25, 3437–3440. https://doi.org/10.1029/98GL00856

Befus, K.S., Gardner, J.E., 2016. Magma storage and evolution of the most recent effusive

and explosive eruptions from Yellowstone Caldera. Contrib. to Mineral. Petrol. 171. https://doi.org/10.1007/s00410-016-1244-x

Befus, K.S., Zinke, R.W., Jordan, J.S., Manga, M., Gardner, J.E., 2014. Pre-eruptive storage conditions and eruption dynamics of a small rhyolite dome: Douglas Knob, Yellowstone volcanic field, USA. Bull. Volcanol. 76, 1–12. https://doi.org/10.1007/s00445-014-0808-8

Blatter, D.L., Sisson, T.W., Hankins, W. Ben, 2017. Voluminous arc dacites as amphibole reaction-boundary liquids, Contributions to Mineralogy and Petrology. Springer Berlin Heidelberg. https://doi.org/10.1007/s00410-017-1340-6

Blundy, J., Cashman, K., 2008. Petrologic reconstruction of magmatic system variables and processes. Rev. Mineral. Geochemistry 69, 179–239. https://doi.org/10.2138/rmg.2008.69.6

Brugger, C.R., Hammer, J.E., 2010. Crystallization kinetics in continuous decompression experiments: Implications for interpreting natural magma ascent processes. J. Petrol. 51, 1941–1965. https://doi.org/10.1093/petrology/egq044

Burkert, C., Freundt, A., Gilbert, D., Kutterolf, S., 2010. Origin of magmatic components in the Diamante Tuff, in: SFB 574 Subduction Workshop. Pucón.

Carey, S., Sigurdsson, H., 1989. The intensity of plinian eruptions. Bull. Volcanol. 51, 28–40. https://doi.org/10.1007/BF01086759

Caricchi, L., Annen, C., Blundy, J., Simpson, G., Pinel, V., 2014. Frequency and magnitude of volcanic eruptions controlled by magma injection and buoyancy. Nat. Geosci. 7, 126–130. https://doi.org/10.1038/ngeo2041

Cashman, K. V, Scheu, B., 2015. Magmatic fragmentation. Encycl. Volcanoes 459–471.

Castro, J.M., Schipper, C.I., Mueller, S.P., Militzer, A.S., Amigo, A., Parejas, C.S., Jacob,

D., 2013. Storage and eruption of near-liquidus rhyolite magma at Cordón Caulle, Chile. Bull. Volcanol. 75, 1–17. https://doi.org/10.1007/s00445-013-0702-9

Chesner, C.A., 1998. Petrogenesis of the Toba Tuffs, Sumatra, Indonesia. J. Petrol. 39, 397–438. https://doi.org/10.1093/petroj/39.3.397

Cole, J.W., Milner, D.M., Spinks, K.D., 2005. Calderas and caldera structures: A review. Earth-Science Rev. 69, 1–26. https://doi.org/10.1016/j.earscirev.2004.06.004

Coombs, M.L., Gardner, J.E., 2001. Shallow-storage conditions for the rhyolite of the 1912 eruption at Novarupta, Alaska. Geology 29, 775–778. https://doi.org/10.1130/0091-7613(2001)029<0775:SSCFTR>2.0.CO;2

Deering, C.D., Bachmann, O., Vogel, T.A., 2011. The Ammonia Tanks Tuff: Erupting a melt-rich rhyolite cap and its remobilized crystal cumulate. Earth Planet. Sci. Lett. 310, 518–525. https://doi.org/10.1016/j.epsl.2011.08.032

Devine, J.D., Gardner, J.E., Brack, H.P., Layne, G.D., Rutherford, M.J., 1995. Comparison of microanalytical methods for estimating H2O contents of silicic volcanic glasses. Am. Mineral. 80, 319–328. https://doi.org/10.2138/am-1995-3-413

Dingwell, D., 1998. Magma degassing and fragmentation: recent experimental advances. From Magma to Tephra-Modelling Phys. Process. … 1–23.

Druitt, T.H., Sparks, R.S.J., 1984. On the formation of calderas during ignimbrite eruptions. Nature 310, 679–681. https://doi.org/10.1038/310679a0

Farías, M., Charrier, R., Carretier, S., Martinod, J., Fock, A., Campbell, D., Cáceres, J., Comte, D., 2008. Late Miocene high and rapid surface uplift and its erosional response in the Andes of central Chile (33° - 35°S). Tectonics 27. https://doi.org/10.1029/2006TC002046

Farías, M., Comte, D., Charrier, R., Martinod, J., David, C., Tassara, A., Tapia, F., Fock, A.,

2010. Crustal-scale structural architecture in central Chile based on seismicity and surface geology: Implications for Andean mountain building. Tectonics 29. https://doi.org/10.1029/2009TC002480

First, E.C., Hammer, J.E., Ruprecht, P., Rutherford, M., 2021. Experimental constraints on dacite magma storage beneath Volcán Quizapu, Chile. J. Petrol. 62. https://doi.org/10.1093/petrology/egab027

Futa, K., Stern, C.R., 1988. Sr and Nd isotopic and trace element compositions of Quaternary volcanic centers of the Southern Andes. Earth Planet. Sci. Lett. 88, 253–262. https://doi.org/10.1016/0012-821X(88)90082-9

Gana, P., Wall, R., Gutiérrez, Á., 1996. Mapa Geológico Del Área De Valparaíso- Curacaví, Regiones de Valparaíso y Metropolitana, Servicio Nacional de Geología y Minería, Mapa Geológico Nº 1, 1 mapa escala 1:100.000. Santiago.

Gardner, J.E., Befus, K.S., Gualda, G.A.R., Ghiorso, M.S., 2014. Experimental constraints on rhyolite-MELTS and the Late Bishop Tuff magma body. Contrib. to Mineral. Petrol. 168, 1–14. https://doi.org/10.1007/s00410-014-1051-1

Gardner, J.E., Rutherford, M., Carey, S., Sigurdsson, H., 1995. Experimental constraints on pre-eruptive water contents and changing magma storage prior to explosive eruptions of Mount St Helens volcano. Bull. Volcanol. 57, 1–17. https://doi.org/10.1007/BF00298703

Ghiorso, M.S., Evans, B.W., 2008. Thermodynamics of rhombohedral oxide solid solutions and a revision of the Fe-Ti two-oxide geothermometer and oxygen-barometer. Am. J. Sci. 308, 957–1039. https://doi.org/10.2475/09.2008.01

Giordano, D., Russell, J.K., Dingwell, D.B., 2008. Viscosity of magmatic liquids: A model. Earth Planet. Sci. Lett. 271, 123–134. https://doi.org/10.1016/j.epsl.2008.03.038

Gottsmann, J., Lavallée, Y., Martí, J., Aguirre-Díaz, G., 2009. Magma-tectonic interaction and the eruption of silicic batholiths. Earth Planet. Sci. Lett. 284, 426–434. https://doi.org/10.1016/j.epsl.2009.05.008

Gottsmann, J., Martí, J. (Eds.), 2008. Caldera Volcanism Analysis, Modeling and Response, Developments in Volcanology.

Gregg, P.M., De Silva, S.L., Grosfils, E.B., Parmigiani, J.P., 2012. Catastrophic caldera-forming eruptions: Thermomechanics and implications for eruption triggering and maximum caldera dimensions on Earth. J. Volcanol. Geotherm. Res. 241–242, 1–12. https://doi.org/10.1016/j.jvolgeores.2012.06.009

Gudmundsson, A., 2008. Chapter 8 Magma-Chamber Geometry, Fluid Transport, Local Stresses and Rock Behaviour During Collapse Caldera Formation. Dev. Volcanol. https://doi.org/10.1016/S1871-644X(07)00008-3

Guerstein, P.G., 1993. Origen y significado geológico de la asociación piroclástica pumícea. Preistoceno de la Provincia de Mendoza entre los 33°30' y 34°40' L.S. Universidad Nacional de La Plata, La Plata.

Hammer, J.E., Rutherford, M.J., 2002. An experimental study of the kinetics of decompression-induced crystallization in silicic melt. J. Geophys. Res. Solid Earth 107, ECV 8-1-ECV 8-24. https://doi.org/10.1029/2001jb000281

Hammer, J.E., Rutherford, M.J., Hildreth, W., 2002. Magma storage prior to the 1912 eruption at Novarupta, Alaska. Contrib. to Mineral. Petrol. 144, 144–162. https://doi.org/10.1007/s00410-002-0393-2

Hammond, P.A., Taylor, L.A., 1982. The ilmenite/titano-magnetite assemblage: kinetics of re-equilibration. Earth Planet. Sci. Lett. 61, 143–150. https://doi.org/10.1016/0012-821X(82)90047-4

Harrington, R., 1989. The Diamante Caldera and Maipo Caldera Complex in the Southern Andes of Argentina and Chile (34º 10' south). Rev. la Asoc. Geológica Argentina 19, 186–193.

Hildreth, W., 1981. Gradients in Silicic Magma Chambers ' Implications for Lithospheric Magmatism of the processes and paths by which magmas originate and (with or without some residue) and to have been ' emplaced ' Sampling of igneous rocks from the lunar surface and (st.

Hildreth, W., Drake, R.E., 1992. Volcán Quizapu, Chilean Andes. Bull. Volcanol. 54, 93–125. https://doi.org/10.1007/BF00278002

Hildreth, W., Godoy, E., Fierstein, J., Singer, B.S., 2010. Laguna del Maule volcanic field: Eruptive history of a Quaternary basalt to rhyolite distributed volcanic field on the Andean range crest in central Chile. Serv. Nac. Geol. y Mineria, Bolletin 63, 145.

Hildreth, W., Moorbath, S., 1988. Crustal contributions to arc magmatism in the Andes of Central Chile. Contrib. to Mineral. Petrol. 98, 455–489. https://doi.org/10.1007/BF00372365

Hughes, G.R., Mahood, G.A., 2011. Silicic calderas in arc settings: Characteristics, distribution, and tectonic controls. Bull. Geol. Soc. Am. 123, 1577–1595. https://doi.org/10.1130/B30232.1

Hynek, S.A., Marchetti, D.W., Fernandez, D.P., Cerling, T.E., 2010. Composition, pre-eruptive zonation, and geochronologic significance of the ~450ka Diamante Tuff, Andean Cordillera (34°S), Argentina. Quat. Geochronol. 5, 591–601. https://doi.org/10.1016/j.quageo.2010.02.002

Jambon, A., 1982. Tracer diffusion in granitic melts: Experimental results for NA, K, RB, CS, CA, SR, BA, CE, EU to 1300°C and a model of calculation. J. Geophys. Res. Solid

Earth 87, 10797–10810. https://doi.org/https://doi.org/10.1029/JB087iB13p10797

Jaupart, C., Allègre, C.J., 1991. Gas content, eruption rate and instabilities of eruption regime in silicic volcanoes. Earth Planet. Sci. Lett. 102, 413–429. https://doi.org/10.1016/0012-821X(91)90032-D

Jellinek, A.M., DePaolo, D.J., 2003. A model for the origin of large silicic magma chambers: Precursors of caldera-forming eruptions. Bull. Volcanol. 65, 363–381. https://doi.org/10.1007/s00445-003-0277-y

Johnson, M.C., Rutherford, M.J., 1989. Experimentally determined conditions in the fish canyon tuff, Colorado, magma chamber. J. Petrol. 30, 711–737. https://doi.org/10.1093/petrology/30.3.711

Klug, C., Cashman, K. V., 1994. Vesiculation of May 18, 1980, Mount St. Helens magma. Geology 22, 468–472. https://doi.org/10.1130/0091-7613(1994)022<0468:VOMMSH>2.3.CO;2

Lara, L., Wall, R., Stockli, D., 2008. La ignimbrita Pudahuel (Asociación Piroclástica Pumícea) y la caldera Diamante (33° S): nuevas edades U–Th–He, in: XVII Congreso Geológico Argentino. p. 1365.

Larsen, J.F., 2006. Rhyodacite magma storage conditions prior to the 3430 yBP caldera-forming eruption of Aniakchak volcano, Alaska. Contrib. to Mineral. Petrol. 152, 523–540. https://doi.org/10.1007/s00410-006-0121-4

Le Bas, M.J.L., Maitre, R.W.L., Streckeisen, A., Zanettin, B., 1986. A chemical classification of volcanic rocks based on the total alkali-silica diagram. J. Petrol. 27, 745–750. https://doi.org/10.1093/petrology/27.3.745

Lindsay, J.M., De Silva, S., Trumbull, R., Emmermann, R., Wemmer, K., 2001a. La Pacana caldera, N. Chile: A re-evaluation of the stratigraphy and volcanology of one of the

world's largest resurgent calderas. J. Volcanol. Geotherm. Res. 106, 145–173. https://doi.org/10.1016/S0377-0273(00)00270-5

Lindsay, J.M., Schmitt, A.K., Trumbull, R.B., De Silva, S.L., Siebel, W., Emmermann, R., 2001b. Magmatic Evolution of the La Pacana Caldera System, Central Andes, Chile: Compositional Variation of Two Cogenetic, Large-Volume Felsic Ignimbrites. J. Petrol. 42, 459–486. https://doi.org/10.1093/petrology/42.3.459

Lipman, P.W., 2007. Incremental assembly and prolonged consolidation of Cordilleran magma chambers: Evidence from the Southern Rocky Mountain volcanic field. Geosphere 3, 42–70. https://doi.org/10.1130/GES00061.1

Lipman, P.W., 2000. Calderas. Encycl. Volcanoes 643–662.

Liu, Y., Zhang, Y., Behrens, H., 2005. Solubility of H2O in rhyolitic melts at low pressures and a new empirical model for mixed H2O-CO2 solubility in rhyolitic melts. J. Volcanol. Geotherm. Res. 143, 219–235. https://doi.org/10.1016/j.jvolgeores.2004.09.019

Malfait, W.J., Seifert, R., Petitgirard, S., Perrillat, J.P., Mezouar, M., Ota, T., Nakamura, E., Lerch, P., Sanchez-Valle, C., 2014. Supervolcano eruptions driven by melt buoyancy in large silicic magma chambers. Nat. Geosci. 7, 122–125. https://doi.org/10.1038/ngeo2042

Martel, C., 2012. Eruption dynamics inferred from microlite crystallization experiments: Application to plinian and dome-forming eruptions of Mt. Pelée (martinique, lesser antilles). J. Petrol. 53, 699–725. https://doi.org/10.1093/petrology/egr076

Marti, J., Ablay, G.J., Redshaw, L.T., Sparks, R.S.J., 1994. Experimental studies of collapse calderas. J. Geol. Soc. London. 151, 919–929. https://doi.org/10.1144/gsjgs.151.6.0919

Masturyono, McCaffrey, R., Wark, D.A., Roecker, S.W., Fauzi, Ibrahim, G., Sukhyar, 2001.

Distribution of magma beneath the Toba caldera complex, north Sumatra, Indonesia, constrained by three-dimensional P wave velocities, seismicity, and gravity data. Geochemistry, Geophys. Geosystems 2. https://doi.org/10.1029/2000GC000096

McDonough, W.F., Sun, S. s., 1995. The composition of the Earth. Chem. Geol. 120, 223–253. https://doi.org/10.1016/0009-2541(94)00140-4

Moore, G., Vennemann, T., Carmichael, I.S.E., 1998. An empirical model for the solubility of H 2 O in magmas to 3 kilobars. Am. Mineral. 83, 36–42. https://doi.org/10.2138/am-1998-1-203

Muñoz-Gómez, M., Payacán, Í., Gutiérrez, F., Farías, M., Charrier, R., Polvé, M., 2019. Silicic volcanism triggered by increased denudation rates in the Quaternary Andean arc of central Chile between 33°50′-34°30′S. Lithos 355. https://doi.org/10.1016/j.lithos.2019.105242

National Academies of Sciences and Medicine, E., 2017. Volcanic Eruptions and Their Repose, Unrest, Precursors, and Timing. The National Academies Press, Washington, DC. https://doi.org/10.17226/24650

Pallister, J.S., Hoblitt, R.P., Reyes, A.G., 1992. A basalt trigger for the 1991 eruptions of Pinatubo volcano? Nature 356, 426–428. https://doi.org/10.1038/356426a0

Pamukçu, A.S., Wright, K.A., Gualda, G.A.R., Gravley, D., 2020. Magma residence and eruption at the Taupo Volcanic Center (Taupo Volcanic Zone, New Zealand): insights from rhyolite-MELTS geobarometry, diffusion chronometry, and crystal textures. Contrib. to Mineral. Petrol. 175, 1–27. https://doi.org/10.1007/s00410-020-01684-2

Papale, P., 1999. Strain-induced magma fragmentation in explosive eruptions. Nature 397, 425–428. https://doi.org/10.1038/17109

Pichavant, M., Costa, F., Burgisser, A., Scaillet, B., Martel, C., Poussineau, S., 2007.

Equilibration scales in silicic to intermediate magmas - Implications for experimental studies. J. Petrol. 48, 1955–1972. https://doi.org/10.1093/petrology/egm045

Pineda, C., 2015. Geocronología U-Pb en circones de la Ignimbrita Pudahuel. Universidad de Chile, Santiago, p. 105. Geologist Professional Degree Thesis.

Pinkerton, H., Wilson, L., Macdonald, R., 2002. The transport and eruption of magma from volcanoes: A review. Contemp. Phys. 43, 197–210. https://doi.org/10.1080/00107510110097756

Polanski, J., 1963. Estratigrafía, neotectónica y geomorfología del Pleistoceno pedemontano entre los ríos Diamante y Mendoza: Provincia de Mendoza, Revista de la Asociación Geológica Argentina.

Ruprecht, P., Bergantz, G.W., Cooper, K.M., Hildreth, W., 2012. The crustal magma storage system of volcán quizapu, chile, and the effects of magma mixing on magma diversity. J. Petrol. 53, 801–840. https://doi.org/10.1093/petrology/egs002

Rutherford, M.J., 2008. Magma ascent rates. Rev. Mineral. Geochemistry 69, 241–271. https://doi.org/10.2138/rmg.2008.69.7

Rutherford, M.J., Devine, J.D., 2003. Magmatic conditions and magma ascent as indicated by hornblende phase equilibria and reactions in the 1995-2002 Soufrière Hills magma. J. Petrol. 44, 1433–1454. https://doi.org/10.1093/petrology/44.8.1433

Rutherford, M.J., Hill, P.M., 1993. Magma Ascent Rates From Amphibole Breakdown ' An Experimental Study Applied to the 1980-1986 Mount St . Helens Eruptions the rates processes phenocrysts of amphibole that were is becoming increasingly important in the fields of presence of melt at depth . 98.

Rutherford, M.J., Sigurdsson, H., Carey, S., Davis, A., 1985. The May 18, 1980, eruption of Mount St. Helens. 1. Melt composition and experimental phase equilibria. J. Geophys.

Res. 90, 2929–2947. https://doi.org/10.1029/JB090iB04p02929

Self, S., 2015. Explosive Super-Eruptions and Potential Global Impacts, Volcanic Hazards, Risks and Disasters. Elsevier Inc. https://doi.org/10.1016/B978-0-12-396453-3.00016-2

Sellés, D., Gana, P., 2001. Geología del área Talagante-San Francisco de Mostazal, Regiones Metropolitana de Santiago y del Libertador General Bernardo O'Higgins, Servicio Nacional de Geología y Minería, Carta Geológica de Chile, Serie Geología Básica 74, 1 mapa escala 1:100.000. Santiago.

SERNAGEOMIN, 2003. Mapa Geológico de Chile: versión digital, Servicio Nacional de Geología y Minería, Pubilicación Geológica Digital, Nº 4 (CD-ROM, versión 1.0). Santiago.

Singer, B.S., Le Mével, H., Licciardi, J.M., Córdova, L., Tikoff, B., Garibaldi, N., Andersen, N.L., Diefenbach, A.K., Feigl, K.L., 2018. Geomorphic expression of rapid Holocene silicic magma reservoir growth beneath Laguna del Maule, Chile. Sci. Adv. 4, 1–11. https://doi.org/10.1126/sciadv.aat1513

Sisson, T.W., Grove, T.L., 1993. Experimental investigations of the role of H2O in calc-alkaline differentiation and subduction zone magmatism. Contrib. to Mineral. Petrol. 113, 143–166. https://doi.org/10.1007/BF00283225

Sruoga, P., Etcheverria, M., Folguera, A., Repol, D., 2005a. Programa Nacional de Cartas Geológicas Hoja Geológica 3569-I Volcán Maipo, provincia de Mendoza. Buenos Aires.

Sruoga, P., Llambías, E.J., Fauqué, L., Schonwandt, D., Repol, D.G., 2005b. Volcanological and geochemical evolution of the Diamante Caldera-Maipo volcano complex in the southern Andes of Argentina (34°10′S). J. South Am. Earth Sci. 19, 399–414.

https://doi.org/10.1016/j.jsames.2005.06.003

Stern, C.R., Amini, H., Charrier, R., Godoy, E., Herve, F., Varela, J., 1984. Petrochemistry and age of rhyolitic pyroclastic flows which occur along the drainage valleys of the río Maipo and río Cachapoal (Chile) and the río Yaucha and río Papagayos (Argentina). Rev. Geológica Chile 23, 39–52.

Stern, C.R., Moreno, H., López-Escobar, L., Clavero, J.E., Lara, L.E., Naranjo, J.A., Parada, M.A., Skewes, M.A., 2007. Chilean volcanoes. Geol. Soc. Spec. Publ. 147–178. https://doi.org/10.1144/goch.5

Tramontano, S., Gualda, G.A.R., Ghiorso, M.S., 2017. Internal triggering of volcanic eruptions: tracking overpressure regimes for giant magma bodies. Earth Planet. Sci. Lett. 472, 142–151. https://doi.org/10.1016/j.epsl.2017.05.014

Troncoso, C., 2012. Estudio Estratigráfico y de volcanología física de la Ignimbrita Pudahuel. Universidad de Chile.

Venezky, D.Y., Rutherford, M.J., 1999. Petrology and Fe-Ti oxide reequilibration of the 1991 Mount Unzen mixed magma. J. Volcanol. Geotherm. Res. 89, 213–230. https://doi.org/10.1016/S0377-0273(98)00133-4

Wall, R., Gana, P., Gutiérrez, Á., 1996. Mapa Geológico Del Área De San Antonio-Melipilla, Regiones de Valparaíso, Metropolitana y del Libertador General Bernardo O'Higgins, in: Servicio Nacional de Geología y Minería, Mapa Geológico N^{o} 2, 1 Mapa Escala 1:100.000. Santiago.

Wall, R., Sellés, D., Gana, P., 1999. Area Tiltil-Santiago, Región Metropolitana, Servicio Nacional de Geología y Minería, Mapa Geológico N^{o} 11, 1 mapa escala 1:100.000. Santiago.

Wall, R.M., Lara, L.E., Perez de Arce, C., 2001. Upper pliocene-lower pleistocene $^{40}Ar/^{39}Ar$

ages of Pudahuel ignimbrite (Diamante-Maipo volcanic complex), Central Chile (33.5^0S).

Waters, L.E., Lange, R.A., 2015. An updated calibration of the plagioclase-liquid hygrometer-thermometer applicable to basalts through rhyolites. Am. Mineral. 100, 2172–2184. https://doi.org/10.2138/am-2015-5232

Wilson, Lionel, Stephen, R., Sparks, J., Walker, George P L, Wilson, L, Sparks, R.S.J., Walker, G P L, 1980. Explosive volcanic eruptions — IV. The control of magma properties and conduit geometry on eruption column behaviour, Geophys. J. R. astr. Soc. https://doi.org/10.1111/j.1365-246X.1980.tb02613.x

Zhang, Y., Xu, Z., Zhu, M., Wang, H., 2007. Silicate melt properties and volcanic eruptions. Rev. Geophys. 45, 1–27. https://doi.org/10.1029/2006RG000216

Chapter 5. Melt inclusion analyses.

1. Methods

Twenty-four thin sections from pumices of the PDC and from the pumice-rich fall deposit were petrologically described to look for minerals that host MI (Fig. 1-2). Plagioclase, the most abundant phenocryst, has the most and better-looking MI so was pick for this study. We select eight representative samples: six from a column were the plinian fall deposit was expose in the Argentinian side of the caldera, and two from the Chilean side, one of each valley where outcrops of the ignimbrite are present (circles symbols in Fig. 1).

Pumices samples were gently crushed, and individual phenocrysts were hand-picked using stereo microscope. Around 10-20 crystals per sample of a size between 0.4 and 2.5 mm, were mounted individually in epoxy and polished until expose the MI, which were described considering parameters as size, bubble and crystals presence, location in the phenocryst, among others. For volatiles and major elements analyses, only homogeneous and bubble-bearing MI were used as their composition is the least modified by post-entrapment processes. MI bigger than 15 µm were selected to determinate major element composition in an electron microprobe (EMP). MI with a diameter bigger than 30 µm were also selected for volatile content analyses in secondary ion mass spectrometric (SIMS) and were pressed into indium in order to prevent H-C contamination.

Volatile elements (O, H, C, S, F, Cl) were measured using a Cameca IMS 7f-Geo SIMS in the Washington University in St. Louis (USA). Major and minor element composition of glasses and major element composition for plagioclase were determinate using a JEOL JXA 8230 SuperProbe electron microprobe (EMP) at the Stanford University (USA). Major elements analyses in glass were conducted using an accelerating voltage 15 keV, a beam current of 5 nA and a spot size of 5 µm of diameter. For minor elements in glass the accelerating voltage was 15 keV, the beam current was 50 nA, and the spot size was 5 µm of diameter. For major elements analyses in plagioclase the accelerating voltage used was of 15 keV, the bean current 20 nA and the spot size of 1 µm of diameter.

2. Results

Petrography of melt inclusions

Melt inclusions were found in plagioclase and biotite phenocrysts, however the ones in biotite were too small (<10 µm) for analysed and, as is not an abundant phenocryst (~0.5%), MI hosted in it were not considered for this study. In the other hand, most of the plagioclase crystals that were examined contain MI and they usually have a diameter between 30 and 10 µm. There are two different plagioclase groups in the Pudahuel Ignimbrite: group 1 of unzoned phenocrysts with compositions of An_{20-17} and group 2 of normally zoned phenocryst from An_{48-40} in the core to An_{20-17} in the rims (Pineda et al., 2021), and they are found in all samples collected. MI were identified in these two groups and almost all phenocrysts contain more than one, however they hardly ever were in the same plane so the most homogeneous and biggest was select for analyses. MI are usually glassy with one or more bubbles (Table 1), or entirely glassy, with no evidence of recrystallization and bubble-free. Several MI show some grade of recrystallization and some of them present apatite as a daughter mineral. Bubble volumes in bubble-bearing MI range from 0.5-40%. Some MI showed evidence of decrepitation, those were not analysed as they composition was probably altered. Only regularly shaped MI were used for this study.

Major element compositions

Major elements compositions of MI are shown in Harker diagrams along with pumice matrix compositions (Fig. 3). MI are divided according to the composition of the plagioclase zone where they were trapped. Considering the composition range from zoned plagioclase, crystals were divided in core $>An_{32}$, middle An_{32-24} and rim $<An_{24}$; MI that are host in homogeneous plagioclase (An_{20-17}) are also considerate in the last group.

Silica composition of MI shows a small variation: from 67 to 75 wt.% SiO_2 approximately. The ones with higher SiO_2 values are overlapping with pumice glass compositions (70 - 75 wt.% SiO_2) and are mainly from the rim group. Other major elements in MI as Al_2O, K_2O and CaO, show not marked variation, and their average values matches with the glass pumice composition, however there are some isolated points that are above the mean composition as in the case of K_2O or below as in the case of Al_2O_3, which are mainly the ones trapped in more sodic plagioclase. MI shows a depletion of Na_2O relative to the pumice glass

composition at intermediate SiO_2 contents (66 - 70 wt.% SiO_2). MI trapped in the middle and core of plagioclase present a slightly higher concentration of MgO, TiO_2 and FeO than the ones trapped in plagioclase rims or in homogeneous plagioclase, and present higher values than the glass pumices.

Volatiles

Volatile content of MI shows no correlation with SiO_2 (Fig. 4), F content for MI hosted in rims or homogeneous plagioclase range from ~200 - 400 ppm, and contents for the ones hosted in middle composition plagioclase show contents <100 ppm; P content for MI host in rims or homogeneous plagioclase compositions range between ~60 and ~80 ppm, and S range from ~20 - 40 ppm, MI hosted in plagioclase cores show higher volatile contents that the rest of the inclusions.

Water content for MI hosted in rims or homogeneous plagioclase varies approximately between 3 and 5 wt.% H_2O, meanwhile the ones trapped in the middle zones show lower contents (1 and 3.3 wt.% H_2O). The only analysis for a MI trapped in a core is of 4.8 wt.% H_2O with an anomalously high content of CO_2 (Table 2, Fig. 4).

Isobars were calculated with the program *VolatileCalc* (Newman and Lowenstern, 2002), using a pre-eruptive temperature of 720ºC (Pineda et al., 2021). Pressure values range from less than 100 MPa to 200 MPa (Fig. 5), being the MI trapped in the middle part of the plagioclases the ones that present the lowest values. The MI trapped in a core of the plagioclase present a CO_2 value almost four times higher than the other MI analyzed, so is out of the range application of the method and is not possible to calculate a pressure value.

Table 4: Melt inclusion petrography.

Sample	Size (μm)	Shape	MI Bubbles	MI vol (μm³)	Bubble 1 vol (μm³)	Bubble 2 vol (μm³)	Bubble 3 vol (μm³)	Bubble 4 vol (μm³)	Total bubble vol	Bubble percent volume (%)	notes
DAC9.S.P3.MI1	45 x 40	trapezoidal	0	37699							
DAC9.S.P4.MI1	74.9 x 38.2	ellipsoidal	0	57228							
DAC9.S.P5.MI1	85.2 x 44.8	ellipsoidal	3	89535	1150	796	195		2142	2.4	
DAC11.S.P1.MI1	53.6 x 46	rectangular	1	59385	6206				6206	10.5	crystal
DAC11.S.P3.MI1	31 x 35	rectangular	1	19884	206				206	1.0	possible crystalization
DAC11.S.P4.MI1	48.6 x 30	ellipsoidal	1	22902	187				187	0.8	
DAC11.S.P5.MI1	78.6 x 64.3	rectangular	1	170154	1531				1531	0.9	possible crystalization
DAC11.S.P6.MI1	48 x 30	ellipsoidal	0	22620							
DAC11.S.P7.MI1	66.4 x 42.9	rectangular	0	63986							possible crystalization
DAC11.S.P8.MI1	76.4 x 45	trapezoidal	2	81006	204	204			407	0.5	possible crystalization
DAC11.S.P8.MI2	47.6 x 36.2	ellipsoidal	0	32661							
DAC13.S.P1.MI1	98.6 x 31.4	ellipsoidal	3	50902	5655	524	333		6512	12.8	
CPIP02.S.P1.MI1	47.1 x 42.9	ellipsoidal	3	45387	187	97	42		326	0.7	
CPIP02.S.P2.MI1	45.7 x 34.3	trapezoidal	0	28152							
CPIP02.S.P3.MI1	34.3 x 26.8	rectangular	0	12899							
CPIP02.S.P4.MI1	45.8 x 25	rectangular	1	14988	3105				3105	20.7	
CPIP02.S.P7.MI1	48.6 x 30	rectangular	3	22902	524	524	333		1380	6.0	
CPIP02.S.P8.MI1	36.5 x 29.2	rectangular	4	16295	74	16	156	5	250	1.5	
CPIP10.S.P1.MI1	50 x 37	trapezoidal	0	35840							
DAC9.S.P1.MI1a	90.9 x 80	trapezoidal	3	304609	3157	1596	395		5147	1.7	
DAC9.S.P1.MI2a	75.6 x 70.7	trapezoidal	1	197861	1839				1839	0.9	possible crystalization
DAC9.S.P2.MI1	36 x 40	rectangular	1	30159	524				524	1.7	

DAC12.S.P1.MI1	85.7 x 48.6	ellipsoidal	0	105987						
DAC9.M.P1.MI1	29.7 x 17.1	ellipsoidal	0	4547						
DAC9.M.P1.MI2	25.3 x 20.3	rectangular	2	5459	345	102		447	8.2	
DAC9.M.P2.MI1	27.6 x 18.8	ellipsoidal	0	5108						
DAC9.M.P3.MI1	43.5 x 21.2	rectangular	1	10237	2855			2855	27.9	
DAC9.M.P4.MI1	36 x 20.3	ellipsoidal	1	7768	221			221	2.8	
DAC9.M.P5.MI1	17.9 x 12.3	ellipsoidal	0	1418						
DAC9.M.P7.MI1	45.8 x 20.7	ellipsoidal	1	10276	697			697	6.8	
DAC9.M.P7.MI2	37.5 x 18	amorphous	2	6362	274	48		321	5.1	
DAC9.M.P8.MI1	25.1 x 16.8	ellipsoidal	0	3709						
DAC9.M.P9.MI1	28.1 x 18.6	ellipsoidal	0	5090						
DAC9.M.P11.MI1	41.6 x 16.8	ellipsoidal	0	6148						
DAC9.M.P13.MI1	35.4 x 26.3	ellipsoidal	0	12821						
DAC9.M.P14.MI1	34.3 x 20	ellipsoidal	0	7184						
DAC9.M.P14.MI2	25.7 x 17	ellipsoidal	0	3889						
DAC9.M.P16.MI1	14.3 x 12	ellipsoidal	0	1078						
DAC9.M.P17.MI2	20.6 x 15.3	ellipsoidal	1	2525	144			144	5.7	
DAC9.M.P17.MI3	47.1 x 30.6	trapezoidal	1	23092	2572			2572	11.1	
DAC9.M.P17.MI4	48 x 32	rounded ellipsoidal	1	25736	2145			2145	8.3	cracks
DAC9.M.P18.MI1	16 x 8.8	ellipsoidal	0	649						
DAC9.M.P19.MI1b	28.2 x 27.1	rectangular	1	10844	108			108	1.0	
DAC9.M.P19.MI2	18.2 x 12.4	rectangular	0	1465						
DAC9.M.P19.MI3	19 x 13.2	trapezoidal	0	1733						
DAC10.M.P1.MI1	61.5 x 46.2	ellipsoidal	3	68732	6454	974	82	7512	10.9	
DAC11.M.P1.MI1	58.5 x 21.4	ellipsoidal	1	14028	2711			2711	19.3	
DAC11.M.P2.MI1	50 x 26.7	trapezoidal	1	18663	716			716	3.8	
DAC11.M.P2.MI2	50 x 27.5	trapezoidal	0	19799						

DAC11.M.P2.MI4	72.2 x 24.4	trapezoidal	0								
DAC11.M.P4.MI1	21.2 x 11.8	rectangular	0	1546							
DAC11.M.P7.MI1	25.8 x 20.8	ellipsoidal	0	5845							
DAC11.M.P9.MI1	33.2 x 18.4	rectangular	0	5885							
DAC11.M.P10.MI1	26.7 x 18.7	trapezoidal	0	4889							
DAC11.M.P10.MI2	26.7 x 17.3	trapezoidal	0	4184							
DAC12.M.P4.MI3	66.7 x 22.2	rectangular	3	17212	1302	1232	92		2625	15.3	
DAC12.M.P7.MI1	68.5 x 38.6	ellipsoidal	1	53440	2904				2904	5.4	
DAC12.M.P9.MI1	26.7 x 16.7	ellipsoidal	2	3899	34	19			52	1.3	
DAC12.M.P9.MI2	18.7 x 13.3	ellipsoidal	2	1732	54	10			65	3.7	
DAC13.M.P2.MI1	63.3 x 33.3	trapezoidal	2	36753	3678	3877			7554	20.6	
DAC13.M.P2.MI2	36.1 x 20	ellipsoidal	1	7561	897				897	11.9	
DAC13.M.P2.MI3	47.2 x 22.8	ellipsoidal	0	12847							
DAC13.M.P3.MI1a	71.8 x 21.2	rectangular	1	16896	3350				3350	19.8	
DAC13.M.P4.MI1	64.3 x 38.6	ellipsoidal	2	50163	6858	63			6920	13.8	crystal?
DAC13.M.P8.MI1	48.4 x 24	rectangular	1	14597	5500				5500	37.7	
DAC13.M.P10.MI2	58.9 x 31.2	rectangular	2	30021	2065	212			2277	7.6	
DAC13.M.P10.MI3	69.5 x 31.6	trapezoidal	4	36338	1788	1222	131	131	3272	9.0	
DAC 9.T.P1.MI1a											
DAC 9.T.P1.MI1b											
DAC 9.T.P1.MI2a											
DAC 9.T.P1.MI2b											
DAC 9.T.P2.MI1	30 x 18	trapezoidal	0	5089							

Table 5: Melt inclusion and plagioclase host compositions. Major elements determined by EMPA and volatiles determined by SIMS.

Sample	K_2O	CaO	SiO_2	Al_2O_3	Na_2O	MgO	FeO	MnO	BaO	TiO_2	Cl	SO_3	Total	H_2O	CO_2	F	P	S	Total with H_2O	Plg host composition		
	wt%	wt%	wt%	wt%	wt%	wt%	wt%	wt%	wt%	wt%	wt%	wt%		wt%	ppm	ppm	ppm	ppm		An	Ab	Or
DAC9.S.P3.MI1	4.0	0.50	67.88	12.29	3.52	0.10	0.53	0.07	0.07	0.08	0.13	0.01	89.2							19.0	75.7	5.3
DAC9.S.P5.MI1	3.9	0.50	72.57	12.50	3.40	0.09	0.54	0.05	0.12	0.09	0.13	0.01	93.9	4.9	127.9	308	94	34	98.8	19.2	75.7	5.2
DAC11.S.P1.MI1	3.9	0.50	67.56	12.51	2.90	0.13	0.86	0.09	0.04	0.11	0.21	0.02	88.8							32.4	64.7	2.9
DAC11.S.P4.MI1	3.9	0.48	68.23	12.01	3.03	0.07	0.50	0.06	0.07	0.07	0.14	0.02	88.6	4.2	760.6	266	73	32	92.7	18.9	75.5	5.6
DAC11.S.P5.MI1	4.1	0.73	67.16	11.73	4.06	0.09	0.57	0.06	0.01	0.06	0.13	0.02	88.7	4.4	259.5	307	85	30	93.1	19.6	75.1	5.3
DAC11.S.P6.MI1	4.0	0.46	66.66	11.92	3.28	0.11	0.56	0.07	0.01	0.07	0.16	0.03	87.3	4.8	4077.6	432	108	50	92.1	32.9	64.4	2.7
DAC11.S.P8.MI1	3.9	0.49	68.11	11.70	3.07	0.08	0.44	0.06	0.08	0.06	0.12	0.03	88.2	4.5	384.2	295	88	30	92.7	18.3	76.2	5.5
DAC11.S.P8.MI2	3.9	0.47	71.42	12.46	3.27	0.11	0.48	0.06	0.07	0.08	0.13	0.00	92.4							18.3	76.2	5.5
DAC13.S.P1.MI1	4.7	0.46	67.83	11.88	2.60	0.08	0.61	0.08	0.06	0.07	0.15	0.03	88.5	3.0	984.6	370	88	44	91.5	19.0	75.4	5.6
CPIP02.S.P1.MI1	6.2	0.44	67.08	11.61	2.11	0.07	0.46	0.05	0.08	0.06	0.13	0.01	88.3							18.6	75.9	5.4
CPIP02.S.P2.MI1	4.1	0.37	69.91	12.11	2.96	0.08	0.48	0.06	0.06	0.06	0.13	0.02	90.3	4.4	37.4	288	82	28	94.7	19.9	75.0	5.2
CPIP02.S.P4.MI1	4.5	0.57	68.50	13.22	2.98	0.15	0.87	0.10	0.06	0.10	0.23	0.02	91.3	1.0	674.8	106	45	9	92.3	30.6	66.3	3.0
CPIP02.S.P7.MI1	5.6	0.48	68.55	11.96	2.43	0.10	0.50	0.04	0.08	0.08	0.14	0.02	89.9							20.4	74.6	5.0
CPIP02.S.P8.MI1	5.6	0.41	67.21	11.39	1.72	0.09	0.45	0.06	0.11	0.07	0.13	0.02	87.2	4.4	356.4	246	68	20	91.6	19.1	75.8	5.2
CPIP10.S.P1.MI1	5.2	0.58	69.66	12.56	2.61	0.08	0.60	0.08	0.04	0.08	0.14	0.01	91.7	3.3	71.9	26	108	21	95.0	30.8	66.1	3.1
DAC9.S.P1.MI1a	4.2	0.41	71.47	12.61	3.58	0.08	0.52	0.07	0.08	0.09	0.11	0.00	93.2							18.9	75.9	5.3
DAC9.S.P1.MI1b	4.0	0.42	71.65	12.76	3.71	0.07	0.52	0.06	0.03	0.10	0.11	0.01	93.4							18.9	75.9	5.3
DAC9.S.P1.MI2a	3.6	0.49	67.87	12.30	2.70	0.09	0.60	0.07	0.06	0.09	0.14	0.02	88.1							18.9	75.9	5.3
DAC9.S.P1.MI2b	3.6	0.51	70.55	12.92	3.86	0.09	0.60	0.08	0.06	0.11	0.13	0.01	92.5							18.9	75.9	5.3
DAC9.S.P2.MI1	3.9	0.45	70.86	12.17	3.44	0.09	0.54	0.08	0.07	0.10	0.11	0.02	91.8							16.7	77.2	6.1
DAC12.S.P1.MI1	3.5	0.45	73.54	12.79	1.19	0.08	0.52	0.07	0.09	0.07	0.10	0.01	92.5							22.6	72.9	4.5
DAC9.M.P1.MI1	3.87	0.50	71.72	12.17	3.83	0.09	0.50	0.07	0.04	0.10	0.11	0.02	93.0							19.5	75.3	5.1
DAC9.M.P1.MI2	4.04	0.43	73.36	12.23	3.34	0.10	0.44	0.05	0.04	0.10	0.11	0.01	94.3							19.5	75.3	5.1

DAC9.M.P2.MI1	3.90	0.40	70.41	12.43	3.52	0.10	0.56	0.08	0.06	0.08	0.12	0.01	91.7	19.9	75.2	4.9
DAC9.M.P3.MI1	4.07	0.50	70.36	12.54	3.54	0.19	0.86	0.08	0.05	0.22	0.18	0.02	92.6	26.9	69.4	3.7
DAC9.M.P4.MI1	3.94	0.52	70.12	12.64	3.74	0.15	0.79	0.09	0.09	0.18	0.17	0.01	92.4	24.7	71.7	3.7
DAC9.M.P5.MI1	3.55	1.18	70.71	14.23	4.56	0.08	0.44	0.07	0.05	0.09	0.10	0.00	95.1	19.5	75.4	5.1
DAC9.M.P7.MI1	3.69	0.59	70.96	12.81	3.59	0.20	1.05	0.05	0.11	0.31	0.18	0.01	93.6	38.3	59.6	2.1
DAC9.M.P7.MI2	4.20	0.65	71.82	12.40	3.81	0.10	0.82	0.06	0.06	0.09	0.17	0.02	94.2	34.2	63.4	2.4
DAC9.M.P7.MI1b	3.35	0.59	70.34	12.50	2.29	0.18	1.11	0.07	0.11	0.31	0.18	0.01	91.0	38.3	59.6	2.1
DAC9.M.P8.MI1	4.11	0.35	72.00	12.44	3.41	0.09	0.53	0.07	0.06	0.09	0.10	0.01	93.3	17.3	77.0	5.8
DAC9.M.P9.MI1	3.62	0.50	71.68	11.96	3.32	0.10	0.49	0.06	0.04	0.09	0.10	0.01	92.0	19.1	75.8	5.2
DAC9.M.P11.MI1	3.78	0.52	71.03	12.43	3.37	0.09	0.47	0.06	0.06	0.09	0.11	0.02	92.0	18.7	76.0	5.3
DAC9.M.P13.MI1	4.61	0.25	71.02	12.32	3.84	0.08	0.50	0.06	0.02	0.08	0.11	0.01	92.9	19.3	75.6	5.1
DAC9.M.P14.MI1	3.75	0.55	71.59	12.51	3.45	0.08	0.49	0.07	0.04	0.09	0.10	0.01	92.7	19.7	75.1	5.2
DAC9.M.P14.MI2	3.90	0.46	71.51	12.03	3.28	0.09	0.50	0.08	0.05	0.10	0.10	0.01	92.1	19.7	75.1	5.2
DAC9.M.P16.MI1	2.43	2.50	66.38	18.12	6.08	0.10	0.52	0.06	0.09	0.09	0.10	0.00	96.5	17.7	76.6	5.7
DAC9.M.P17.MI2	4.16	0.67	69.39	12.92	3.74	0.16	0.82	0.08	0.07	0.20	0.18	0.02	92.4	29.3	67.6	3.1
DAC9.M.P17.MI3	3.78	0.57	70.59	12.76	3.82	0.17	0.87	0.09	0.07	0.22	0.17	0.01	93.1	29.3	67.6	3.1
DAC9.M.P17.MI4	3.54	0.45	69.37	12.81	4.10	0.17	0.84	0.08	0.07	0.21	0.18	0.01	91.8	29.3	67.6	3.1
DAC9.M.P18.MI1	3.42	0.48	70.82	12.08	3.43	0.09	0.53	0.07	0.07	0.09	0.11	0.01	91.2	17.7	76.4	5.8
DAC9.M.P19.MI1b	3.69	0.42	70.39	12.15	3.47	0.09	0.49	0.07	0.10	0.09	0.11	0.01	91.1	19.5	75.5	5.1
DAC9.M.P19.MI2	4.23	0.48	70.62	12.41	3.47	0.09	0.53	0.08	0.09	0.08	0.11	0.01	92.2	19.5	75.5	5.1
DAC9.M.P19.MI3	3.26	0.47	72.12	12.62	3.68	0.09	0.49	0.07	0.10	0.10	0.10	0.01	93.1	19.5	75.5	5.1
DAC10.M.P1.MI1	3.73	0.27	69.67	12.38	3.86	0.18	0.99	0.12	0.04	0.27	0.28	0.00	91.8	28.8	67.8	3.4
DAC11.M.P1.MI1	3.61	0.68	70.81	13.25	3.92	0.26	1.07	0.07	0.13	0.11	0.19	0.01	94.1	33.8	63.4	2.8
DAC11.M.P1.MI1b	4.14	0.48	70.76	13.18	4.20	0.27	1.11	0.08	0.02	0.10	0.19	0.01	94.6	33.8	63.4	2.8
DAC11.M.P2.MI1	3.34	0.81	68.27	13.25	3.97	0.26	1.03	0.08	0.04	0.15	0.17	0.02	91.4	38.8	59.0	2.1
DAC11.M.P2.MI4	3.83	0.55	73.12	12.57	3.40	0.13	0.48	0.05	0.04	0.17	0.12	0.01	94.5	34.0	63.4	2.6
DAC11.M.P4.MI1	2.71	2.19	67.28	16.80	5.31	0.11	0.72	0.09	0.07	0.10	0.15	0.01	95.5	19.3	75.6	5.1

DAC11.M.P7.MI1	4.10	0.46	70.98	12.28	3.62	0.09	0.50	0.07	0.03	0.09	0.11	0.01	92.3	20.0	75.0	4.9
DAC11.M.P9.MI1	4.03	0.34	71.44	12.21	3.60	0.10	0.51	0.08	0.07	0.09	0.11	0.01	92.6	20.7	74.4	4.9
DAC11.M.P10.MI1	3.75	0.40	71.51	12.51	3.38	0.09	0.48	0.05	0.07	0.09	0.10	0.01	92.4	20.0	74.9	5.1
DAC11.M.P10.MI2	4.15	0.29	71.29	12.27	3.69	0.08	0.42	0.06	0.10	0.08	0.09	0.01	92.5	20.0	74.9	5.1
DAC12.M.P4.MI3	4.25	0.54	72.08	12.47	3.95	0.09	0.60	0.06	0.07	0.08	0.12	0.00	94.3	19.9	75.1	5.0
DAC12.M.P7.MI1	3.52	0.36	74.40	12.74	3.75	0.09	0.54	0.07	0.07	0.10	0.10	0.00	95.8	18.8	76.0	5.2
DAC13.M.P2.MI1	4.30	0.51	74.49	12.36	3.43	0.10	0.61	0.07	0.04	0.09	0.10	0.01	96.1	20.8	74.6	4.6
DAC13.M.P2.MI2	4.81	0.50	73.53	12.30	2.95	0.09	0.62	0.07	0.08	0.10	0.10	0.01	95.2	20.8	74.6	4.6
DAC13.M.P2.MI3	4.09	0.50	75.31	12.87	2.91	0.10	0.62	0.06	0.08	0.10	0.11	0.01	96.8	20.8	74.6	4.6
DAC13.M.P2.MI3b	3.85	0.52	74.98	12.65	3.14	0.11	0.58	0.06	0.04	0.10	0.10	0.01	96.2	20.8	74.6	4.6
DAC13.M.P3.MI1a	5.14	0.73	74.83	13.99	3.58	0.12	0.85	0.09	0.05	0.18	0.17	0.01	99.7	35.0	62.4	2.6
DAC13.M.P3.MI1b	4.39	0.69	74.34	13.77	3.51	0.12	0.84	0.10	0.04	0.17	0.17	0.00	98.1	35.0	62.4	2.6
DAC13.M.P4.MI1	4.14	0.42	73.70	13.27	3.60	0.10	0.58	0.07	0.07	0.09	0.12	0.01	96.2	23.1	72.8	4.1
DAC13.M.P8.MI1	4.07	0.47	74.31	12.90	3.62	0.10	0.49	0.08	0.12	0.09	0.10	0.01	96.3	41.2	56.8	2.0
DAC13.M.P10.MI2	5.63	0.53	74.48	13.51	2.68	0.14	0.63	0.07	0.08	0.11	0.12	0.01	98.0	31.6	65.4	2.9
DAC13.M.P10.MI3	4.49	0.55	71.34	13.31	4.23	0.11	0.45	0.10	0.07	0.12	0.16	0.01	94.9	31.6	65.4	2.9
DAC 9.T.P1.MI1a	4.2	0.41	71.47	12.61	3.58	0.08	0.52	0.07	0.08	0.09	0.11	0.00	93.2			
DAC 9.T.P1.MI1b	4.0	0.42	71.65	12.76	3.71	0.07	0.52	0.06	0.03	0.10	0.11	0.01	93.4			
DAC 9.T.P1.MI2a	3.6	0.49	67.87	12.30	2.70	0.09	0.60	0.07	0.06	0.09	0.14	0.02	88.1			
DAC 9.T.P1.MI2b	3.6	0.51	70.55	12.92	3.86	0.09	0.60	0.08	0.06	0.11	0.13	0.01	92.5			
DAC 9.T.P2.MI1	3.9	0.45	70.86	12.17	3.44	0.09	0.54	0.08	0.07	0.10	0.11	0.02	91.8			
DAC 12.T.P1.MI1?	3.5	0.45	73.54	12.79	1.19	0.08	0.52	0.07	0.09	0.07	0.10	0.01	92.5			

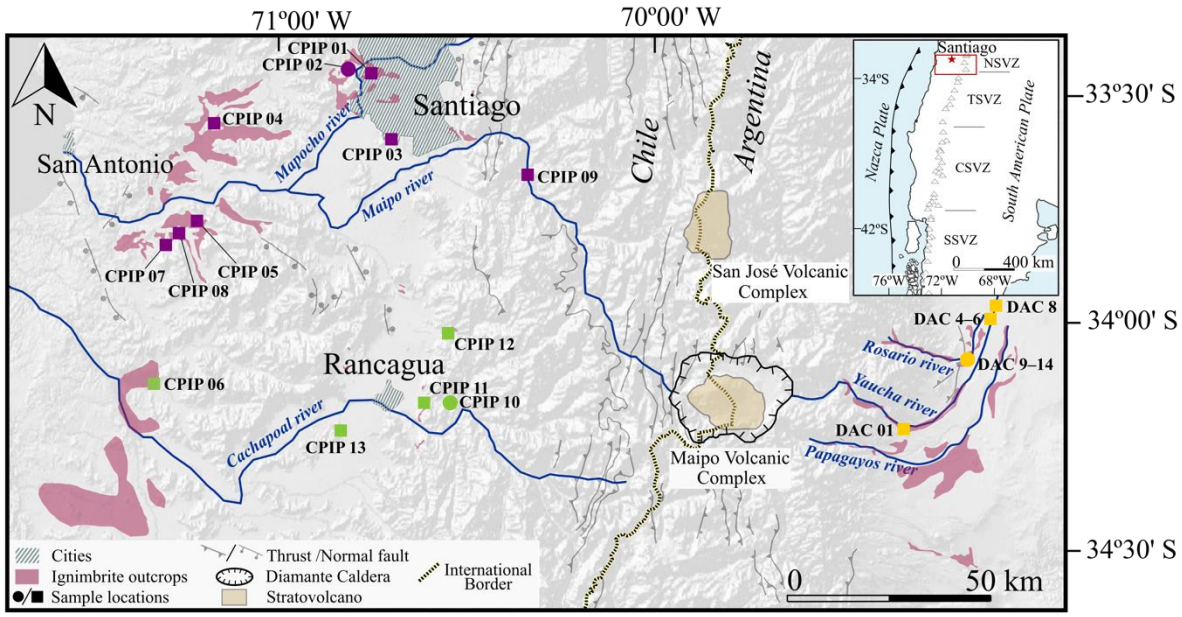

Figure 10:Regional location. Digital elevation model of Central Chile showing the outcrops of the Pudahuel Ignimbrite in pink; (data from Gana et al., 1996; Sellés and Gana, 2001; SERNAGEOMIN, 2003; Sruoga et al., 2005; Stern et al., 1984; Wall et al., 1999, 1996). Diamante caldera, Maipo volcano and cities are indicated. Locations of samples used in this study are shown: squares represent samples taken for MI chemical analyses (see text). Inset figure shows location and volcanoes of the South Volcanic Zone (SVZ) and its segments: northern, transition, central and southern volcanic zones (NSVZ, TSVZ, CSVZ and SSVZ respectively), modified from Stern et al., (2007).

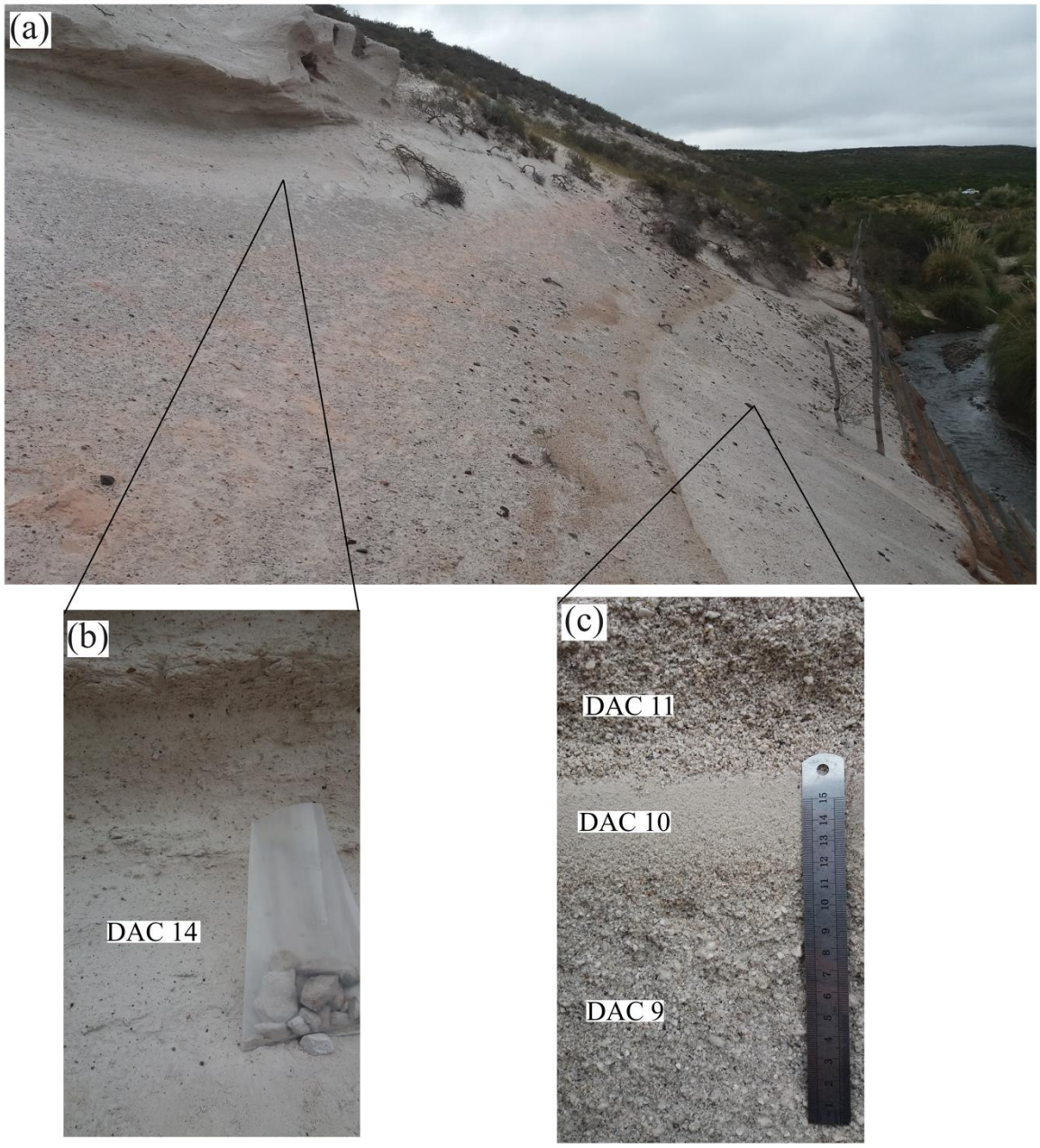

Figure 11: PDC and fallout deposits. a) outcrop in Yaucha valley, Argentina; b) detail of the PDC; c) detail of fall deposit units.

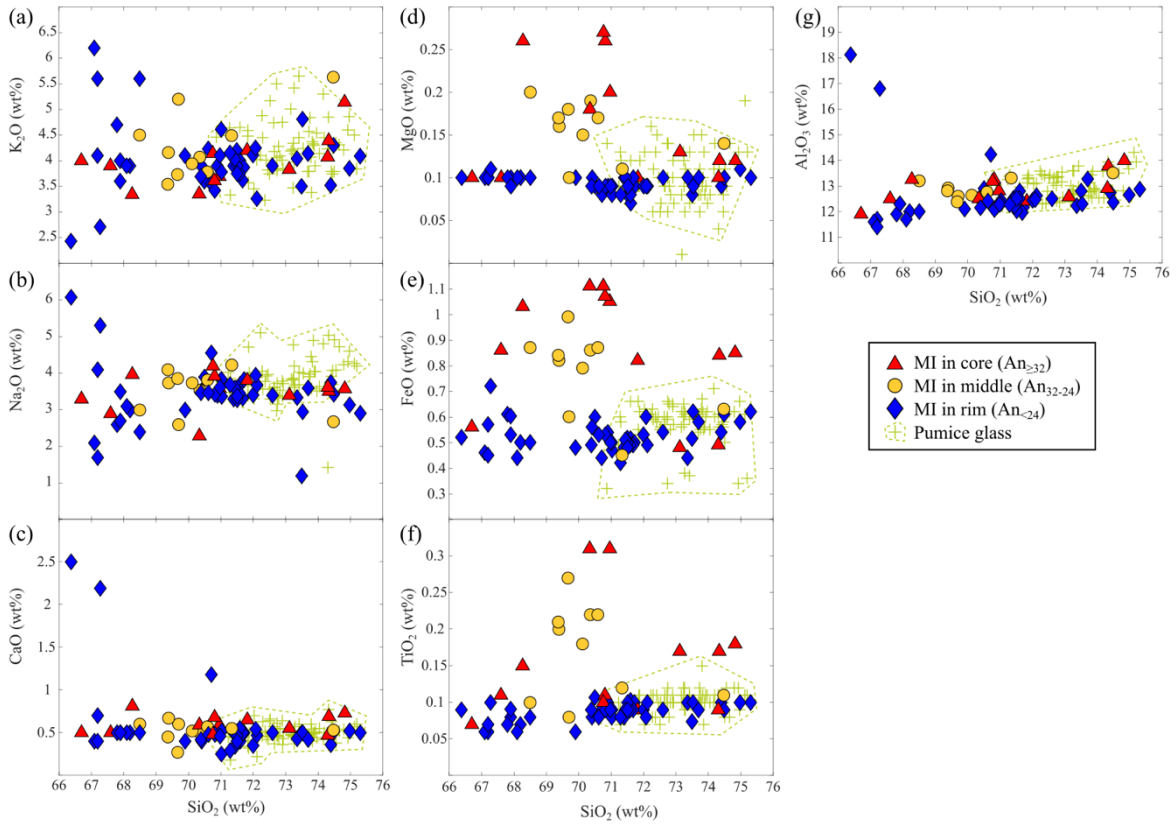

Figure 12: Harker diagrams for MI. Pumice glass composition is shown. a) K_2O; b) Na_2O; c) CaO; d) MgO; e) FeO; f) TiO_2; g) Al_2O_3.

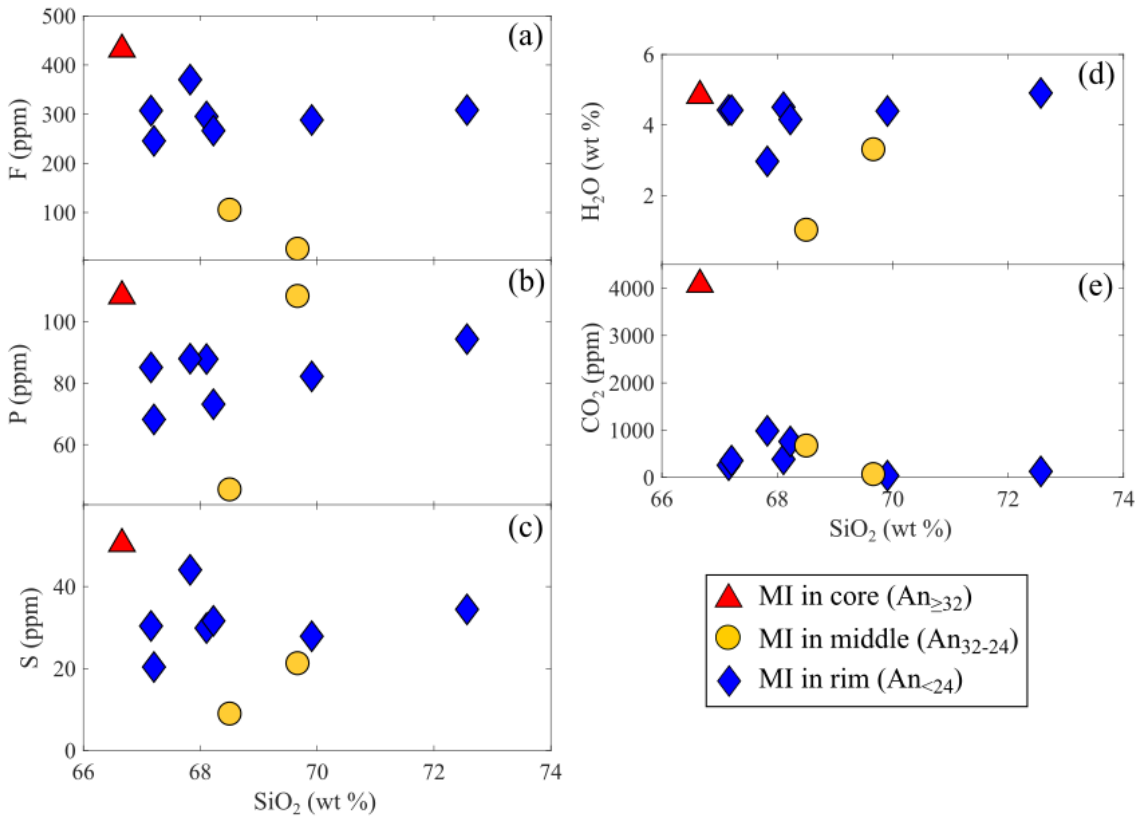

Figure 13: Volatile concentration in MI. a) F versus SiO_2; b) P versus SiO_2; c) S versus SiO_2; d) H_2O versus SiO_2; e) CO_2 versus SiO_2.

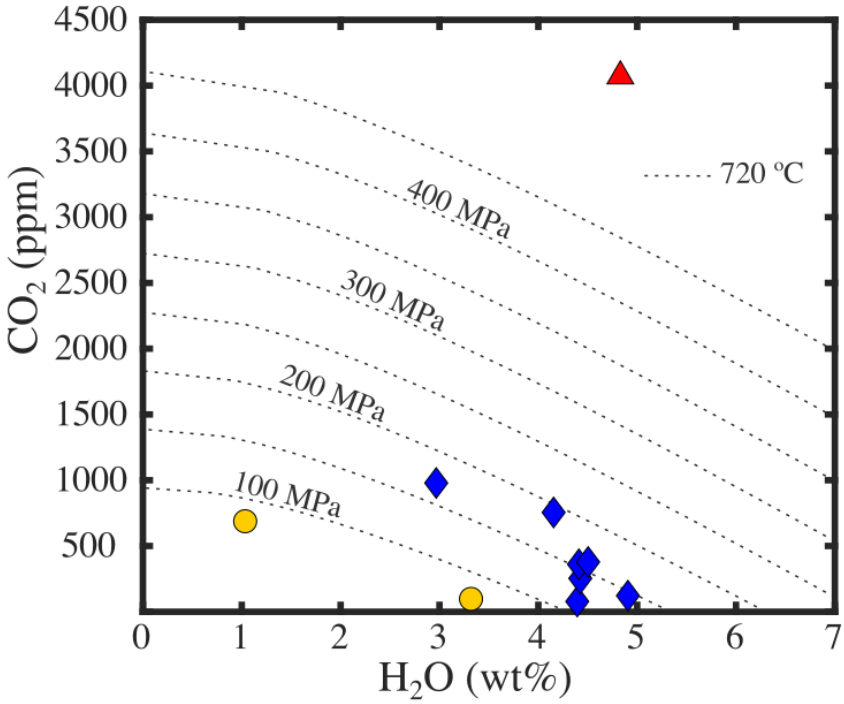

Figure 14: Isobaric lines calculated using the VolatileCalc solubility model (Newman and Lowenstern, 2002).

Chapter 6. Synthesis and conclusions.

Pudahuel Ignimbrite is an apparently young and volumetric rhyolite deposit associated to the Diamante caldera, where the active Maipo volcano is located. Its closeness to big cities makes the thorough characterization of factors such as age, pre-eruptive conditions and magmatic processes related to the magma that generated it, of utmost importance to really assess the potential hazard of this complex.

1. Storage Age

One of the main concerns is the eruption age, as different estimations of it have been considered and there is a significant variation between them (from 0.13 ± 0.03 Ma to 2.3 ± 0.3 Ma; Pineda, 2015; Wall et al., 2001, respectively). For a long time, this eruption age has been considered of ~ 450 ka, which implies a ~360 ka of steadiness for the volcanic system before the Maipo volcano started to develop ~89 ka ago. This gap, along with no evidence of subsequent deposits over the ignimbrite and a general lack of evidence that show rework, insinuates that the eruption age should be younger. Subsequent geochronological works suggested younger and more suitable ages of *ca.* 130 – 150 ka, however, lack of uncertainties (Lara et al., 2008) and the use of a less reliable method to date young eruptions (Pineda, 2015), made necessary an unequivocal and definitive estimation of the age. New U–Th ages in zircons separated from the ignimbrite pumices indicate a more likely eruption age of 167 ± 8 ka (Fig. 1 a–c). This value is closer to the oldest age determined for the Maipo volcano which is of 86 ± 10 ka (Sruoga et al., 2005) and denotes a ~70 ka gap between the change of the eruption style in the complex.

Zircons chemical signature indicate that the presence of other accessory minerals that incorporates REE, Th and U to its structures can affect the U–Th activity ratios in zircons affecting the age estimation with the U–Th method. Particularly, monazite incorporates Th over U decreasing the U–Th ratio in zircons growing along with it. This behavior can be identified not only between different crystals, but also along a single mineral analysis, and its consideration conveys to calculations of relatively younger ages. This is particularly important in the study of young eruptions, where couple of thousands of years can affect the

interpretation of determining processes, which in turn can affect the hazard awareness of the system.

2. Pre-eruptive conditions

On the other hand, a complete characterization of the conditions that generated this caldera forming eruption is necessary, not only to determine possible associated hazards to the complex, but also to improve our understanding of this catastrophic events. The pre-eruptive conditions of the Pudahuel Ignimbrite were determined through analytical and experimental approaches. The Fe–Ti oxide geothermometer (Ghiorso and Evans, 2008) and the plagioclase hygrometer (Waters and Lange, 2015) were combined to determine the temperature–X^{fl}_{H2O} conditions where glass, felspar and Fe–Ti oxides were in equilibrium. This results were combined with the composition–dependent water solubility model of Zhang, (2010) applied to a pumice composition. This approach indicates pre-eruptive temperatures of 717 ± 7 ºC, P_{H2O} of 200–360 MPa and a water content between 6.9 and 7.6 wt. % (Fig. 1 c–d). The same methodology was applied considering hotter temperatures, taking into account that Fe–Ti oxides temperatures could be a minimum as the Fe–Ti exchange equilibrium is restored quickly when there is changes in temperature and/or fO_2 (Hammond and Taylor, 1982; Venezky and Rutherford, 1999). This results in a larger range of P–T–H_2O conditions that allowed to form the glass and plagioclase compositions of the pumices. Phase equilibrium experiments were performed on a representative pumice sample at the range of resulting conditions, considering both H_2O-vapor saturated and undersaturated states. The best reproduction of major natural phase assemblage and its compositions was achieved by the experiments that were performed at low temperatures (700 – 750 ºC) and high P_{Total} (>200 MPa, more likely 300–350 Mpa), with water contents of at least 6 wt. %, which is consistent with the mineralogical approach. The results of the undersaturated experiments shows close matching between plagioclase and glass experimental compositions with the natural ones and suggest that the melt was not necessarily H_2O-saturated. Melt inclusions hosted in plagioclase rims indicate entrapment pressures between 100 – 200 MPa for a temperature of 720 ºC, which are ~ 4 – 8 km depth, considering a crustal density of 2,700 kg/m^3 (Anderson, 1989). Although the upper limit is consistent with the lower limit of total pressures obtained from experiments, these values indicate lower depth crystallization for the most sodic plagioclase at same temperatures. However, most of these MI present bubbles, which can

contain part of the volatiles of the melt that were trapped during plagioclase crystallization, and therefore these values need to be considered as a minimum.

Experimental results indicate depths of over 10 km (11–13 km), which is high when compared with those most commonly considered for caldera forming eruptions (< 5 km, e.g., Coombs and Gardner, 2002; Larsen, 2006). Still, evidence has been found of deeper magma accumulation (Chesner, 1998; Johnson and Rutherford, 1989; Masturyono et al., 2001; Pamukçu et al., 2020). Obtained depths correlates well with the regional structural setting, as the Diamante caldera zone is located over major crustal structures at 10 km depth (Farías et al., 2010), which could promote magma accumulation at such deep levels considering that pre-existing structures favor magma chamber growth and evolution (Hughes and Mahood, 2011).

3. Magmatic processes and eruption triggers

These high pressures difficult a caldera forming eruption and pose a problem in the identification of possible eruption triggers. Second boiling, a commonly invoked mechanism (Caricchi et al., 2014; Cashman and Scheu, 2015), is not that relevant in deep reservoirs since it requires proportionally higher extents of crystallization. This is unlikely for a crystal-poor rhyolite with no evidence of a crystal rich counterpart. Furthermore, to consider this process as viable, the Pudahuel rhyolite would have had to efficiently separate from a mush shortly before the eruption. However, the interaction of carbonic fluids with H_2O-rich magmas can increase magma overpressure by increasing volume and crystallization due to the reduction of the dissolved H_2O weight fraction (Blundy et al., 2010; Blundy and Cashman, 2008). A flux of CO_2 injected into a reservoir with eruptible magma (i.e., <50% vol.% crystals; Marsh, 1981), if large enough, could destabilize the system and lead it to eruption (Caricchi et al., 2018). Melt inclusions show relatively high CO_2 contents when compared to silicic arc magmas (Wallace, 2005), and apparently there is a correlation between the increase of CO_2 content and the decrease of H_2O content. This suggests that a rapid CO_2 flushing could be a potential trigger for the Pudahuel eruption, still, the amount of MI suitable for volatile measurements are not enough to strongly determine this correlation and more analyses would be needed to properly consider this mechanism.

In reservoirs as deep as this one, a caldera forming eruption could also be triggered by an external factor (Allan et al., 2012; Gregg et al., 2012; Pallister et al., 1992). In the area where

the Diamante caldera is located, a regional uplift of between 2 and 1.5 km occurred, which subsequently denuded at a high rate (Farías et al., 2008). Muñoz-Gómez et al., (2019) proposed that this intense denudation took place between 1.1 and 0.1 Ma and suggested that it drove a crustal melting process that generated many silicic magmas in the region, including the Pudahuel Ignimbrite. They proposed that eventually, these reservoirs developed an overpressure intrinsically when the system achieved saturation of a fluid phase. However, numerical models that support this theory assume pressures inconsistent with the results presented here, and a modeling considering higher pressures are necessary to determine whether denudation could affect the reservoir.

Deglaciation can also change the pressure at upper crustal levels (< 10 km depth) at a scale of hundreds of years, which could provoke a failure in the rock, as well as dike propagation in and out of a reservoir, making it collapse and leading to an explosive eruption (Mora and Tassara, 2019). Considering that the penultimate Chilean Andean glacial maximum has been recorded between 170-130 ka (Clapperton, 1983; Rabassa and Clapperton, 1990), and that major deglaciations proceed rapidly (< 15 ka) (Singer et al., 1997), the possibility that this process could trigger the eruption is a hypothesis worthy of investigation.

4. Potential Hazard

The study of the Pudahuel Ignimbrite has an enormous importance in the assessment of the risk associated to the Maipo volcanic complex, especially considering that caldera-forming eruptions represent one of the most catastrophic geologic events on Earth (Gottsmann and Martí, 2008). This is reinforced by the presence of an active volcano in the caldera and that future caldera-forming eruptions can be expected to take place at sites of existing calderas (Lipman, 2000). The Maipo volcano has been characterized for generating less evolved eruptions than the Pudahuel ignimbrite (54 –68 wt% SiO_2), with alternation of effusive and explosive events, and the historical ones characterized by small volume strombolian explosions of andesitic compositions (Sruoga et al., 2012). Estimations of the pre-eruptive conditions for one of the postglacial events (<14 ka), done through different mineral approaches, indicate temperatures between ~860 –1010 ºC, pressures of ~200 –340 MPa (~7.6 –12.8 km depth) and water contents of 3.6–5.2 wt. % (Sruoga et al., 2012). These depths are quite similar to the ones estimated for the Pudahuel reservoir, which could be related to the structural setting of the area (Fig. 1f). The small volumes, high temperatures, and less

evolved compositions of the Maipo products are not comparable with the characteristics of a caldera forming eruption, however, there are plenty of super volcanoes that have produced more than one great eruption, but also much smaller eruptions (e.g., Yellowstone, Long Valley, Taupo, among others), which will depend on the rate of magma production (Self, 2015). The cycling generation of more differentiated dacitic events in the Maipo volcano and the evidence of reservoirs at similar depth, implicate that they can grow in this area and that magma can evolve. External triggers, as the ones discussed previously, could disturb the reservoir and, if the rheologic conditions of the melt are like the ones of the Pudahuel rhyolite and enough magma volume has accumulated, an eruption of catastrophic characteristics could be generated. Further mineralogical analysis would allow better constraints of the possible triggers of the eruption, which along with geophysical monitoring of the area, could contribute to dilucidate the real hazard of the Maipo volcanic complex.

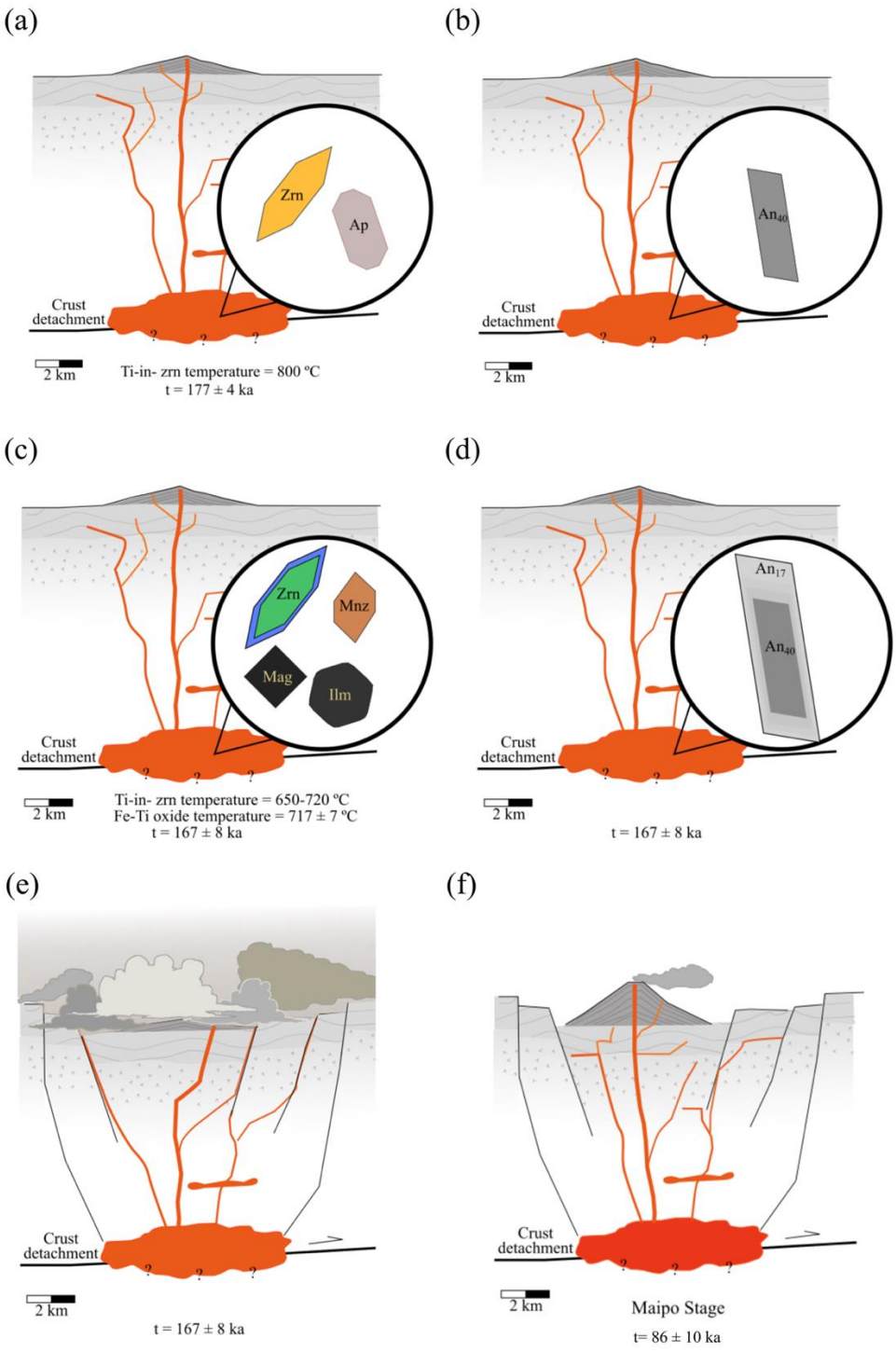

Figure 1: Schematic interpretation of the Maipo volcanic complex evolution, (a) accessory minerals such as zrn and ap indicate reservoir temperatures of 800 ºC and ages of 177 ± 4 ka, (b) growth of major phases, particularly less evolved pl, (c–d) accessory minerals such as zrn, mnz, mag and ilm, combined with major phase composition (pl and glass), indicate a reservoir of low temperatures and relatively high pressures, (e) zrn and mnz indicate a maximum eruption age of 167 ± 8 ka, (f) development of the Maipo stage.

5. Referencias

Allan, A.S.R., Wilson, C.J.N., Millet, M.A., Wysoczanski, R.J., 2012. The invisible hand: Tectonic triggering and modulation of a rhyolitic supereruption. Geology 40, 563–566. https://doi.org/10.1130/G32969.1

Anderson, D.L., 1989. Theory of the Earth. Blackwell Scientific Publications.

Blundy, J., Cashman, K., 2008. Petrologic reconstruction of magmatic system variables and processes. Rev. Mineral. Geochemistry 69, 179–239. https://doi.org/10.2138/rmg.2008.69.6

Blundy, J., Cashman, K. V., Rust, A., Witham, F., 2010. A case for CO2-rich arc magmas. Earth Planet. Sci. Lett. 290, 289–301. https://doi.org/10.1016/j.epsl.2009.12.013

Caricchi, L., Annen, C., Blundy, J., Simpson, G., Pinel, V., 2014. Frequency and magnitude of volcanic eruptions controlled by magma injection and buoyancy. Nat. Geosci. 7, 126–130. https://doi.org/10.1038/ngeo2041

Caricchi, L., Sheldrake, T.E., Blundy, J., 2018. Modulation of magmatic processes by CO2 flushing. Earth Planet. Sci. Lett. 491, 160–171. https://doi.org/10.1016/j.epsl.2018.03.042

Cashman, K. V, Scheu, B., 2015. Magmatic fragmentation. Encycl. Volcanoes 459–471.

Chesner, C.A., 1998. Petrogenesis of the Toba Tuffs, Sumatra, Indonesia. J. Petrol. 39, 397–438. https://doi.org/10.1093/petroj/39.3.397

Clapperton, C.M., 1983. The glaciation of the Andes. Quat. Sci. Rev. 2, 83–155. https://doi.org/10.1016/0277-3791(83)90005-7

Coombs, M.L., Gardner, J.E., 2002. Shallow-storage conditions for the rhyolite of the 1912 eruption at Novarupta, Alaska. Geology 29, 775–778. https://doi.org/10.1130/0091-7613(2001)029<0775:SSCFTR>2.0.CO;2

Farías, M., Charrier, R., Carretier, S., Martinod, J., Fock, A., Campbell, D., Cáceres, J.,

Comte, D., 2008. Late Miocene high and rapid surface uplift and its erosional response in the Andes of central Chile (33° - 35°S). Tectonics 27. https://doi.org/10.1029/2006TC002046

Farías, M., Comte, D., Charrier, R., Martinod, J., David, C., Tassara, A., Tapia, F., Fock, A., 2010. Crustal-scale structural architecture in central Chile based on seismicity and surface geology: Implications for Andean mountain building. Tectonics 29. https://doi.org/10.1029/2009TC002480

Ghiorso, M.S., Evans, B.W., 2008. Thermodynamics of rhombohedral oxide solid solutions and a revision of the Fe-Ti two-oxide geothermometer and oxygen-barometer. Am. J. Sci. 308, 957–1039. https://doi.org/10.2475/09.2008.01

Gottsmann, J., Martí, J. (Eds.), 2008. Caldera Volcanism Analysis, Modeling and Response, Developments in Volcanology.

Gregg, P.M., De Silva, S.L., Grosfils, E.B., Parmigiani, J.P., 2012. Catastrophic caldera-forming eruptions: Thermomechanics and implications for eruption triggering and maximum caldera dimensions on Earth. J. Volcanol. Geotherm. Res. 241–242, 1–12. https://doi.org/10.1016/j.jvolgeores.2012.06.009

Hammond, P.A., Taylor, L.A., 1982. The ilmenite/titano-magnetite assemblage: kinetics of re-equilibration. Earth Planet. Sci. Lett. 61, 143–150. https://doi.org/10.1016/0012-821X(82)90047-4

Hughes, G.R., Mahood, G.A., 2011. Silicic calderas in arc settings: Characteristics, distribution, and tectonic controls. Bull. Geol. Soc. Am. 123, 1577–1595. https://doi.org/10.1130/B30232.1

Johnson, M.C., Rutherford, M.J., 1989. Experimental calibration of the aluminum-in-hornblende geobarometer with application of Long Valley caldera (California) volcanic rocks. Geology 17, 837–841. https://doi.org/10.1130/0091-7613(1989)017<0837:ECOTAI>2.3.CO;2

Lara, L., Wall, R., Stockli, D., 2008. La ignimbrita Pudahuel (Asociación Piroclástica

Pumícea) y la caldera Diamante (33° S): nuevas edades U–Th–He, in: XVII Congreso Geológico Argentino. p. 1365.

Larsen, J.F., 2006. Rhyodacite magma storage conditions prior to the 3430 yBP caldera-forming eruption of Aniakchak volcano, Alaska. Contrib. to Mineral. Petrol. 152, 523–540. https://doi.org/10.1007/s00410-006-0121-4

Lipman, P.W., 2000. Calderas. Encycl. Volcanoes 643–662.

Marsh, B.D., 1981. On the crystallinity, probability of occurrence, and rheology of lava and magma. Contrib. to Mineral. Petrol. 78, 85–98. https://doi.org/10.1007/BF00371146

Masturyono, McCaffrey, R., Wark, D.A., Roecker, S.W., Fauzi, Ibrahim, G., Sukhyar, 2001. Distribution of magma beneath the Toba caldera complex, north Sumatra, Indonesia, constrained by three-dimensional P wave velocities, seismicity, and gravity data. Geochemistry, Geophys. Geosystems 2. https://doi.org/10.1029/2000GC000096

Mora, D., Tassara, A., 2019. Upper crustal decompression due to deglaciation-induced flexural unbending and its role on post-glacial volcanism at the Southern Andes. Geophys. J. Int. 216, 1549–1559. https://doi.org/10.1093/gji/ggy473

Muñoz-Gómez, M., Payacán, Í., Gutiérrez, F., Farías, M., Charrier, R., Polvé, M., 2019. Silicic volcanism triggered by increased denudation rates in the Quaternary Andean arc of central Chile between 33°50′-34°30′S. Lithos 355. https://doi.org/10.1016/j.lithos.2019.105242

Pallister, J.S., Hoblitt, R.P., Reyes, A.G., 1992. A basalt trigger for the 1991 eruptions of Pinatubo volcano? Nature 356, 426–428. https://doi.org/10.1038/356426a0

Pamukçu, A.S., Wright, K.A., Gualda, G.A.R., Gravley, D., 2020. Magma residence and eruption at the Taupo Volcanic Center (Taupo Volcanic Zone, New Zealand): insights from rhyolite-MELTS geobarometry, diffusion chronometry, and crystal textures. Contrib. to Mineral. Petrol. 175, 1–27. https://doi.org/10.1007/s00410-020-01684-2

Pineda, C., 2015. Geocronología U-Pb en circones de la Ignimbrita Pudahuel. Universidad

de Chile, Santiago, p. 105. Geologist Professional Degree Thesis.

Rabassa, J., Clapperton, C.M., 1990. Quaternary glaciations of the southern Andes. Quat. Sci. Rev. 9, 153–174. https://doi.org/10.1016/0277-3791(90)90016-4

Self, S., 2015. Explosive Super-Eruptions and Potential Global Impacts, Volcanic Hazards, Risks and Disasters. Elsevier Inc. https://doi.org/10.1016/B978-0-12-396453-3.00016-2

Singer, B.S., Thompson, R.A., Dungan, M.A., Feeley, T.C., Nelson, S.T., Pickens, J.C., Brown, L.L., Wulff, A.W., Davidson, J.P., Metzger, J., 1997. Volcanism and erosion during the past 930 k.y. at the Tatara-San Pedro complex, Chilean Andes. Bull. Geol. Soc. Am. 109, 127–142. https://doi.org/10.1130/0016-7606(1997)109<0127:VAEDTP>2.3.CO;2

Sruoga, P., Etcheverr, M.P., Feineman, M., Rosas, M., Burkert, C., Iba, O., Aires, B., Luis, S., 2012. Complejo Caldera Diamante-Volcán Maipo 69, 508–530.

Sruoga, P., Llambías, E.J., Fauqué, L., Schonwandt, D., Repol, D.G., 2005. Volcanological and geochemical evolution of the Diamante Caldera-Maipo volcano complex in the southern Andes of Argentina (34°10′S). J. South Am. Earth Sci. 19, 399–414. https://doi.org/10.1016/j.jsames.2005.06.003

Venezky, D.Y., Rutherford, M.J., 1999. Petrology and Fe-Ti oxide reequilibration of the 1991 Mount Unzen mixed magma. J. Volcanol. Geotherm. Res. 89, 213–230. https://doi.org/10.1016/S0377-0273(98)00133-4

Wall, R.M., Lara, L.E., Perez de Arce, C., 2001. Upper pliocene-lower pleistocene $^{40}Ar/^{39}Ar$ ages of Pudahuel ignimbrite (Diamante-Maipo volcanic complex), Central Chile ($33.5^{0}S$).

Wallace, P.J., 2005. Volatiles in subduction zone magmas: Concentrations and fluxes based on melt inclusion and volcanic gas data. J. Volcanol. Geotherm. Res. 140, 217–240. https://doi.org/10.1016/j.jvolgeores.2004.07.023

Waters, L.E., Lange, R.A., 2015. An updated calibration of the plagioclase-liquid hygrometer-thermometer applicable to basalts through rhyolites. Am. Mineral. 100, 2172–2184. https://doi.org/10.2138/am-2015-5232

Zhang, Y., 2010. Diffusion in minerals and melts: Theoretical background. Rev. Mineral. Geochemistry 72, 5–59. https://doi.org/10.2138/rmg.2010.72.2